IEKP-KA/2004-15

Studien an Siliziumstreifendetektoren

für das CMS Experiment

Thomas Weiler

Zur Erlangung des akademischen Grades eines
DOKTORS DER NATURWISSENSCHAFTEN
der Fakultät für Physik der
Universität Karlsruhe (TH)

genehmigte

DISSERTATION

von

Dipl. Physiker Thomas Weiler

aus Karlsruhe

Karlsruhe, 16. Juni 2004

Tag der mündlichen Prüfung: 2.Juli 2004
Referent: Prof. Dr. Th. Müller
Korreferent: Prof. Dr. W. de Boer

IEKP-KA/2004-15

Studies on Silicon Strip Detectors

for the CMS Experiment

Zur Erlangung des akademischen Grades eines
Doktors der Naturwissenschaften
der Fakultät für Physik der
Universität Karlsruhe (TH)

genehmigte

Dissertation

von

Dipl. Physiker Thomas Weiler

aus Karlsruhe

Karlsruhe, 16. Juni 2004

Tag der mündlichen Prüfung: 2. July 2004
Referent: Prof. Dr. Th. Müller
Korreferent: Prof. Dr. W. de Boer

Contents

Deutsche Zusammenfassung

Das Standardmodell der Teilchenphysik beschreibt die Grundbausteine der Materie und ihre Wechselwirkungen. Es wurde von verschiedensten Experimenten bis zu Energien von 200 GeV vermessen und mit hoher Genauigkeit bestätigt. Eine offene Frage der Teilchenphysik ist die Herkunft der Masse der Teilchen. Im Standardmodell wird die Masse mit Hilfe des *Higgs Mechanismus* generiert. Dies erfordert die Existenz eines *Higgs-Bosons*, nach dem in bestehenden und künftigen Beschleuniger Experimenten gesucht wird.

Die Suche nach neuen Teilchen stellt an Beschleuniger und Detektoren immer höhere Anforderungen. Um die Abnahme der Wirkungsquerschnitte, der zu untersuchenden Zerfälle, mit steigender Schwerpunktsenergie zu kompensieren, benötigt man immer höhere Teilchenraten (Luminosität). Dies führt zu einer hohen Teilchendichte im Detektor, welche durch eine hohe Granularität des Detektors kompensiert werden kann und einer hohen Rate an strahlungsinduzierte Schädigungen am Detektor und seiner Ausleseelektronik, welche im Design der Detektoren berücksichtigt werden müssen. Der im Aufbau befindliche Proton-Proton Beschleuniger LHC[1] am CERN[2] wird bei einer Schwerpunktsenergie von 14 TeV und einer Luminosität von $L = 10^{34}\text{cm}^2\text{s}^{-1}$ arbeiten. Für den zentralen Spurdetektor des CMS[3] Experimentes erwartet man eine Fluenz innerhalb der Betriebszeit von zehn Jahren am LHC von $1.6 \times 10^{14}\ n_{1MeV}\text{cm}^{-2}$ im Bereich der inneren Spurdetektoren (im Abstand bis 60 cm vom Strahlrohr) und $0.5 \times 10^{14}\ n_{1MeV}\text{cm}^{-2}$ im Bereich der äußeren Spurdetektoren (im Abstand von 60 cm bis 110 cm vom Strahlrohr).

Ein Teil dieser Arbeit beschäftigte sich mit dem Aufbau von Teststationen zur Qualifikation von Siliziumstreifendetektoren insbesondere im Hinblick auf bestrahlte Siliziumdetektoren.

Ein weiterer Teil dieser Arbeit beschäftigt sich mit der Untersuchung der Strahlhärte von Siliziumstreifendetektoren für das CMS Experiment. Teilchen die den Detektor durchdringen erzeugen nicht nur Elektron-Loch Paare die als Signal von der Ausleseelektronik registriert werden, sondern können auch Siliziumatome aus ihrem Gitterplatz herausschlagen. Die hierdurch im Silizium entstandenen Strahlungsschäden, Zwischengitteratome und Fehlstellen, sind bei Raumtemperatur beweglich und können durch das Kristallgitter wandern. Ein Teil der Zwischengitteratome rekombiniert wieder mit Fehlstellen, ein anderer Teil bildet Defektkomplexe, welche bei Raumtemperatur stabil sind. Sowohl die Defektkomplexe als auch die Zwischengitteratome und Fehlstellen ändern die elektrischen Eigenschaften des Siliziumstreifendetektoren im Vergleich zum unbestrahlten Fall. Zu einem tragen die zusätzlichen Defekte im Kristallgitter zum Leckstrom bei, zum anderen ändert sich die effektive Ladungsträgerkonzentration und damit die Verarmungsspannung des Siliziumdetektors.

[1]LHC: large hadron collider
[2]CERN: Centre Européene pour la Recherche Nucléaire
[3]CMS: Compact Muon Solenoid

Für die Bestrahlungsstudie wurden zwei CMS Siliziumstreifendetektoren und ein Frontend-Hybrid (Platine zum Auslesen der Streifen) mit 26 MeV Protonen und ein Siliziumstreifendetektor mit Neutronen bestrahlt. Diese beiden Teilchensorten wurden zur Untersuchung der Strahlungsschäden benutzt, da man um den Wechselwirkungspunkt hauptsächlich Protonen erwartet und im äußeren Bereich des Spurdetektors ein Großteil der Strahlungsschädigung von am elektromagnetischen Kalorimeter rückgestreuten Neutronen induziert wird.

Die Detektoren und der Frontend-Hybrid wurden vor und nach der Bestrahlung qualifiziert, d.h. in allen Auslesemoden mit und ohne Kalibrationsignalen getestet. An den Siliziumstreifendetektoren wurde zusätzlich noch das Ausheilverhalten der Strahlungsschäden und das Signal zu Rauschen für verschiedene Ausheilzeiten untersucht. Aus den globalen IV- und CV-Kurven werden der zu erwartende Leckstrom und die Verarmungsspannung ermittelt. Aus Messungen mit kosmischer Strahlung oder radioaktiven Quellen läßt sich das Signal zu Rauschen bestimmen, ein wichtiger Detektorparameter.

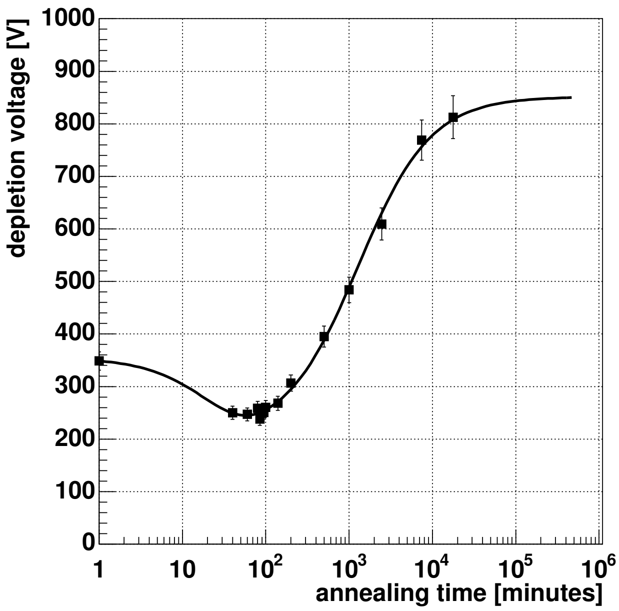

Figure 1: *Ausheilverhalten von Strahlungsschäden in einem Siliziumdetektormodul (Modul 671), das mit Protonen zu einer Fluenz von* 0.7×10^{14} $n_{1MeV} cm^{-2}$ *bestrahlt wurde. Die Datenpunkte lassen sich gut mit dem "Hamburg Modell" beschreiben. Das Minimum der Verarmungsspannung wird nach etwa* 80 *Minuten, bei einer Temperatur von* $60°C$ *erreicht. Dies entspricht etwa* 10 *Tagen bei Raumtemperatur*

Abbildung 1 zeigt die Abhängigkeit der Verarmungsspannung nach Bestrahlung von der Ausheilzeit. Die Änderung der effektiven Ladungsträgerkonzentration und damit die Änderung der Verarmungsspannung kann mit dem *Hamburg Modell* beschrieben werden. Dieses parametrisiert das Ausheilen von Strahlungsschäden (dominiert den Verlauf der Kurve in Abbildung 1 in den ersten 100 Minuten), die Bildung von stabilen Defektkomplexen während des Ausheilens (verantwortlich für den Anstieg der Kurve bei höheren Ausheilzeiten) und während der Bestrahlung (Verschiebung der Kurve zu höheren Spannungen um einen konstanten Wert). Aus dem Verlauf der Kurve in Abbildung 1 erkennt man auch welche Konsequenzen sich für den Betrieb der Detektoren ergeben, zum einem müssen sie gekühlt werden um die Ausheilprozesse zu verlangsamen bzw. zu stoppen und zum anderen sollten die Detektoren nach jeder Bestrahlungsphase für etwa zehn Tage bei Raumtemperatur gehalten werden um die Strahlungsschäden auszuheilen und um damit die Verarmungsspannung niedrig zu halten. Dies impliziert aber auch, daß für eventuelle Wartungsarbeiten nur zehn Tage zur Verfügung stehen, ein Überschreiten dieser Zeit führt zur einer Erhöhung der Verarmungsspannung, welche irreversibel ist.

Abbildung 2 zeigt das Signal zu Rauschen eines Siliziumstreifendetektors für verschiedene Ausheilzeiten in beiden Auslesearten des APV (analog pipeline voltage) chips. Das Signal zu Rauschen nimmt nach Bestrahlung für beide Auslesearten um ca. 30% ab, ist aber mit ≈ 24 im Peak Modus und ≈ 16 im Deconvolution Modus ausreichend für die Messung von Teilchendurchgängen und liegt weit oberhalb der Spezifikation von CMS [CMS98, CMS00].

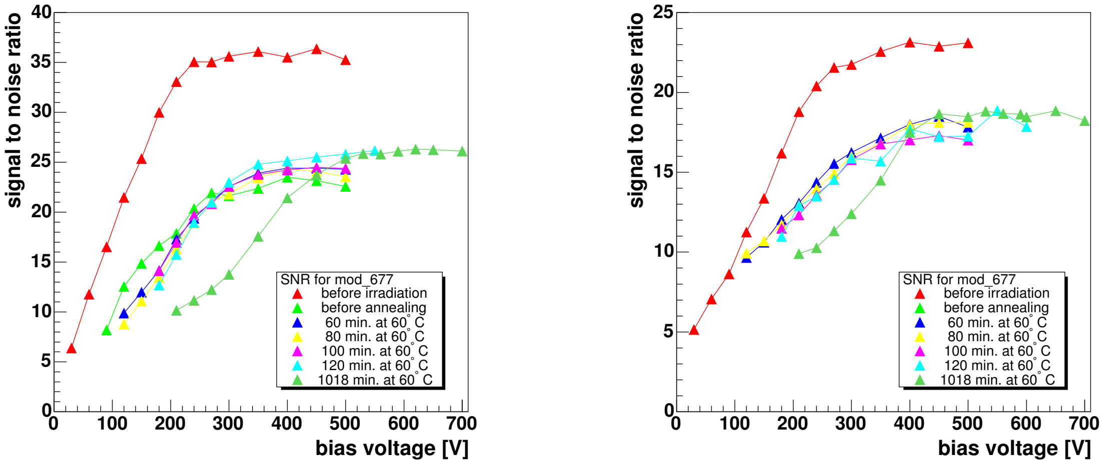

(a) (b)

Figure 2: *Signal zu Rauschen für verschiedene Ausheilzeiten des Moduls 677 bei den Auslesearten (a) Peak Modus und (b) Deconvlutions Modus. Dieses Detektormodul wurde mit Protonen zu einer Fluenz von* 0.7×10^{14} $n_{1MeV}\,cm^{-2}$ *bestrahlt*

Ein weiterer Teil der Studien an Siliziumstreifendetektoren beinhaltet die Untersuchung von Streifendefekten und ihre Auswirkungen auf das Detektorverhalten. Hierbei wurde insbesondere der Einfluß des Streifenleckstromes auf die Detektorauslese (Rauschen des Detektors) und desweiteren der Einfluß mechanischer Verspannungen des Detektors auf den Leckstrom und das Rauschen untersucht.

Chapter 1

Introduction

The standard model of particle physics describes the constituents of matter and their interaction. It is tested up to energies of 200 GeV. The missing part of the standard model, the Higgs boson or even new particles are expected to be detected at higher energies. The large hadron collider (LHC) under construction at CERN will provide the insight to standard model physics and new physics on the TeV-scale.

The high luminosity needed to compensate the low interaction cross section at high energies for the physics of interest and resulting background make great demands on the detectors and the electronics. The compact muon solenoid (CMS) central tracking system placed closed to the interaction point has to cope with a high occupancy and the harsh radiation environment of the LHC.

This thesis concentrates on the qualification of irradiated silicon strip detector modules for the CMS experiment, the investigation of strip faults and the setup of test-stations needed for these tasks. In chapter 2 the accelerator LHC and the physics program at the LHC are presented. This gives the boundaries for design considerations of the experiments. Chapter 3 introduces the CMS experiment giving an overview of all sub-detectors. The silicon strip tracker (SST) in which this work is involved is described in more detail. Chapter 4 summarizes the properties of semiconductors and semiconductor devices including silicon strip detectors. The front-end electronics needed to readout the detectors is described in some detail in chapter 5. The test-stations developed for the qualification of the detector modules during the production phase and the performance studies presented in this work are presented in chapter 6.

In chapter 7 the mechanism of radiation induced damage to silicon detector are discussed and macroscopic effects on the detector properties like the depletion voltage and leakage current are described. The two radiation facilities where the modules and front-end hybrids under investigation have been irradiated are introduced and the data before and after irradiation is presented. The depletion voltage is parameterized using the "Hamburg model", well describing the measured data. When possible the data measured on detector modules is compared with data measured on sensor basis. It should be mentioned that throughout this work speaking of sensors means the plain silicon "detectors" with no readout electronics connected to and detector or detector modules are fully equipped detectors with readout electronics.

During measurements on sensors done by the quality control center (QTC) to permanently check the production quality of the manufactures of the silicon strip sensors, several problems has been detected on different batches from one supplier. To see the consequences of these problems on the performance of the detector modules and to get additional hints on the origin of these problems some modules were built out of these sensors. Chapter 8 presents the results from the measurements done on such modules and additionally shows some strips failure occurred after irradiation.

Chapter 2

Physics Objectives at the Large Hadron Collider (LHC)

The particle energies in reach with the LHC allow to probe physics of the Standard Model of particles, especially for the open questions of electroweak symmetry breaking and the search for physics beyond the Standard Model. The main physics objectives are the search for the standard model (SM) Higgs boson and the various minimal supersymmetric standard model (MSSM) Higgs bosons and supersymmetric particles. Measurements of CP-violation in the B sector, the study of B_s^0 oscillations are also foreseen, as well as the search for signals from QCD de-confinement via relative suppression within the Υ family in heavy ion collisions. Beside the SM and supersymmetric models there are several other theoretical models such as Technicolor, extra dimension, leptoquarks or new gauge bosons, which can be probed.

2.1 The Large Hadron Collider

The LHC is a proton-proton collider installed in the former large electron positron collider (LEP) tunnel with an circumference of ≈ 27 km. The two proton beams are accelerated to a center of mass energy of $\sqrt{s} = 14$ TeV. The proton beams collide at four interaction points where the experiments are placed. There are two general purpose detectors CMS and ATLAS and two specialized detectors, ALICE intends to study heavy ion collisions and LHCb is optimized for the study of b-physics. At the startup of the LHC it is foreseen to operate the accelerator at "low" luminosity of $L_{low} = 10^{33}$ cm^{-2}s^{-1} continuously increasing over a period of three years to the design value of $L_{high} = 10^{34}$ cm^{-2}s^{-1}. This high luminosity compared to present colliders like the Tevatron[1] with $L = 10^{31}$ cm^{-2}s^{-1} is needed to compensate the lower cross sections at higher energies. This allows the study of physics in the 1 TeV scale at the LHC.

2.2 Standard Model Higgs

The Standard Model describes the basic constituents of matter, namely quarks and leptons, interacting by the exchange of gauge bosons, such as gluons, photon, W and Z bosons. All these particles have been observed so far by experiments. However there is one missing

[1] $p\bar{p}$-collider at Fermilab (Chicago), with a center of mass energy $\sqrt{s} = 1.9$ TeV

particle, the Higgs boson, which gives mass to weak gauge bosons W and Z, without violating the gauge theory needed for the renormalization of field theories.

2.2.1 Higgs Production

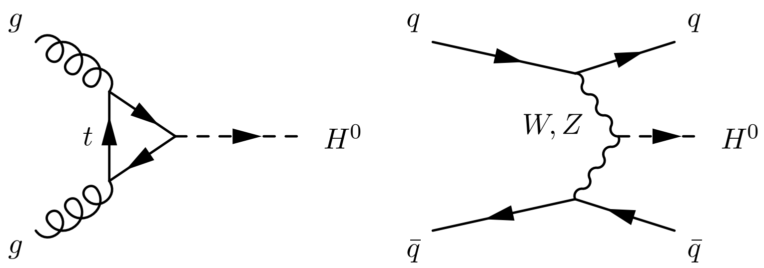

(a) Gluon fusion (b) Vector boson fusion

Figure 2.1: *Standard Model Higgs production (a) gluon-gluon fusion, the Higgs couples via a quark loop to the gluons, (b) vector boson fusion*

There are several production mechanisms for Standard Model Higgs bosons at LHC. First there is the gluon-gluon fusion (see figure 2.1a), which plays a dominant role throughout the entire Higgs boson mass range up to 1 TeV. The gluon coupling to the Higgs boson is mediated by a heavy quark loop, where the top quark loop gives the main contribution to the cross section.

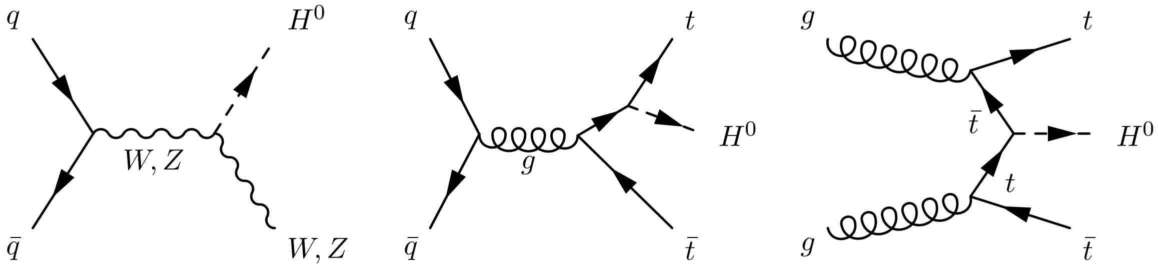

(a) Higgs strahlung off vector bosons (b) Higgs strahlung off top (c) Higgs strahlung off top

Figure 2.2: *Standard Model Higgs production via "Higgs strahlung" (a) off vector bosons, (b) and (c) off heavy quarks*

A further important process for Higgs bosons production is the vector boson fusion $ZZ, W^+W^- \rightarrow H$ (see figure 2.1b). The cross section is one order of magnitude smaller for intermediate masses than gluon-gluon fusion, but competitive for larger Higgs masses (see figure 2.3).

For the search of light Higgs boson masses the "*Higgs strahlung*" processes (see figure 2.2) are of importance. Though the cross section for these processes are smaller than for gluon fusion, the process $q\bar{q} \rightarrow V^* \rightarrow VH$ provides a clean signature for Higgs bosons due to the leptonic decay of vector boson. The Higgs strahlung of top quarks ($gg, q\bar{q} \rightarrow t\bar{t}H$) is interesting for measuring the $Ht\bar{t}$ Yukawa coupling, the cross section of this process is directly proportional to the square of the coupling constant [kra03]. The cross section of various Higgs production processes at the LHC for a mass range of up to 1 TeV is shown in figure 2.3.

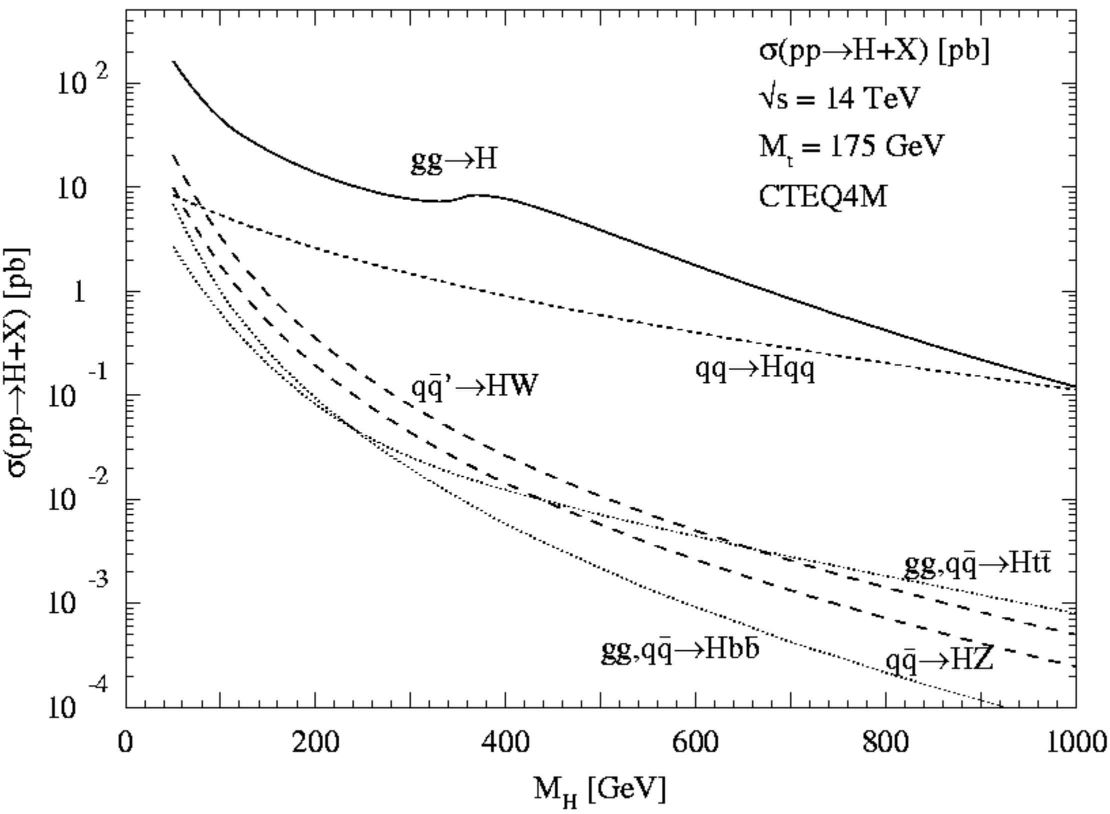

Figure 2.3: *Standard Model Higgs production cross section at LHC for various production mechanisms as function of the Higgs mass. QCD correction are included except for Higgs strahlung* [spi00]

2.2.2 Higgs Decay

Just like for the production mechanism there are several possibilities the Higgs boson can decay to depending on its mass. Figure 2.4 shows the branching ratio for the main decay modes of the Standard Model Higgs for masses up to 0.6 TeV.

In the mass region above the LEP limit of $m_H > 114.5$ GeV to $m_H < 150$ GeV, the most promising decay is $H \rightarrow \gamma\gamma$. Due to the background from pair annihilation of quarks, gluon fusion and bremsstrahlung processes the detection of the Higgs boson in the di-photon channel requires an electromagnetic calorimeter with excellent energy resolution and high granularity. A further interesting channel to find the Higgs boson is based on the large branching ratio for the decay $H \rightarrow b\bar{b}$ for $m_H < 130$ MeV (see figure 2.4). It could be used in the associated production channel $t\bar{t}H$ to extract the Higgs signal in the decay $t\bar{t}H \rightarrow l^{\pm}\nu q\bar{q}b\bar{b}b\bar{b}$, where the Higgs boson decays into $b\bar{b}$ pair, one top leptonically and the other hadronically [dro01]. Whereas the signal from a bare $H \rightarrow b\bar{b}$ decay would be difficult to detect due to the huge QCD background. For this channel a powerful tracking detector is essential.

The channel $H \rightarrow ZZ^{*} \rightarrow 4l$ is a promising one to observe the Higgs boson in the mass range 130 GeV $< m_H <$ 180 GeV. Below $2M_Z$ the event rate is small and the background reduction is more difficult since one of the Z is off mass-shell. For $m_H < 2m_Z$ the background

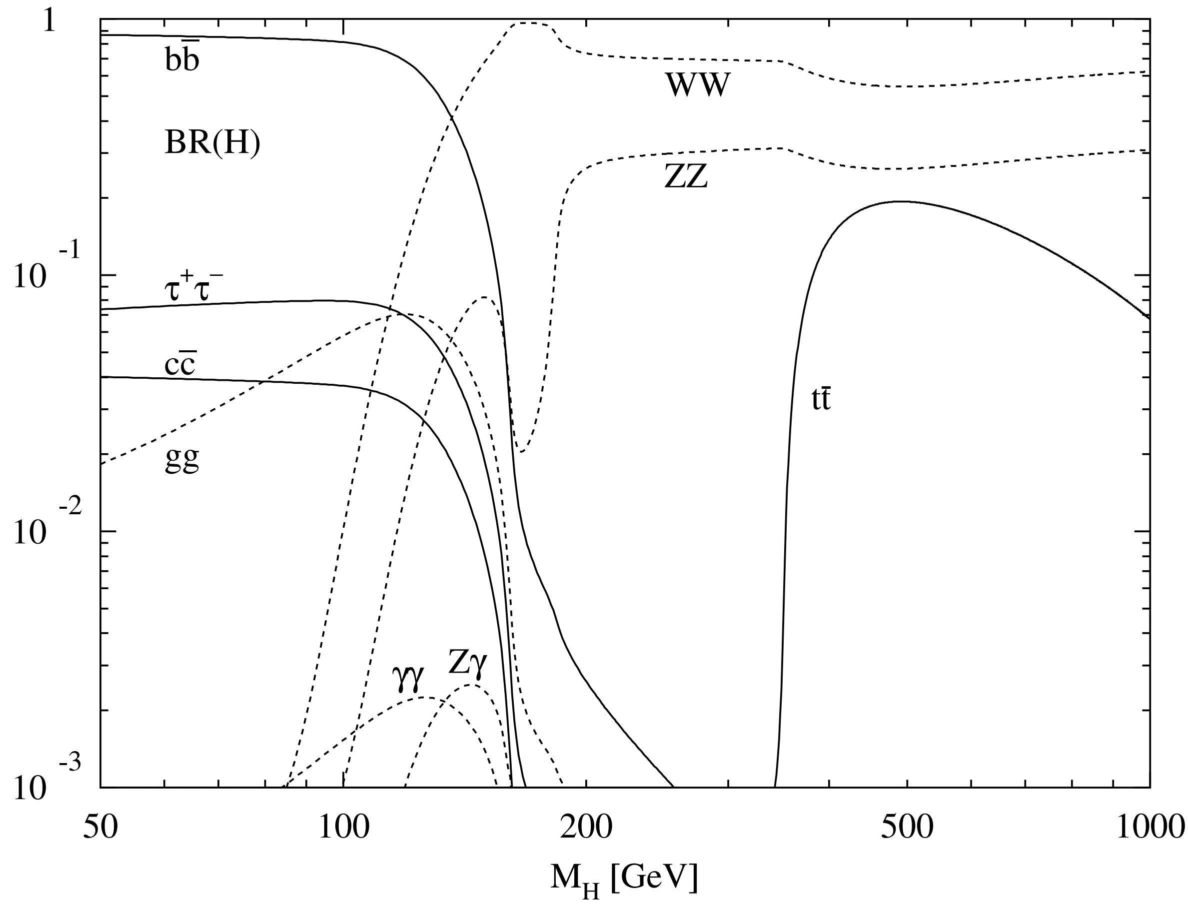

Figure 2.4: *Branching ratio for the main decay modes of the Standard Model Higgs, as function of the Higgs mass* [djo97]

comes from $t\bar{t}$, $Zb\bar{b}$ and ZZ^*. This background can be suppressed by lepton isolation and Z-mass cuts. The channel $H \rightarrow WW^* \rightarrow l^+\nu l^-\nu$ provides a Higgs boson discovery in the mass range 155 GeV $< m_H <$ 180 GeV.

In the mass range 180 GeV $< m_H <$ 600 GeV the most promising channel is $H \rightarrow ZZ \rightarrow 4l$, with both Z bosons now on mass-shell. At this energy the event rate is higher, the background is small and could be reduced by applying Z-mass cuts on both lepton pairs. The $H \rightarrow WW \rightarrow l^+\nu l^-\nu$ channel with high transverse momentum leptons and missing energy will also contribute to the discovery of the Higgs boson in this mass range. For higher Higgs masses (up to $m_H \approx 1$ TeV) the channels $H \rightarrow ZZ \rightarrow l^+\nu l^-\nu$, $H \rightarrow WW \rightarrow lljj$ or $H \rightarrow WW \rightarrow lljj$ have to be used [CMS94, kra03].

2.3 B-Physics

B-physics allows stringent tests on the Standard Model description of CP violation and is also sensitive to new physics. The large production cross section of $b\bar{b}$ pairs gives the possibility to study various reaction channels with a precision equal or better than at Tevatron or the e^+e^- B-factories, due to higher statistics.

In the Standard Model CP violation is described in the framework of the 3×3 complex unitarity mass-mixing matrix (CKM-matrix), which can be described by four independent parameters ("Wolfenstein parameterization") [bat02]. These parameters could be geometrically represented in the so called unitarity triangle (see figure 2.5), which is normally discussed considering experimental measurements.

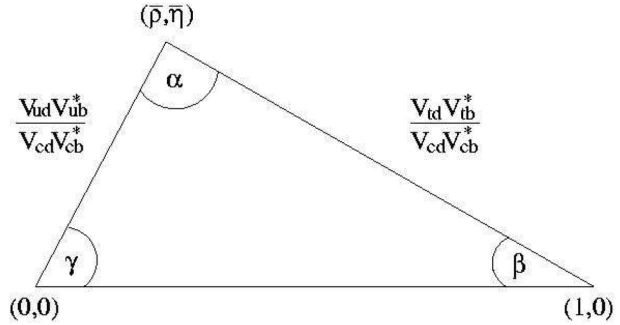

Figure 2.5: *The unitarity triangle of the CKM matrix, using the rescaled parameters* $(\bar{\rho}, \bar{\eta})$

For example the angle γ can be measured from the decay $B_s \to D_s^{\pm} K^{\pm}$ and from the branching ratio of the $B_d \to h_u l \nu$ and $B_d \to h_c X$ one can access $|V_{ub}| / |V_{cb}|$. These decays probe processes only on tree level and are therefore not sensitive to new physics. On the other hand the angle β can be measured by $B_d \to J/\Psi K_s^0$ and $|V_{ub}| / |V_{cb}|$ through B_d mixing, which are both sensitive to new physics contributions in the B_d loop diagrams [ege03].

Rare decays with Standard Model branching ratio of around 10^{-10} for $B_d \to \mu^+\mu^-$ and 4×10^{-9} for the decay $B_s \to \mu^+\mu^-$ are good probes for new physics. As these decays have to be mediated to loops, particles from new physics will possibly increase the branching ratio for these rare decays [ege03].

2.4 Supersymmetry

Supersymmetry is a symmetry between fermions and bosons. It postulates for every quark and lepton (q, l) a scalar superpartner called squark and slepton $(\tilde{q}, \tilde{l})$, and for the gauge bosons (g, γ, W, Z) fermionic superpartners called *gauginos* $(\tilde{g}, \tilde{\gamma}, \tilde{W}, \tilde{Z})$. The minimal supersymmetric extension of the Standard Model needs two Higgs doublets with opposite hypercharge $Y = \pm 1$ to generate masses for up and down type fermions, leading to five supersymmetric Higgs bosons. There are two CP even Higgs bosons, a light one h^0 and a heavier one H^0, one CP odd A^0 and two charged Higgs bosons $H^{\pm}$ [roy03].

The extra particles introduced by Supersymmetry ensure, that the quadratically divergent quantum corrections from quark, lepton and Higgs boson loops are canceled. This solves the hierarchy problem of the Standard Model. Supersymmetry has to be a broken symmetry, otherwise the particles and their superpartners would be degenerated in masses, which is not observed. If Supersymmetry is a true symmetry of nature, hints of its existence will be found at the LHC.

2.5 Heavy Ion Physics

Additional to the proton-proton collisions, heavy ion collisions are foreseen for the physics program of the LHC. The LHC can accelerate different ions ranging from oxygen to lead up to energies per nucleon-nucleon pair of $\sqrt{S_{NN}} = 5.5$ to 7 TeV suitable to study dense hadronic matter. The physics goals of the heavy ion run are the measurement of nuclear structure functions, the study of parton propagation in cold hadronic matter and the quark-gluon plasma [wro02].

2.6 Exotica

The Standard Model of strong and electroweak interaction is in excellent agreement with experimental data. However, there are other theoretical models which can be probed at a mass scale of 1 TeV at the LHC.

The question whether the quark and leptons are fundamental particles or do they have a substructure may be answered if there are deviations from the cross section, an excess of high p_T jets or a more isotropic di-jet angular distribution. If quarks are composite particles and the compositeness scales within the reach of the LHC energy it may be possible to observe excited quark states.

In the Technicolor model the dynamical breaking of electro-weak symmetry is obtained by techni-fermions strongly interacting at a high energy scale. These techni-fermions could be produced by quark anti-quark fusion and decay into vector bosons and detected by the leptonic decay modes of these vector bosons.

In many models the existence of new gauge bosons W' and Z' is predicted. Leptoquarks a particle with lepton and baryon quantum number appear in extensions of the Standard Model or grand unification theory. The LHC can also contribute to the search for monopoles, which might explain the quantization of the electric charge, or to the search for extra dimension.

Chapter 3

The Compact Muon Solenoid (CMS) Experiment

The following chapter introduces considerations taken into account for the construction of a complex detector system such as the CMS detector which will be operated in the harsh radiation environment of a hadron collider. The sub-detectors, specialized for the measurement of certain particles and their properties, will be introduced, special attention is turned to the tracking system in which this PhD is involved.

It is common practice to express the angular acceptance of the sub-detectors in units of *rapidity* or *pseudo-rapidity*. The rapidity is a variable to describe the behavior of particles in inclusively measured reaction. It is defined by

$$y = \frac{1}{2} \ln \left(\frac{E + p_l}{E - p_l} \right) = \tanh^{-1} \left(\frac{p_l}{E} \right) \tag{3.1}$$

where p_l is the longitudinal momentum along the direction of the incident particle (beam axis) and E its energy. For large momenta $p \gg m$, which is fulfilled for all particles to be detected in CMS due to high center of mass energy of the LHC, the rapidity could be approximated by

$$y \approx -\ln \left[\tan \left(\frac{\theta}{2} \right) \right] = \eta \tag{3.2}$$

here θ is the angle between the measured particle and the undeflected beam. This approximation for the rapidity is called *pseudo-rapidity*. Table 3.1 shows the relation between θ and η [boc98].

θ [°]	90	45	40.4	15.4	15	10	5.7	2.1
η	0	0.88	1	2	2.03	2.44	3	4

Table 3.1: Relation between the angle θ (angle between the measured particle and the undeflected beam) and the pseudo-rapidity η [boc98]

3.1 Design Objectives

For the design objectives of the CMS detector both parameters given by the LHC and constraints from the physical program have to be taken into account. The low production cross-sections for new physics such as Higgs search and Supersymmetry at center of mass energy of $\sqrt{s} = 14$ TeV requires a high collision rate (luminosity) resulting in a large background, out of which the events of interest have to be extracted. The high luminosity of 10^{34} cm^{-2}s^{-1} and the LHC bunch crossing frequency of 40 MHz put great demands on the detector and its readout electronics. Thus an average of 20 events occur at the bunch crossing frequency of 25 ns resulting in 10^9 events per second.

From these considerations and the predicted decay channels follow that an optimized and redundant muon system is needed to separate interesting events from background (see chapter 2). In addition a compact design and good momentum resolution ask for a strong magnetic field realized by a superconducting solenoid and an efficient tracking system with high spatial resolution. A precise electromagnetic calorimeter for efficient detection of an intermediate mass Higgs boson decaying via $\gamma\gamma$ fits naturally in the CMS design. The electromagnetic calorimeter and a hadron calorimeter with good energy resolution are essential to trigger on missing energy events. Last but not least a high quality central tracking system is needed to achieve the points mentioned above [CMS94]. A high granularity for all sub-detectors is needed especially for the central tracker to separate track in the case of high occupancy.

3.2 Overview CMS Detector

Figure 3.1 shows a schematic of the CMS detector. Around the beam pipe close to the interaction point the silicon pixel detectors are located, surrounded by a silicon strip tracker (SST). The next shell of the detector builds the electromagnetic calorimeter followed by the hadron calorimeter. The central tracker and both calorimeters are located inside the superconducting solenoid, providing the magnetic field of 4 T. The muon system surrounding the complete detector uses the return yoke of the magnet as absorber. The very forward region is covered by the hadron forward calorimeter placed outside the solenoid enwrapping the beam pipe.

3.2.1 The Magnet

The magnet is the main structure of the CMS experiment, all sub-detectors are supported by it. It consists of a superconducting solenoid of 12.5 m length and an inner free diameter of 6 m, providing an uniform magnetic field of 4 T, allowing precise central and muon tracking. The inner coil radius is large enough to accommodate the central tracker and full calorimetry. The magnetic flux is returned via a 1.5 m thick iron yoke, in which the muon stations are integrated [CMS97c, her01].

3.2.2 The Muon Detectors

The ability to trigger on and to reconstruct muons at highest luminosities is the central concept of the CMS detector. Muons are an distinctive signature for most physic processes the LHC is designed for. The muon system consists of a barrel part integrated in the return

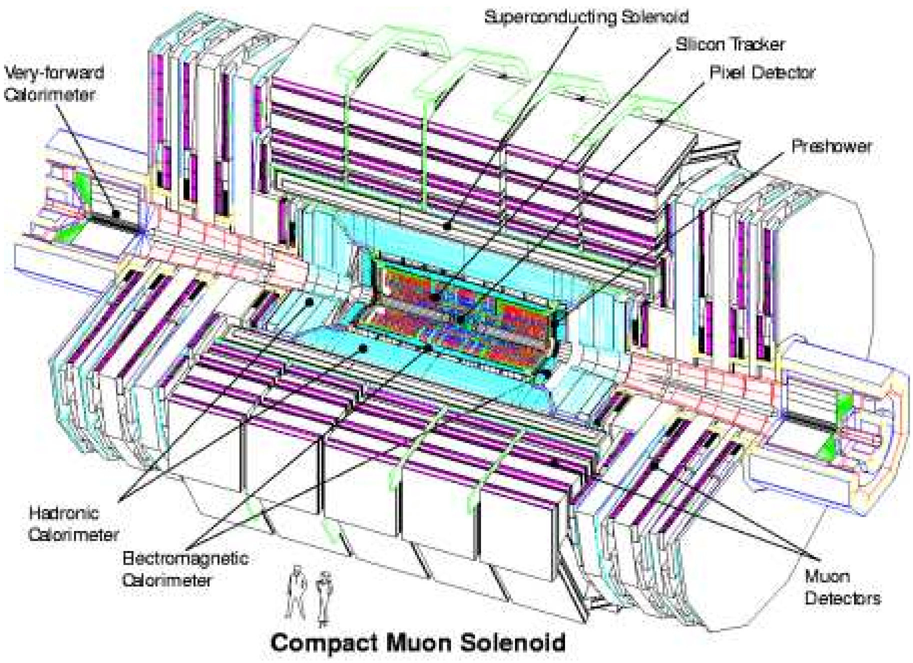

Figure 3.1: *Schematic of the CMS detector [CMSWEB]*

yoke of the superconducting magnet, with a magnetic field of 1.8 T, and an end-cap detector placed at each end of the solenoid.

The muon detector system utilizes three different detector technologies. In the barrel part drift tubes are used, covering a range of pseudo-rapidity $0.0 < |\eta| < 1.3$. The end-cap region is equipped with strip chambers, covering a range of $0.9 < |\eta| < 2.4$. Cathode strip chambers provide a high spatial precision in the presence of large and varying magnetic field, while their fast response time and finer segmentation allow operation in high rate environment. In both the barrel and end cap region resistive plate chambers are used for event selection covering a range of $0.0 < |\eta| < 2.1$. Resistive plate chambers provide a reasonable spatial resolution with an excellent time resolution. Furthermore, the resistive plate chambers have a different sensitivity to the background compared to drift tubes or cathode drift chambers, providing a redundant and complementary trigger capability.

The muon system covers a total surface in the barrel region of ≈ 2000 m^2 and ≈ 1500 m^2 in the end-cap region. The position resolution ranges between 50 μm and 200 μm across the covered pseudo-rapidity range and ensures a stand-alone transverse momentum resolution of about $\Delta p_t/p_t = 8$ to 15% at 10 GeV and $\Delta p_t/p_t = 20$ to 40% at 1 TeV. The momentum resolution will improve after linking with the silicon tracker to $\Delta p_t/p_t = 1$ to 1.5% at 10 GeV and $\Delta p_t/p_t = 6$ to 17% at 1 TeV [CMS97d, gia02].

3.2.3 Hadron Calorimeter

The hadron calorimeter measures energy and direction of particle jets and in combination with the electromagnetic calorimeter identifies neutrinos via the missing transverse energy. The determination of missing energy is a crucial signature for new physics, such as the searches for supersymmetric partners of quarks and gluons.

The hadron calorimeter consists of three parts, the barrel, two end-caps and the very forward calorimeters. Barrel and end-cap calorimeter are located inside the solenoid experiencing a magnetic field of 4 T. The hadron calorimeter is a sampling calorimeter, the active material (4 mm thick plastic scintillator) is inserted between copper absorber planes of 5 mm thickness in the barrel region and 8 mm thickness in the end-caps. The barrel hadron calorimeter covers an $\eta < 1.3$, the end-cap hadron calorimeters cover a pseudo-rapidity range of $1.3 < \eta < 3.0$ [CMS97b]. The very forward calorimeter covers a pseudo-rapidity range of $2.75 < \eta < 5.25$ allowing the measurement of missing transverse energy and forward jet tagging. The very forward calorimeter consists of quartz fibers inserted into grooves of a copper matrix, the shower particles produce light by the Cherenkov effect, therefore the quartz calorimeter is insensitive to low-energy neutrons, which will transverse in large numbers [mer98].

3.2.4 Electromagnetic Calorimeter

The electromagnetic calorimeter plays an essential role in the study of electroweak symmetry breaking. The search for the Higgs boson relies on information of the electromagnetic calorimeter, by measuring the decay into two photons ($H \to \gamma\gamma$) for $m_H < 150$ GeV or measuring electrons and positrons from W and Z decays originating from Higgs decays (e.g. $H \to WW$) for 140 GeV $\leq m_H \leq$ 700 GeV.

For the CMS electromagnetic calorimeter a scintillating crystal calorimeter was chosen, offering the best energy resolution, since most of the electrons or photons energy is deposited within the crystal volume. Lead tungstate ($PbWO_4$) was chosen as calorimeter crystal, well suited for the use in the LHC environment. It is radiation hard, has a short radiation length ($X_0 = 0.89$ cm), a small Moliere radius of 2.19 cm, which allows separation of nearby showers, and a fast scintillation time of 10 ns.

The electromagnetic calorimeter consist of a barrel part, two end-cap detectors and a pre-shower detector. The barrel part covers a pseudo-rapidity of $|\eta| < 1.49$, the crystals have a square cross-section of 22 mm^2 with a length of 230 mm corresponding to 25.8 X_0. The end-caps cover a pseudo-rapidity range of $1.48 < |\eta| < 2.6$.

The crystals in the barrel are readout by avalanche photodiodes (APDs), well suited for the operation in high transverse magnetic fields. In the end-caps the photodetectors are required to operate in a much higher integrated radiation dose and neutron fluence, which would increase the APDs leakage current and therefore the electronics noise to an unacceptable level. Here vacuum photo-triodes (VPTs) are used, which are more radiation tolerant but can not be operated at high transverse magnetic fields.

π^0 decay into two photons may produce a comparable signature as a single high energetic photon. In order to provide a better $\pi^0 - \gamma$ separation a pre-shower detector is placed in front of the calorimeter crystals. It consists of a silicon strip detector with a spatial resolution of ≈ 300 μm, enclosed in lead absorber. The pre-shower detector covers a pseudo-rapidity range from $|\eta| = 1.65$ to 2.61.

The energy resolution in the energy range from 25 GeV to 500 GeV, the range important for the decay $H \to \gamma\gamma$ can be parameterized as

$$\left(\frac{\sigma}{E}\right)^2 = \left(\frac{a}{\sqrt{E}}\right)^2 + \left(\frac{\sigma_n}{E}\right)^2 + c^2 \quad \text{(E in GeV)} \tag{3.3}$$

where a is a stochastic term, considering fluctuation in the shower containment and fluctuation in the photon yield. σ_n considers the noise contribution from readout electronics and pileup energy. The constant term c includes contributions from inter-calibration errors, crystal non-uniformities, and shower leakage. For the detection of high energetic photons and electrons the energy resolution is dominated by the constant term. Figure 3.2 shows the energy dependence for the different terms [CMS97a].

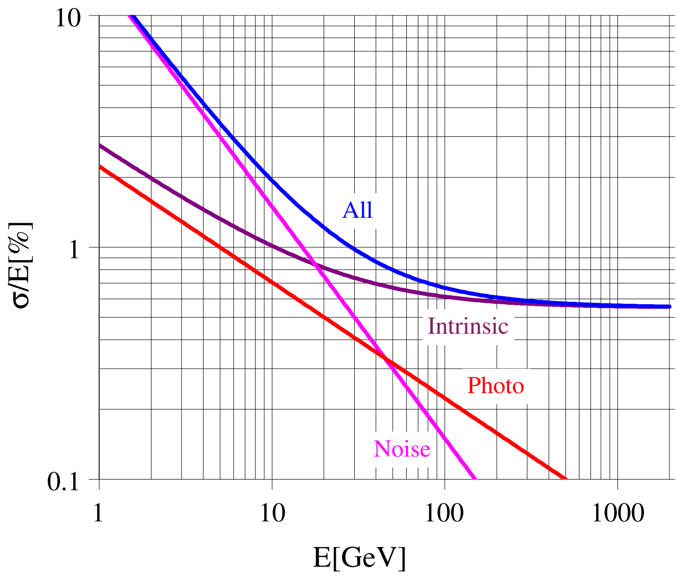

Figure 3.2: *Contributions to the energy resolution for the electromagnetic calorimeter. The line labeled "photo" represents the stochastic term, "noise" the noise term and the line labeled "intrinsic" counts for the constant term* [CMS97a]

3.2.5 The Central Tracker

The central tracking system of the CMS detector consists of a silicon pixel detector close to the beam pipe surrounded by a silicon strip detector [CMS98, CMS00]. A more detailed description of the silicon strip detector can be found in section 3.3.

The silicon pixel detector consists of three layers, surrounding the beam pipe at 4.3 cm, 7.2 cm and 11.0 cm, supplemented by two end-cap disk at each side. For optimal vertex position resolution in both (r, ϕ) and z-coordinate a square pixel shape of 150×150 μm^2 was chosen, resulting in a spatial resolution of below 20 μm. The whole pixel system consists of about 1400 detector modules arranged into 4 modules ladders in the barrel and 7 module blades in the end-cap disks. To readout the modules about 16000 readout chips are bump-bonded to the detector modules, giving total number of 45×10^6 readout channel (pixels) [kot01].

3.3 The Silicon Strip Tracker

This section will describe the layout of the silicon strip tracker and its modules, which are designed to meet the boundary conditions given by the LHC and the physics requirements such as a momentum resolution of 1 to 2% for 100 GeV muon and an impact parameter resolution of ≈ 10 to 20 μm.

3.3.1 Tracker Layout

The silicon strip tracker is divided into four subsystem, see figure 3.3. The four innermost layers arranged cylindrical around the interaction point build up the tracker inner barrel (TIB), followed by six cylindrical layers of the tracker outer barrel (TOB). Next to the TIB in each forward direction three disks with three layers of modules arranged in rings perpendicular to the beam line form the tracker inner disk (TID). The tracker end-cap (TEC) consists of nine disks in each forward direction with seven to four rings of detector modules. The number of rings, layers and their distance to the interaction point is illustrated in figure 3.3. The disks

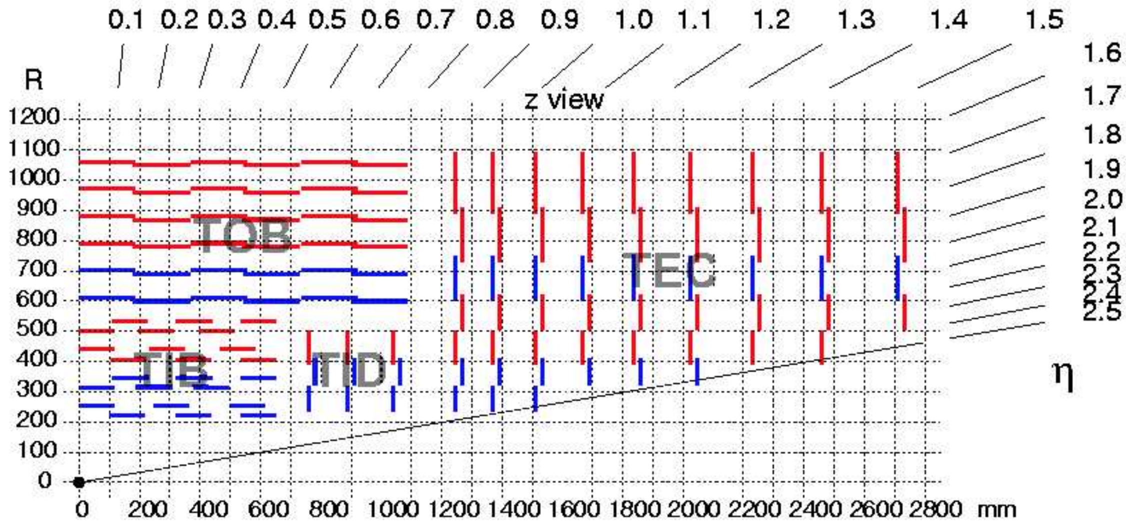

Figure 3.3: *Longitudinal section of one quadrant of the silicon strip tracker, single sided modules are represented by the red color and "double sided" (back to back mounted) modules are blue [die03a]*

and barrel layers are segmented in smaller substructures, the so called petals and rods, see figure 3.4.

The complete silicon strip tracker is built of single sided modules, with strips along the z-direction (beam direction) in the barrel and radial direction in the end-cap part of the detector, allowing readout of the $r\phi$-coordinate. For the separation of particle tracks three-dimensional information is needed. This is obtained by mounting a normal single sided module and one stereo module, with strips tilted by 100 mrad, back to back. The two innermost layers of TIB, TOB and TID, and the ring 1, ring 2 and ring 5 of TEC are equipped with these modules (see figure 3.3). This layout provides at least eight measurement points for high momentum tracks with $|\eta| < 2.5$ from which four come from so called double sided modules

3.3.2 The Modules

As mentioned above the complete silicon strip tracker consists of single sided modules, which are the smallest subunit of the tracking detector. Each module is made of a carbon fiber frame, supporting the silicon sensors (one or two depending on the module type) and the

(a) (b)

Figure 3.4: *View on a petal (a) and rod (b) the substructures of the disks and the barrel layers*

front-end readout hybrid. A kapton[1] foil bearing the supply lines for the high voltage, filter capacities and temperature sensors are glued between sensor and carbon fiber frame. The kapton foil electrically isolates the sensor's backplane from the conductive carbon fiber frame. Figure 3.5 shows a completely assembled TEC module of type ring 6 and a TOB module of type OB2 (for details about size and number of strips see appendix C).

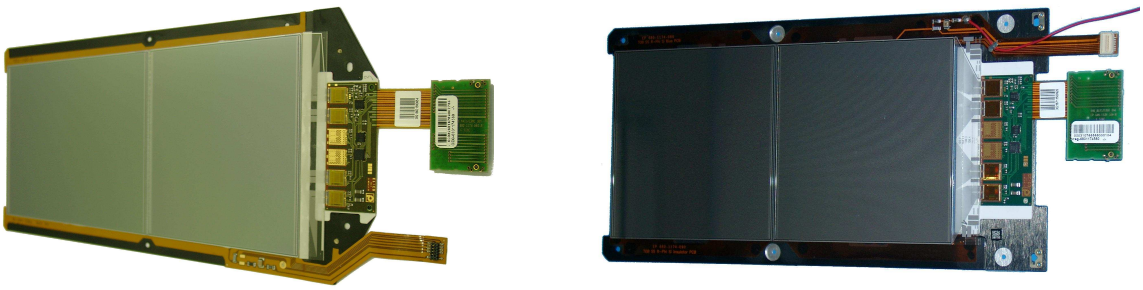

(a) (b)

Figure 3.5: *Complete modules of type (a) ring* 6 *and (b) OB2*

As the hit multiplicity, occupancy and radiation effects in the module scale with the position within the tracker, these aspects are considered in the choice of strip pitch and length and of the thickness of the bulk material. Occupancy considerations require sensors with a pitch from 80 μm to 120 μm and strip length around ≈ 10 cm for radii < 60 cm. For $r > 60$ cm a pitch from 80 μm up to 200 μm and a strip length of ≈ 20 cm is sufficient. The strip length of around 20 cm is obtained by daisy-chaining two sensors. The increased noise

[1]kapton polyamide film by DuPont is an electrical insulation material with outstanding thermal, mechanical, chemical and electrical properties (see [kap97])

due to the increased strip length is compensated by the usage of 500 μm thick sensors. In the inner part of the silicon tracker 320 μm thick sensors with a resistivity between 1.5 $k\Omega$ and 3.2 $k\Omega$ are used to be able to fully deplete detector modules after irradiation [sgu04]. The various types and geometries of sensors and modules of the silicon strip tracker are summarized in table C.1.

All silicon strip detectors are made of p^+-strips on n-doped bulk material, the p^+-strips are connected via polysilicon resistors to ground potential and readout capacitively. Radiation hardness is achieved by the usage of a multi-guard rings, metal over-hang technique (improves the breakdown voltage behavior) and using silicon with $< 100 >$ lattice orientation that gives a better Si-SiO_2 interface behavior. More details about the function of silicon detectors can be found in chapter 4 and section 4.3. During the operation and storage of the detector the temperature is kept below $-10°$C, to reduce the leakage current and slow down reverse annealing effects (see section 7.1).

3.3.3 Performance

The transverse momentum resolution for muons is $\approx 2\%$ or better for a transverse momentum $p_T < 100$ GeV/c and $|\eta| < 1.7$. For larger pseudo-rapidity ranges the performance decreases due to the reduced lever arm. The transverse impact parameter resolution for muons with $p_T = 100$ GeV/c is less than 20 μm for the whole pseudo-rapidity range covered by the tracker (see figure 3.6). The track reconstruction efficiency is close to 100% for muons over most of the pseudo-rapidity range, for pion and tracks within jets the reconstruction efficiency reduces to around 90% to 95% due to nuclear interactions [sgu04].

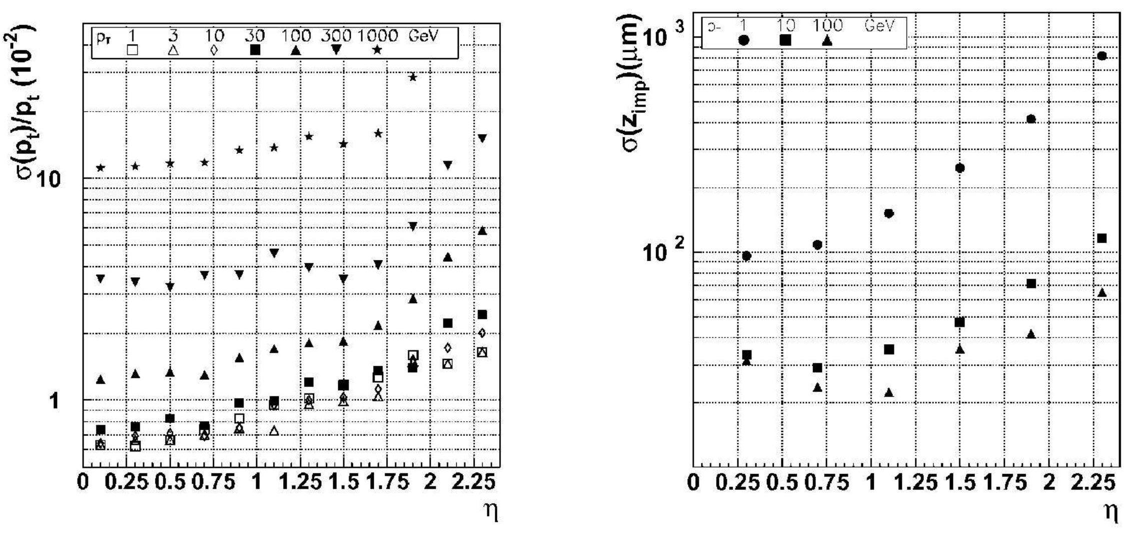

(a) (b)

Figure 3.6: *Transverse momentum resolution (a) and transverse impact parameter resolution* Z_{imp} *(b) as function of pseudo-rapidity for single muons with different* p_t *values [len01]*

3.3.4 Radiation Environment

The high particle collision rate and the beam energy of 7 TeV at the LHC lead to a harsh radiation environment where the silicon strip tracker has to be operated in. This has to be taken into account in the design and construction of the detector, as well as for the selection of the material used in the detector.

In the inner part of the tracker the radiation environment is dominated by secondary particles produced in the *pp* collisions, mainly charged hadrons. In the outer part of the tracker for radii larger then $\approx$ 50 cm neutron albedo from the surrounding electromagnetic calorimeter starts to dominate [CMS98, CMS00].

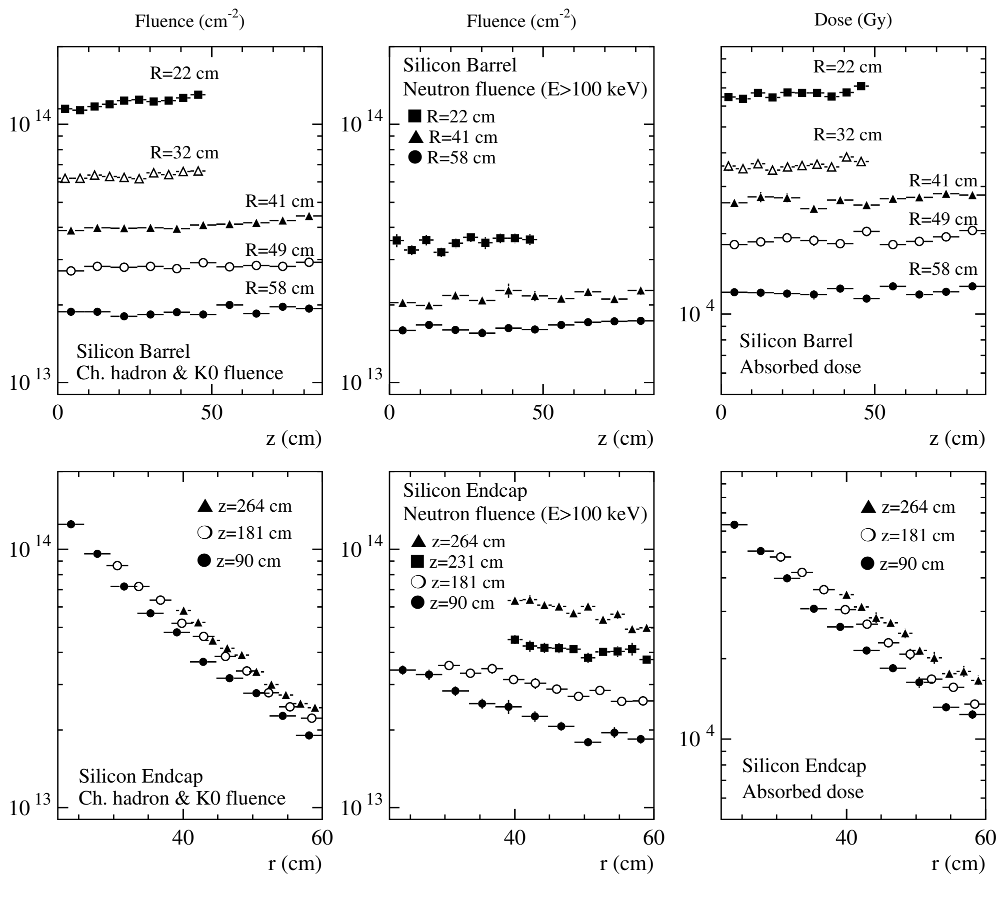

Figure 3.7: *Energy-integrated charged hadron and neutron fluences and absorbed dose in the silicon tracker. All values are for an integrated luminosity of* 5×10^5 pb^{-1}*, the fluence are scaled to* 1 *MeV-equivalent neutrons. For the end-cap disks the values are averaged over the radial range [CMS98]*

Figure 3.7 shows the expected fluence for charged hadrons, neutrons and the absorbed dose for different radii. From this one expects a maximum fluence of 1.6×10^{14} n_{1MeV} cm^{-2} for the TIB and the inner rings of the TID and TEC. TOB and the outer rings of the TEC will be exposed to a maximum fluence of 0.5×10^{14} n_{1MeV} cm^{-2} mainly from neutron albedo. Due to uncertainties in the expected fluences it is recommended to apply a safety factor of 1.5 for the TIB and 2 for the TOB fluence for irradiation studies and qualification of the detectors [CMS00].

Chapter 4

Semiconductor Radiation Detectors

The first section of this chapter summarizes basics on semiconductor physics in order to get an understanding of semiconductor devices and an insight of principles of semiconductor radiation detectors.

4.1 Basic properties of semiconductors

4.1.1 Energy Bands in Solids

The allowed energy states of electrons in solids are structured in energy bands, separated by a forbidden energy region. These energy bands can be calculated by solving the Schrödinger equation

$$\left[-\frac{\hbar^2}{2m}\nabla^2 + V(\vec{r})\right]\Phi_k(\vec{r}) = E_k\Phi_k(\vec{r}) \tag{4.1}$$

for a single electron problem. Using the *Bloch theorem*, which states that for a periodic potential energy $V(\vec{r})$ as given by the lattice periodicity, the solutions of the Schrödinger equation are of the form

$$\Phi_k(\vec{r}) = e^{j\vec{k}\vec{r}}U_n(\vec{k},\vec{r}) \ , \tag{4.2}$$

where k is the wave vector, n gives the band index and $U_n(\vec{k},\vec{r})$ is a periodic function in $\vec{r}$ with the periodicity of the direct lattice.

The energy band above the last completely occupied energy band is called *conduction band*, the energy band below are called *valence band*. The distance between the energy of the lowest edge of the conduction band and the energy of the highest edge of the valence band is called *bandgap* E_g. Figure 4.1 shows the energy band structure for the semiconductors Ge, Si and GaAs in momentum space, numerically calculated with the pseudopotential method [che76]. L, Γ (center of the first Brillouin zone) and X represent special symmetry points of the reciprocal lattice. Only for GaAs the bandgap lies at $k = 0$, therefore GaAs is called a *direct semiconductor*, Si and Ge are *indirect semiconductors*, which means that momentum transfer (e.g by thermal phonons) is needed to excite an electron from the valence band to the conduction band.

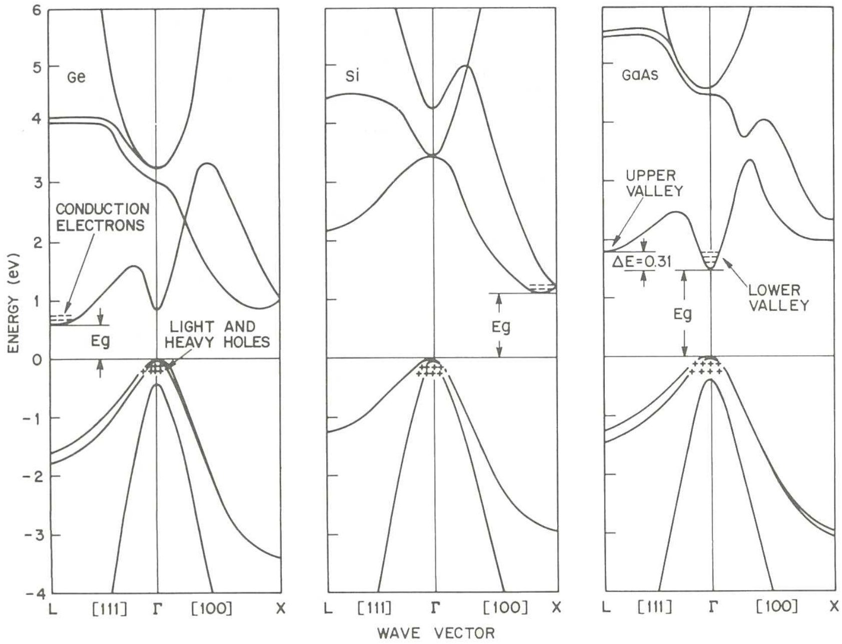

Figure 4.1: *Energy band structure for Ge, Si and GaAs plotted in energy-momentum plane. L, Γ and X are symmetry points of the lattice. (+) and (-) indicating holes and electrons in the according band* [sze81, che76]

4.1.2 Intrinsic Semiconductors

In an ideal pure and undisturbed semiconductor all charge carriers are descended from thermally broken lattice bindings. The number of occupied states in the conduction band is given by

$$n = \int_{E_c}^{\infty} N(E) \cdot F(E) \cdot dE \ , \tag{4.3}$$

where integration is done over all energies of the conduction band, starting at the lowest energy of the conduction band E_c. The *Fermi-Dirac distribution* $F(E)$ gives the occupation probability for an electron state

$$F(E) = \frac{1}{1 + e^{\left(\frac{E-E_f}{k_B T}\right)}} \ . \tag{4.4}$$

E_f is the *Fermi energy*, at this energy $F(E)$ is one half, T is absolute Temperature and k_B the Boltzmann constant. For $|E - E_f| < 3k_B T$, the Fermi-Dirac distribution $F(E)$ can be approximated by the *Boltzmann distribution*

$$F_n(E) \approx e^{-\frac{E-E_f}{k_B T}} \ . \tag{4.5}$$

The density of states $N(E)$ can be approximated by the density at the low energy edge of the conduction band. This is justified because for low temperatures and low carrier concentration only the states near the bottom of the conduction band are occupied.

$$N(E) = M_c \frac{\sqrt{2}}{\pi^2} \frac{(E - E_f)^{\frac{1}{2}}}{\hbar^3} (m_n^*)^{\frac{2}{3}} , \tag{4.6}$$

with M_c the density of equivalent minima in the conduction band (which can be set to 1 for the case of non degenerate energy bands) and m_n^* the density of states effective mass for electrons. Solving equation 4.3 the number of occupied states in the conduction band is given by

$$n = 2 \left(\frac{2\pi m_n^* k_B T}{\hbar^2} \right)^{\frac{2}{3}} M_c \cdot e^{-\frac{E_c - E_f}{k_B T}} = N_c \cdot e^{-\frac{E_c - E_f}{k_B T}} , \tag{4.7}$$

with the effective density of states in the conduction band N_c. In the same way the density of holes near the top of the valence band can be calculated

$$p = N_v \cdot e^{-\frac{E_v - E_f}{k_B T}} , \tag{4.8}$$

where N_v is the effective density of states in the valence band and E_v is the highest possible energy in it.

For intrinsic semiconductors the number of electrons and holes generated by thermal excitation is equal, $n = p = n_i$, where n_i is the intrinsic charge carrier concentration. With equation 4.7 and 4.8 the *Fermi level* calculates to

$$E_f = E_i = \frac{E_c + E_v}{2} + \frac{k_B T}{2} \cdot \ln \left(\frac{N_v}{N_c} \right) = \frac{E_c + E_v}{2} + \frac{3k_B T}{4} \cdot \ln \left(\frac{m_p^*}{m_n^* M_c^{2/3}} \right) \tag{4.9}$$

and for the intrinsic charge carrier density one gets

$$n_i = \sqrt{n \cdot p} = \sqrt{N_c N_v} \cdot e^{-\frac{E_c - E_v}{2k_B T}} = \sqrt{N_c N_v} \cdot e^{-\frac{E_g}{2k_B T}} . \tag{4.10}$$

4.1.3 Extrinsic Semiconductors

Inserting impurities (e.g. boron, phosphor) into the crystal lattice alters the materials properties, this is called doping. A doped semiconductor is also called *extrinsic semiconductor*. The silicon mono-crystal forms a diamond lattice, where every silicon atom has four nearest neighbors covalently bound to each other (intrinsic case). Replacing a silicon atom by an arsenic or phosphorous atom which has five valence electrons, only four are needed for the formation of covalent bonds, leading to an excess of electrons. This type of semiconductor is called *n-type semiconductor* and dopants are called *donors*. In the same way an excess of holes in a semiconductor can be obtained, by adding atoms with three valence electrons. These dopants are called *acceptors*, (e.g. boron) and the semiconductor is a *p-type semiconductor*.

The replacement of lattice atoms by dopants is accompanied by creation of new energy levels in the band gap. If the donor levels E_d are close to the conduction band (e.g for phosphorous $E_c - E_d = 0.045$ eV), these atoms will be completely ionized at room temperature. In the same way acceptor levels E_a close to the valence band are completely filled with electrons from the valence band leaving holes in the valence band (e.g for boron $E_a - E_v = 0.045$ eV).

The Fermi level for intrinsic semiconductors is very close to the center of the band gap (see equation 4.9). For extrinsic semiconductors the Fermi level must move towards the conduction band for n-type semiconductors or towards the valence band for p-type semiconductors, to preserve charge neutrality. The doping concentration usually is much higher than the intrinsic charge carrier concentration, one gets the Fermi level from equation 4.7 and 4.8 by replacing the charge carrier concentration with doping concentration

$$E_c - E_f = k_B T \ln \frac{N_c}{N_d} \quad \text{and} \quad E_f - E_v = k_B T \ln \frac{N_v}{N_a} \; . \tag{4.11}$$

The equation 4.7 and 4.8 for the charge carrier concentration can be rewritten in a more useful form using the intrinsic charge carrier concentration (equation 4.10) and the intrinsic Fermi level (equation 4.9)

$$n = n_i e^{\frac{E_f - E_i}{k_B T}} \quad \text{and} \quad p = n_i e^{\frac{E_i - E_f}{k_B T}} \; . \tag{4.12}$$

These equations lead to a fundamental property of charge carrier in semiconductors, the *mass action law*

$$n_i^2 = n \cdot p \; . \tag{4.13}$$

This equation depends not on the Fermi level and therefore the expression holds for the intrinsic and extrinsic case. See figure 4.2 for position of the Fermi level and the charge carrier concentration for the different cases discussed here.

4.1.4 Carrier Transport Phenomena in Semiconductors

So far the properties of semiconductors in equilibrium state were discussed. In the following sections the case of non equilibrium states are focused on. Non equilibrium states can be caused by the application of an electrical field (*drift*) or the presence of inhomogeneous charge carrier distributions (*diffusion*). Both cases are connected with current flow.

4.1.4.1 Drift

Without any field applied free charge carriers underlie only thermal motion. This thermal motion has the same probability in each direction and therefore the average displacement of a free charge carrier is zero.

In the presence of an electrical field the free charge carrier will be accelerated between two collision in the direction defined by the electrical field. The average drift velocity for electron and holes is given by

$$\begin{aligned} v_n &= -\frac{q\tau_c}{m_n^*}E = -\mu_n E \\ v_p &= \frac{q\tau_c}{m_p^*}E = \mu_p E \; . \end{aligned} \tag{4.14}$$

τ_c is mean free time between two collision ($\tau_c \approx 10^{-12}$ s), q the electric charge and $m_n^*(m_p^*)$ the electrons (holes) effective mass. Equation 4.14 holds for drift velocities small compared to thermal velocity ($v_d \ll v_{th}$). There are large deviations from Ohm's law for the case $v_d \approx v_{th}$, the critical electrical field for this case could be estimated by

$$|E_{\text{crit}}| = \frac{1}{\mu}\sqrt{\frac{3k_B T}{m_n^*}} \; . \tag{4.15}$$

Using 4.14 and $v_d = v_{th} = 10^7\,\text{cm}\,\text{s}^{-1}$ one gets the critical electrical field for electrons in silicon at room temperature to $|E_{\text{crit}}| \approx 10^4\text{Vcm}^{-1}$ (see figure 4.3).

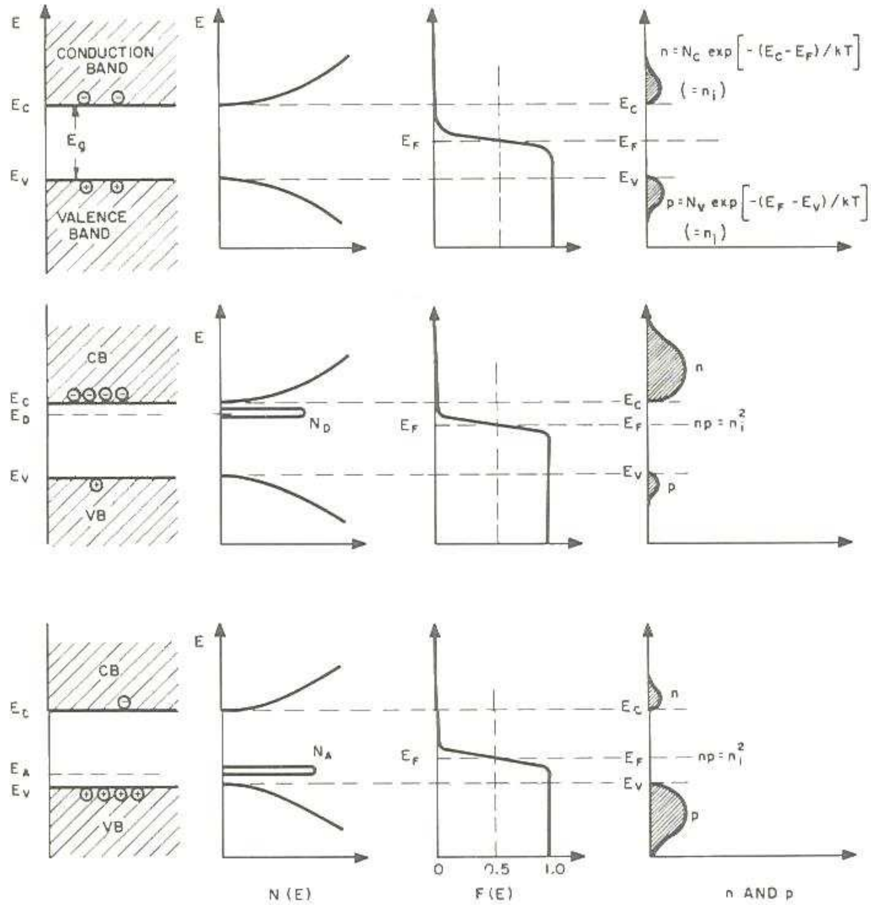

Figure 4.2: *Simplified schematic of the band diagram, followed by density of states, the Fermi-Dirac distribution and corresponding charge carrier concentration (from left to right), for intrinsic, n-type and p-type semiconductors (from top to bottom)* [sze81]

4.1.4.2 Diffusion

The diffusion process starts, if there are different concentrations of charge carriers. This process is dominated by statistics. Consider the electrons and holes as electrically neutral, the probability for an electron (hole) to come from the region of the higher concentration to the one with lower concentration by random movement is much higher than vice versa. The diffusion process smears out the charge distribution and can be described by the diffusion equation

$$
\begin{aligned}
F_n &= -D_n \nabla n \qquad (4.16)\\
F_p &= -D_p \nabla p \ .
\end{aligned}
$$

F_n (F_p) is the flux of electrons (holes) in the density gradient ∇n (∇p) and D_n (D_p) is the diffusion constant. Combining the motion in the presence of an electrical field E and diffusion

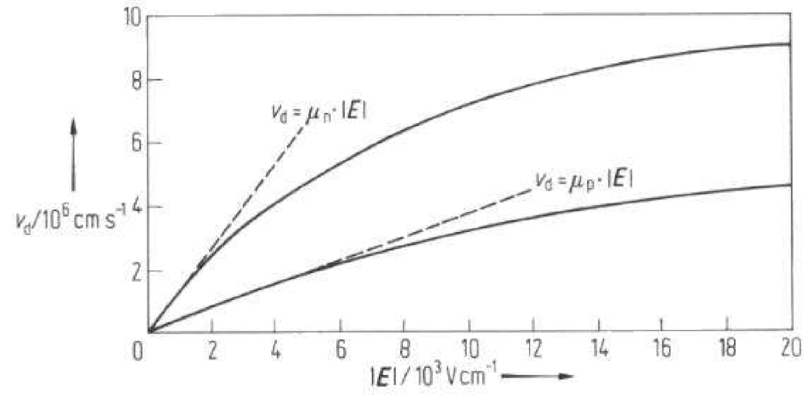

Figure 4.3: *Drift velocity of free charge carrier in silicon for different applied electrical fields* [ber92]

one finds for the total current density

$$\begin{aligned} j_n &= q\mu_n nE + qD_n \nabla n \\ j_p &= q\mu_p pE - qD_p \nabla p \ . \end{aligned} \tag{4.17}$$

In the equilibrium state the current density has to be zero. This delivers the connection between mobility and diffusion, the *Einstein equation*

$$\begin{aligned} D_n &= \frac{k_B T}{q}\mu_n \\ D_p &= \frac{k_B T}{q}\mu_p \ . \end{aligned} \tag{4.18}$$

4.1.5 Generation and Recombination of Charge Carriers

4.1.5.1 Thermal Generation

Thermal generation of charge carriers is one important process in semiconductors with regard to semiconductor radiation detector. The free charge originating from thermal generation contributes to the system noise (see section 4.3.3) and therefore influences the ability of signal detection.

For some direct semiconductors with a small band gap, the thermal energy at room temperature is high enough to directly excite electrons into the conduction band. In case of larger band gaps or for indirect semiconductors the thermal generation proceeds in two steps via energy levels in the band gap, caused by impurities and lattice defects. Furthermore to for indirect semiconductors momentum has to be transferred to excite electrons into conduction band.

4.1.5.2 Generation by Electromagnetic Radiation

Electron hole pairs can be created by electromagnetic radiation, which is the working principle of photo detectors and solar cells. If the energy of a photon is larger than the band gap, a electron can be lifted directly in the conduction band. Take into account that for indirect semiconductors an additional momentum transfer is needed, e.g. by absorbing a phonon. The electrons and holes move towards the band gap edges, emitting energy in form of lower energetic photons or phonons. Absorption of a photon with energies lower than band gap energy will take place via impurity or defect energy levels in band gap, here the photon is absorbed by an electron, which is lifted from the valence band into a mid gap energy state or from a mid gap energy state into the conduction band. The energy dependence of the penetration depth is shown in figure 4.4.

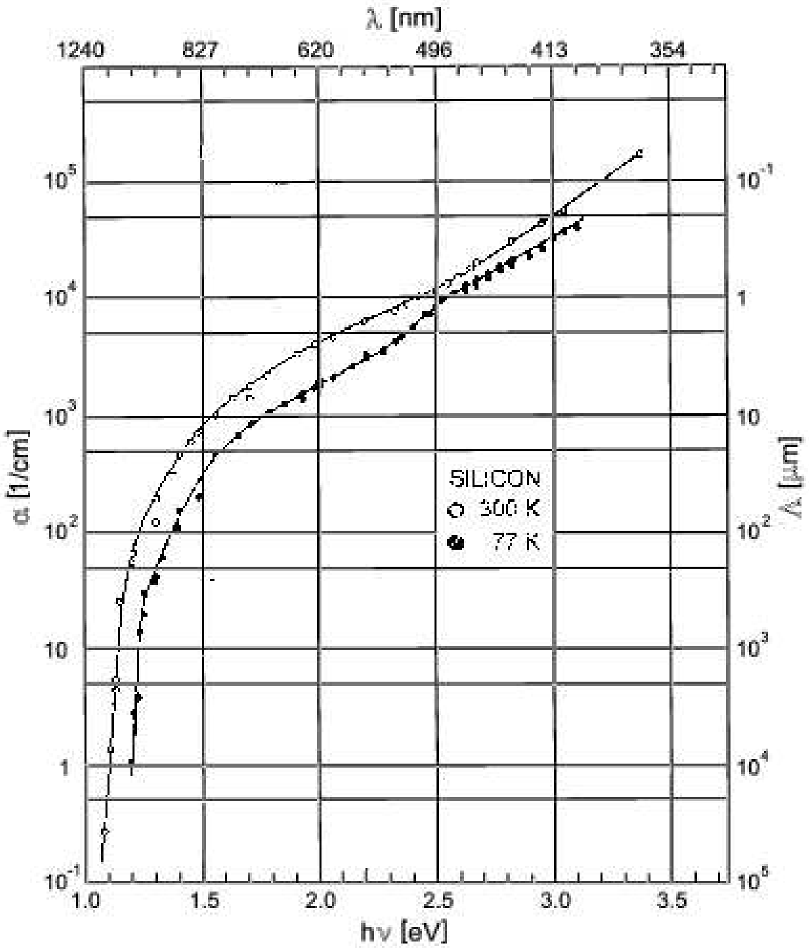

Figure 4.4: *Dependance of absorption coefficient and penetration depth on photon energy for silicon* [das55]

4.1.5.3 Generation by Charge Particles

A charged particle interacts with matter primarily through Coulomb force, producing many electron hole pairs along the particles track in the material. The production process can be a direct one, producing an electron hole pair or an indirect producing a high energy electron

(δ electron), that subsequently loses its energy by producing electron hole pairs. The energy loss of charged particles in matter is described by the *Bethe Bloch formula* [leo87]

$$\frac{dE}{dx} = 2\pi N_A r_e^2 m_e c^2 \rho \frac{Z}{A}\frac{z^2}{\beta^2}\left[\ln\frac{2m_e\gamma^2 v^2 W_{max}}{I^2} - 2\beta^2 - \delta - 2\frac{C}{Z}\right] , \tag{4.19}$$

where $2\pi N_A r_e^2 m_e c^2 = 0.1535\frac{\mathrm{MeVc}^2}{\mathrm{g}}$, A and Z the atomic mass and atomic number of the absorber material, z the electric charge of the incident particle. W_{max} is the maximum kinetic energy which can be transfered in a single collision, δ is a correction due to density effects and the term $\frac{C}{Z}$ considers shell corrections only relevant at very low energies.

The energy loss of a charge particle in matter is of stochastic nature. The probability distribution function (pdf) describing the energy loss Δ in an absorber of thickness x is called *Landau distribution*.

$$f(x,\Delta) = \frac{1}{\xi}\frac{1}{\pi}\int_0^\infty e^{-u\ln u - u\lambda}\sin(\pi u)du \tag{4.20}$$

with $\lambda = \frac{1}{\xi}\left[\Delta - \xi\left(\ln\xi - \ln\epsilon + 1 - \gamma_e\right)\right]$, ξ the mean energy loss and γ_e the Euler's constant. The quantity ϵ represents the minimum energy transfer and can be calculated by $\ln\epsilon = \ln\frac{(1-\beta)I^2}{2mc^2\beta^2} + \beta^2$ [leo87].

For detector calibration the most probable energy loss per unit thickness is the more relevant quantity. Because of the long tail of the distribution due to high energy loss events, which are hard to extract from background, makes the mean energy loss difficult to determine. The most probable energy loss is about 70% of mean energy loss calculated by equation 4.19 [hag02].

4.1.5.4 Recombination

There exist several *recombination* processes to restore the thermal equilibrium of the semiconductor. This can take place by a band to band transition, where the energy (at least the band gap energy) discarded by the emission of a photon (radiative recombination), energy transfer to another free electron (Auger recombination) or the emission of phonons (multi-phonon process). In indirect semiconductors the band to band transition is highly suppressed. A more effective process is the recombination on deep defect levels. These levels have to be capable to capture and emit electrons and holes.

4.2 Basic Semiconductor devices

The following section describes basic semiconductor devices needed to build up semiconductor radiation detectors, such as pixel and strip detectors. Also parts common in readout electronics will be introduced.

4.2.1 pn-Junction

The *pn-junction* is obtained by joining two semiconductors of opposite doping. It is the main structure used in silicon radiation detectors. In the equilibrium case before getting the two semiconductors in contact, electron and holes are homogeneously distributed in their respective volume. When getting in contact, holes from the p-side diffuse into the n-side recombinining with electrons and electrons from the n-side diffuse into the p-side recombining with holes. The remaining doping atoms creating the so called *space charge region* near the contact. This causes an electrical field contrary to the diffusion process, removing all free charge carriers from the region around the junction (see figure 4.5). The *built-in voltage* can be calculated from the difference in the intrinsic energy levels.

$$V_{bi} = \frac{1}{e}\left(E_i^p - E_i^n\right) = \frac{k_B T}{e} \ln\left(\frac{N_a N_d}{n_i^2}\right) \tag{4.21}$$

N_a and N_d is the number of acceptor and donor atoms respectively. The width of the space-charge region can be obtained by using the Schottky approximation (abrupt pn-junction) and charge neutrality

$$\begin{aligned} d_n &= \sqrt{\frac{2\epsilon\epsilon_0}{e}\frac{N_a}{N_d(N_a+N_d)}V_{bi}} \\ d_p &= \sqrt{\frac{2\epsilon\epsilon_0}{e}\frac{N_d}{N_a(N_a+N_d)}V_{bi}}\ . \end{aligned} \tag{4.22}$$

If an external voltage is applied the the variation of total electrostatic potential is $V_{bi} - V$ and equation 4.22 expands to

$$\begin{aligned} d_n &= \sqrt{\frac{2\epsilon\epsilon_0}{e}\frac{N_a}{N_d(N_a+N_d)}\left(V_{bi}-V\right)} \\ d_p &= \sqrt{\frac{2\epsilon\epsilon_0}{e}\frac{N_d}{N_a(N_a+N_d)}\left(V_{bi}-V\right)}\ . \end{aligned} \tag{4.23}$$

For a forward biased diode the space charge region shrinks, for a reversed biased diode the space charge region increases. In the case of an asymmetric junction the space charge region covers mainly the low doped bulk material. The voltage needed to increase the space charge region over the complete diode's thickness is called *depletion voltage*.

$$V_{dep} = \frac{e}{2\epsilon\epsilon_0}\left|N_{\text{eff}}\right| d^2\ , \tag{4.24}$$

where $N_{\text{eff}} = N_d - N_a$ is the effective doping concentration, given by the difference between the concentration ionized donors and acceptors in the space charge region.

The total current can be described in good approximation by the minority carrier (electrons in the p-region and holes in the n-region) diffusion currents at the edges of the neutral regions. The voltage current relationship can be expressed by the ideal *diode's law*

$$J = \left(J_{s_n} + J_{s_p}\right)\left(e^{\frac{eV}{k_B T}} - 1\right) = J_s\left(e^{\frac{eV}{k_B T}} - 1\right)\ . \tag{4.25}$$

J_s is the reverse bias saturation current, which can be obtained by solving the time-independent continuity equation for minority carriers applying the boundary condition of no minority carriers at the edges of the space charge region

$$J_s = e\left(\frac{n_{p0} D_n}{\sqrt{D_n \tau_n}} + \frac{p_{n0} D_p}{\sqrt{D_p \tau_p}}\right)\ . \tag{4.26}$$

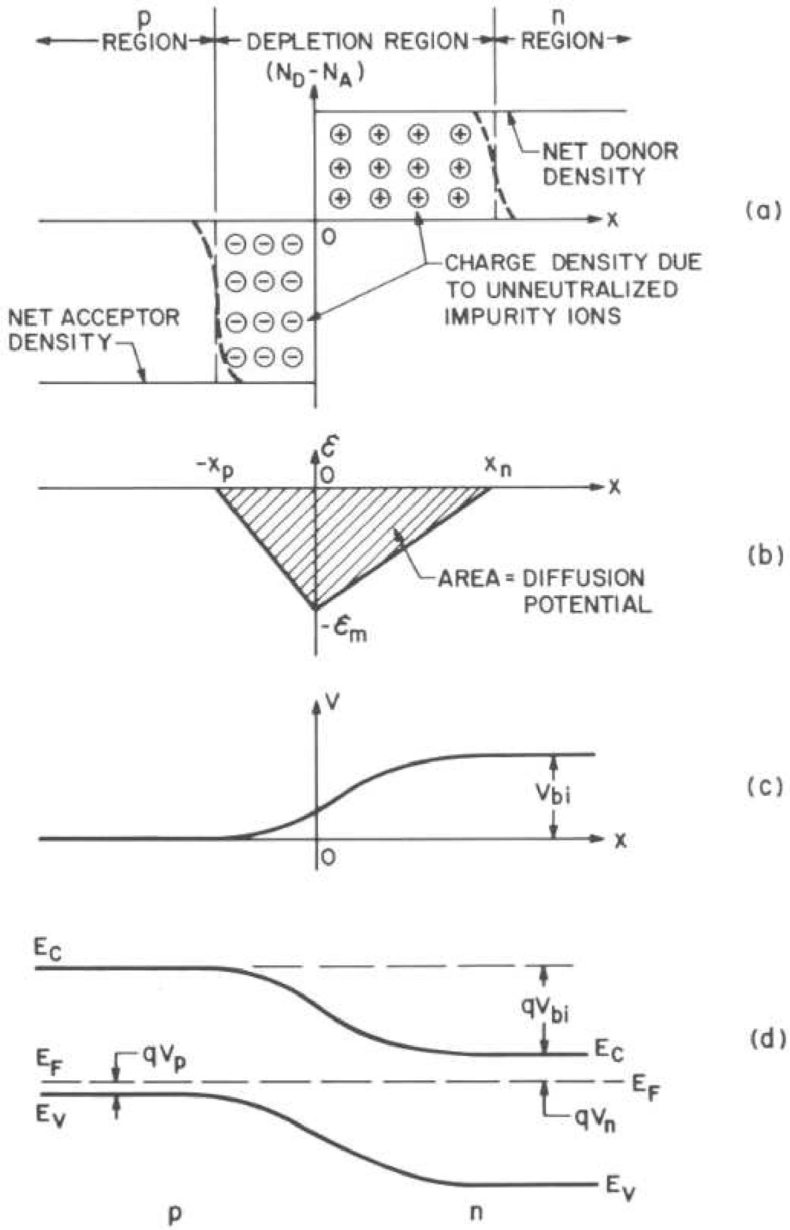

Figure 4.5: *pn-junction in thermal equilibrium, (a) space-charge region, (b) electric field , (c) potential variation with distance where V_{bi} is the built-in potential, (d) energy band* [sze81]

With $\tau_{n,p}$ the carrier lifetime. The above expression was derived for the assumption that no charge is generated in the space charge region, which does not hold for reversed biased diodes. In the case of reverse bias the product $n \cdot p$ falls below n_i and generation dominates. The generation current can be estimated by product of the generation rate ($G_{th} = \frac{n_i}{\tau_g}$, with τ_g

generation lifetime of minority carriers) and the change in the depletion volume

$$J_v = e\frac{n_i}{\tau_g}\left(d - d_0\right) \ , \tag{4.27}$$

d_0 is the depletion depth for no external field applied.

4.2.2 Metal Semiconductor Contact

When metal makes a contact with a semiconductor, a barrier (Φ_{ba}) will be formed at the metal-semiconductor interface. Figure 4.6 shows the evolution of the energy bands after contacting the semiconductor.

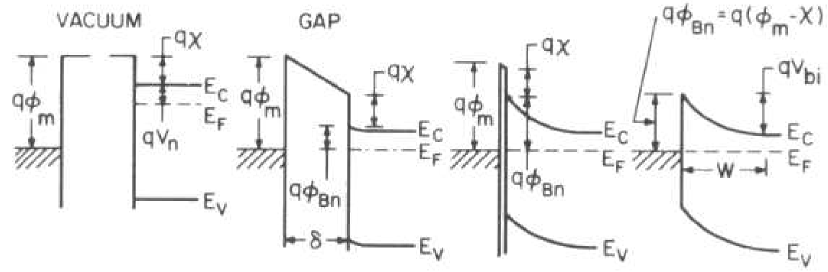

Figure 4.6: *Energy band diagram for metal semiconductor contact, evolution to thermal equilibrium, χ is the electron affinity, Φ_m the metals work function, V_n the energy difference between E_c and the Fermi level in the semiconductor and Φ_{bn} the barrier height,* [sze81]

The Fermi level of semiconductor is lowered by the difference of work functions, bending the energy bands near contact. The *work function* is the difference between Fermi level and vacuum level. From figure 4.6 one can see the barrier height, which an electron from the metal has to overcome to reach the semiconductor. The height of the barrier does not change if an external voltage is applied, but the threshold for electrons against movement from the semiconductor into the metal will change with the applied voltage. The metal semiconductor contact has a rectifying behavior, a similar current voltage relationship as for the pn-junction can be found

$$J = J_s\left(e^{\frac{qV}{k_B}T} - 1\right) \ , \tag{4.28}$$

with a saturation current

$$J_s = A^* T^2 e^{-\frac{e\Phi_{bn}}{k_B T}} \tag{4.29}$$

A^* is the effective Richardson constant, $e\Phi_{bn}$ the barrier height.

4.2.2.1 Ohmic Contact

A contact with negligible resistance relative to semiconductor material is defined as *ohmic contact.* It should not degrade the device performance. To receive an ohmic contact, either a low barrier height is needed or a high doping concentration in surface layer of the semiconductor, as then the barrier width become narrow and in addition to thermic emission of electrons, the process of tunneling becomes an important current source.

4.2.3 Metal Oxide Semiconductor (MOS) Structure

The *metal insulator semiconductor* (*MIS*) structure is a useful device to study surface defects and is a common building block of various detectors, such as charge coupled devices (CCD) and modern microelectronics. In the case of silicon a common insulator is silicon oxide, then the structure is called *metal oxide semiconductor* (*MOS*) structures.

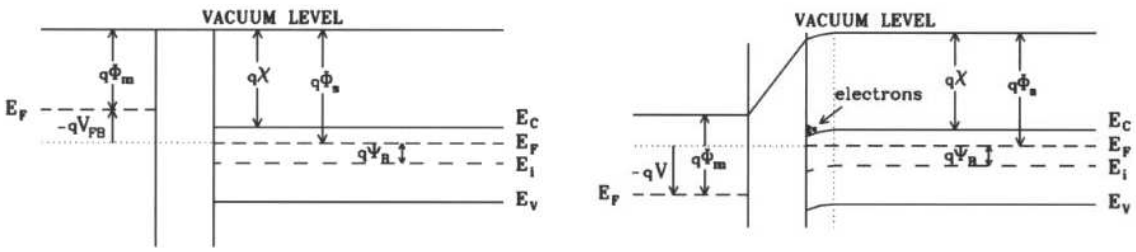

(a) $V = V_{fb}$ (b) $V > V_{fb}$

Figure 4.7: *Energy band diagram for a n-type MOS structure, (a) flat band condition, (b) accumulation,* [lut99]

In figure 4.7a the different operation modes for a MOS structure is shown. In the *flat band condition* the charge carrier concentration in the semiconductor is uniform up the boundary with the oxide, the electric field in the semiconductor is zero. Since the working function of the semiconductor and metal are different, a voltage

$$V_{fb} = \Phi_m - \Phi_s \tag{4.30}$$

has to be applied to achieve the flat band condition. This voltage is called *flat band voltage.*

If a voltage $V \geq V_{fb}$ is applied across the n-type MOS structure the potential at the semiconductor oxide interface moves in positive direction and the energy bands bend downwards in the interface region (see figure 4.7 b).

The distance between Fermi level and conduction band decreases and therefore the electron concentration near oxide interface increases due to exponential dependence of the charge carrier concentration on the energy difference $(E_c - E_f)$. This is the accumulation case.

Applying a voltage $V \leq V_{fb}$ across the n-type MOS structure, the energy bands bend upwards and the electron concentration at the interface decreases. This is called depletion case.

Decreasing the voltage further, the energy bands at the interface bend even more upward, and the intrinsic Fermi level (E_i) will equal or even cross the Fermi level (E_f). This is called inversion (see figure 4.8), one distinguishes between weak inversion where the hole concentration is smaller than the electron concentration and the strong inversion, where the hole concentration is higher than the electron concentration in the bulk.

All considerations above are true for the case of no oxide charge. In the presence of charge in the oxide the voltage threshold voltages of the different cases will change and therefore the MOS structure is a good device to investigate surface damage.

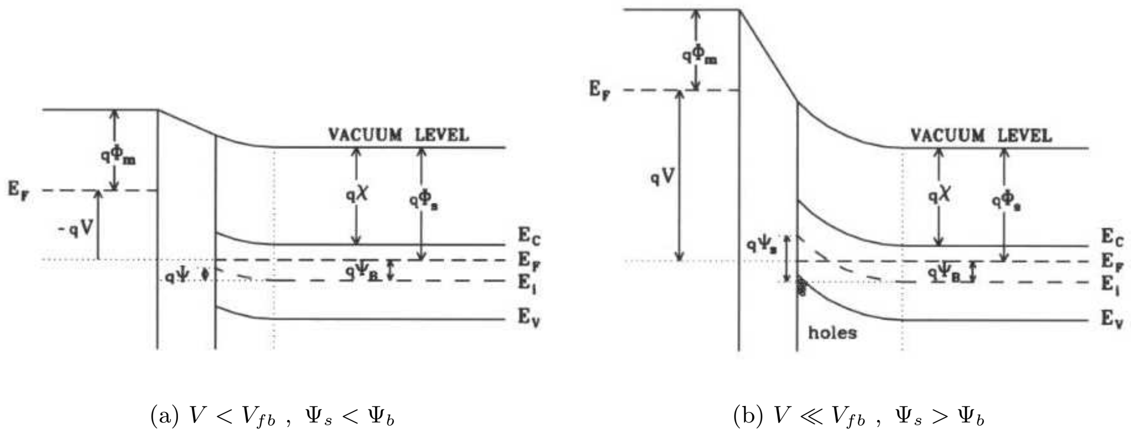

Figure 4.8: *Energy band diagram for a n-type MOS structure, (a) surface depletion, (b) inversion,* [lut99]

4.2.4 $n^+ - n$ Transition

The same effects discussed in section 4.2.1 occur for single type semiconductors, when the doping concentration changes, as for $n^+ - n$ *-junctions*. The abrupt change in charge carrier concentration let electrons diffuse from the highly doped n^+-side to the n-side, with lower electron concentration. Leaving a positive charged region in the n^+-side near the junction and a negative charge region in the n-side, building up an electric field acting contrary to the diffusion process.

4.2.5 Field Effect Transistor (FET)

Field effect transistors (*FET*) are widely used both in analog signal processing and digital circuits. In this section the principle of the field effect transistor will be explained to understand its application in the readout electronics (see section 5.1) and the consequences arising from radiation damage (see section 7.1).

In figure 4.9 the profile of a n-type FET is shown, it consists of p-type gates on a n-type substrate. The ohmic contacts on both ends of the substrate function as source and drain. If a voltage is applied at the drain, which is more positive compared to source, electrons move from the source to drain. The gate controls the width of the depletion layer, the conduction is limited to the space between the depletion layers.

4.2.5.1 MOS-FET

The metal oxide semiconductor field effect transistor (*MOS-FET*) is widely used in integrated circuits, microprocessors, semiconductor memories, power devices and high density detector read-out electronics. The difference to the FET is that in a MOS-FET the conductance is changed by the effective area of the conductive channel and the charge carrier concentration.

Figure 4.10 shows a schematic of a MOS-FET. In the p-type substrate n^+ implants form the source and drain contact. The gate is a metal contact on an insulating oxide layer between

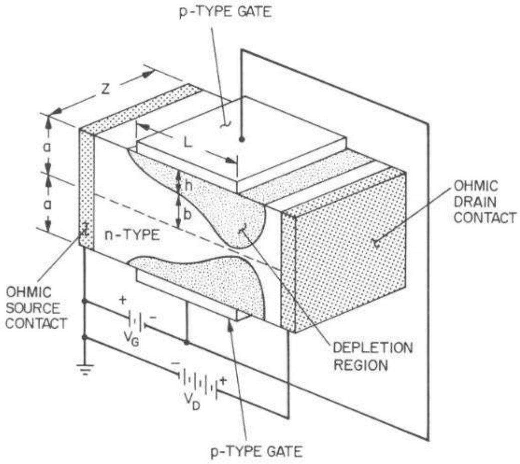

Figure 4.9: *Schematic of of a junction field effect transistor, p-type gates on n-type substrate, the ohmic contacts to the n-substrate act as source and drain,* [sze81]

the source and drain.

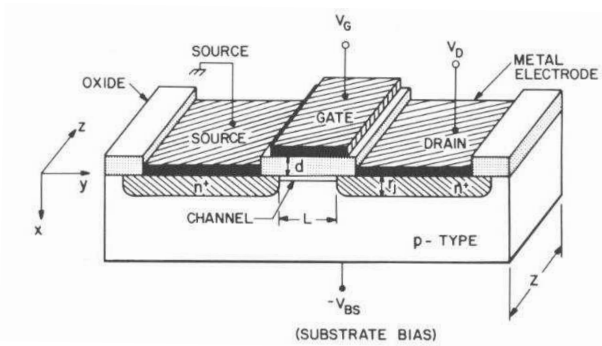

Figure 4.10: *Schematic of a MOSFET, the gate is decoupled by an oxide layer, the source and drain formed by highly doped n-type, the substrate is of p-type semiconductor,* [sze81]

Without applied gate voltage V_g one of the highly doped n-type regions is operated in reverse bias condition and therefore no current will flow. If a positive gate voltage is applied negative charge is induced near the interface of the oxide and p-type region. Increasing the gate voltage leads to further bending of the energy bands and the creation of an inversion layer (see section 4.2.3 and figure 4.8b).

The conductance of the inversion layer can be altered by the applied gate voltage. The voltage on the back surface contact V_{bs} can be ground (reference voltage) or reverse biased, this will also effect the conductance channel.

4.3 The CMS Silicon Detectors

Silicon detectors are mainly reverse biased pn-junctions, which are shaped or segmented for their designated application. In this section the structure of silicon detectors are shown with respect to their application in the CMS experiment.

4.3.1 Strip Detectors

Silicon strip detectors are used for precise position measurements, as lithographic technology enables to integrate many p^+ strips into n-bulk material of the sensor, with a typical pitch of 60...100 nm (it also possible to use a p-bulk with n^+ strips). When electron hole pairs are created in the detectors bulk material by processes discussed in section 4.1.5 they move along the field lines resulting in a signal on the corresponding strips. The position of the traversing particle is then calculated by the center of gravity of the pulse height distribution of the strip signals.

Figure 4.11 shows a schematic view of a strip sensor as it is used for the CMS Silicon Strip Tracker. It consists of a n-type bulk with p^+ strips forming the pn-junction and uniformly metalized n^+ layer on the back side providing an good ohmic contact. This highly doped n^+ layer acts as barrier for minority carriers coming from the depleted bulk region and for majority carriers injected from the metal contact, keeping the leakage current low. The n^+ implant along the edges of sensor prevents the space charge region from reaching the cutting edges.

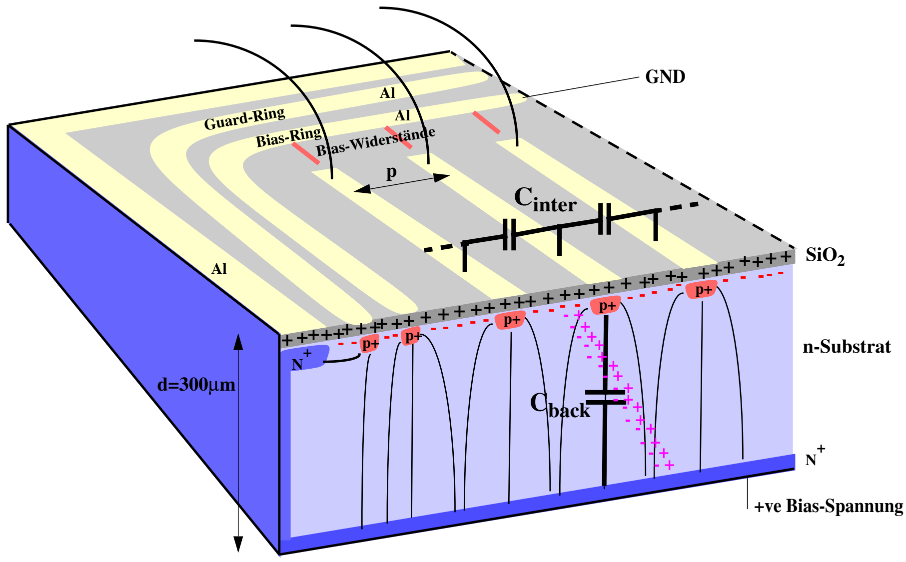

Figure 4.11: *Schematic of a silicon strip sensor,on n-substrate* [fel01]

Around the active sensor region there are two p^+ ring structures covered with aluminum. The outer one, the *guard ring* degrades the electric field between n^+ at the sensor edges and the p^+ strips. The inner one, the *bias ring* is connected to ground potential and biases the p^+ strips via radiation hard poly silicon resistors. The aluminum read-out strips are capacitively coupled to p^+ implants, this coupling is achieved by multi-layers of SiO_2 and Si_3N_4.

All aluminum strips and rings are on both sides around 15% wider than the implants underneath. This *metal overhang* moves the high electrical field region from the p^+ implants into the oxide layer, allowing to operate the detectors at higher bias voltages [agr03, bor03], which is important in order to operate the detector after irradiation (see chapter 7.1).

4.3.2 Pixel Detectors

Even better spatial resolution can be achieved by shrinking the electrode size, therefore the large area diode is divided into many small pads or pixels. In the case of the CMS pixel detector a square shaped pixels size of $150 \times 150 \mu m^2$ is adopted (see figure 4.12) [kot01], thus providing a spatial resolution of a few micrometers is achieved. Moreover, the small active cells make this type of detectors particular appropriate in high flux regions (around the interaction point) of the experiment.

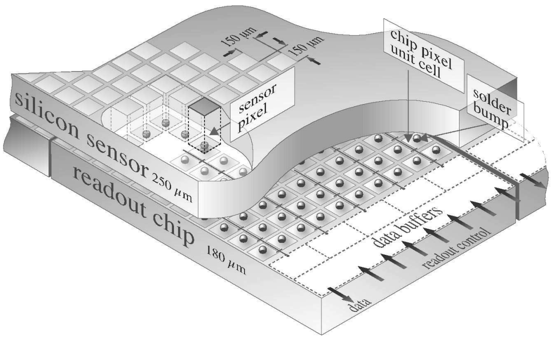

Figure 4.12: *Schematic view of a silicon pixel sensor with bump bonded read-out electronics* [CMS98]

4.3.3 Detector Noise

An important parameter in the operation of a detector is its noise performance, which significantly influences the signal detection capability. One source of noise is the read-out electronics, but also the detector itself generates noise. Figure 4.13 shows a schematic of a detector front-end. The detectors is represented by its capacitance C_d, the bias voltage is applied via resistor

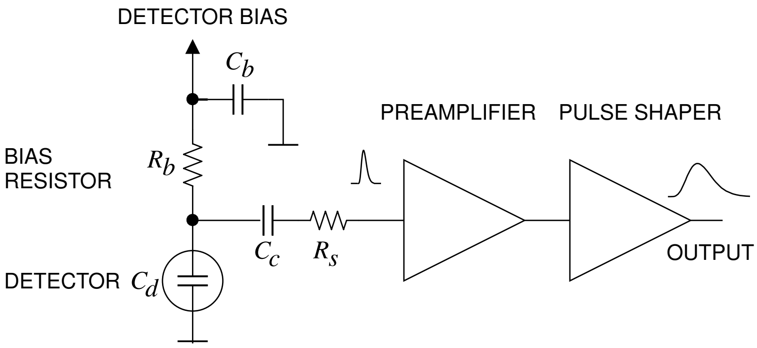

Figure 4.13: *Schematic model of a detector and front end circuit* [hag02]

R_b, the signal is coupled to the preamplifier through a coupling capacitor C_c. All resistances present in the signal input path are represented by the series resistance R_s. For noise analysis modules the noise sources by current and voltages sources, as shown in figure 4.14. The leakage current of a semiconductor detector fluctuates due to the statistical emission of electrons.

This is called "*shot noise*" and is modeled as current source in parallel with the detector. Thermal velocity fluctuations of charge carriers in resistors are contributing to noise and can be modeled either as voltage or current noise source. Resistors in series with the input act as voltage noise sources, resistors shunting the input act as current sources. The capacitor

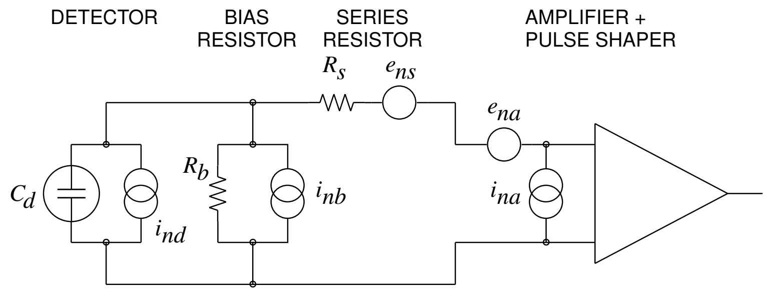

Figure 4.14: *Equivalent circuit for noise analysis* [hag02]

C_b (see figure 4.13) passes voltage fluctuations to ground, therefore, the bias resistor shunts the input and acts as current source i_{nb}. The same effect has the shot noise current from the detector i_{nd}. These noise sources are called parallel [hag02].

Table 4.1 shows the main noise source, types and formulas for the evaluation of the equivalent noise charge (ENC) for both read-out modes of the APV (peak and deconvolution mode, see section 5.1). The total capacitance C_{tot} can be calculated from the measured values

Noise source	**Type**	**ENC (RMS e^-)**	**expression for $T = -10°$C**	**deconvolution**
Reverse bias current i_nb	parallel	$\frac{e}{q_e}\sqrt{\frac{q_e i_{nb} T_s}{4}}$	$\approx 108 \cdot \sqrt{i_{nb}(\mu\text{A}) T_s(\text{ns})}$	$\times 0.45$
Bias resistance R_{poly}	parallel	$\frac{e}{q_e}\sqrt{\frac{k_B T T_s}{2R_{poly}}}$	$\approx 22.5 \cdot \sqrt{\frac{T_s(ns)}{R_{poly}(M\Omega)}}$	$\times 0.45$
Metal strip resistance R_s	series	$\frac{e}{q_e} C_{tot} \cdot \sqrt{\frac{k_B T R_s}{6T_s}}$	$\approx 13 \cdot C_{tot}(pF)\sqrt{\frac{R_s(\Omega)}{T_s(ns)}}$	$\times 1.45$
Front-end electronics	series	$(246 + 36 \times C_{tot}(pF))$	-	$(396 + 59 \times C_{tot}(pF))$

Table 4.1: *Noise sources, types and relative ENC evaluation formulas. T_s is the shaping time, q_e the electron charge, e the Euler number, C_{tot} the total capacitive load seen by the amplifier* [CMS98, CMS00]

of the coupling capacitance C_c, the inter-strip capacitance C_{int} and the calculated value for strip to backplane capacitance C_{back} to

$$C_{tot} = \frac{C_c C_{strip}}{C_c + C_{strip}} \tag{4.31}$$

with $C_{strip} = C_{back} + 2C_{int}$ and assuming that only the direct neighbors inter-strip capacitance contribute to the strip capacitance. The CMS sensor specifications forsee a coupling capacitance of $C_c = 1.2$ pF/(cm μm) for the strip length in cm and the implant width in μm and for C_{strip} a value around 1.3 pF/cm. The metal strip resistance R_s corresponds to the cross sectional area and the length of the strip.

Table 4.2 lists the ENC for an OB2 module. The total capacitance and the strip resistance were calculated using the strip dimension for the implant (width 46.0 μm and length 9.1cm) and the aluminum strip (width 58.0 mum, length 9.1cm and thickness 1.2 μm) as given in [bor03]. Additionally the resistance and capacitance of the pitch adapter had been considered ($R_{PA} \approx 20 - 60\ \Omega$ [ray01] and $C_{PA} \approx 1$ pF [mig02]). The resulting values from these calculation are $C_{tot} = 16.33$ pF and $R_s = 130\Omega$. The sampling time of the readout chip is $T_s = 50$ ns, the poly resistor is $R_{poly} = 1.85\ M\Omega$ and for the reverse bias current values were chosen from measurements on module 671 presented in section 7.5 (0.5 μA for the non-irradiated and 1300 μA for the irradiated case both at $-10°$C).

Noise source	**peak mode** [ENC (RMS e^-)]	**deconvolution mode** [ENC (RMS e^-)]
Reverse bias current	24 – 1217	11 – 548
Bias resistance R_{poly}	165	74
Metal strip resistance R_s	340	493
Front-end electronics	830	1354
Squared sum	913 – 1521	1443 – 1543

Table 4.2: *Equivalent noise charge for OB2 module, calculated with* $T_s = 50$ *ns, reverse bias current ranging from* 0.5 μA *to* 1300 */muA*, $R_{poly} = 1.85\ M\Omega$, $R_s = 130\Omega$ *and* $C_{tot} = 16.33$ *pF*

The most probable energy loss of a minimum ionizing particle (MIP) will produce about 36750 electrons seen in the signal. Therefore on expects a signal to noise ratio (SNR) for non-irradiated OB2 module of 40 in peak mode and 25 in deconvolution mode. After irradiation to a fluence expected for the outer barrel region of CMS the SNR will decrease to 24 in peak mode and 23 in deconvolution mode. In the calculation for the irradiated case only the increase in the leakage current has been taken into account, but there may be also charge trapped in defect levels (see section 7.1.5.3) or a change in the detector capacity directly entering in the total noise. Anyhow, the values given for the SNR are maximum ratings since the effective thickness of the space charge region is reduced by the conductive n^+ layer providing an ohmic contact between silicon and aluminum. Noise sources from other electronic parts in the readout lines (line drivers, the front end driver (FED)) are also not considered in these calculations.

Chapter 5

The Front End Hybrid of CMS Silicon Strip Detectors

The front-end hybrid supports all application specific integrated circuits (ASICs) needed to readout and control signal processing of the individual channels. In the following the main application are presented.

5.1 APV

The analog pipeline voltage chip (APV) enables signal processing of 128 channel readout channels of the silicon strip tracker. Each channel consists of a low noise preamplifier with shaper, a 192-cell analog pipeline and an analog pulse shape processor (APSP).

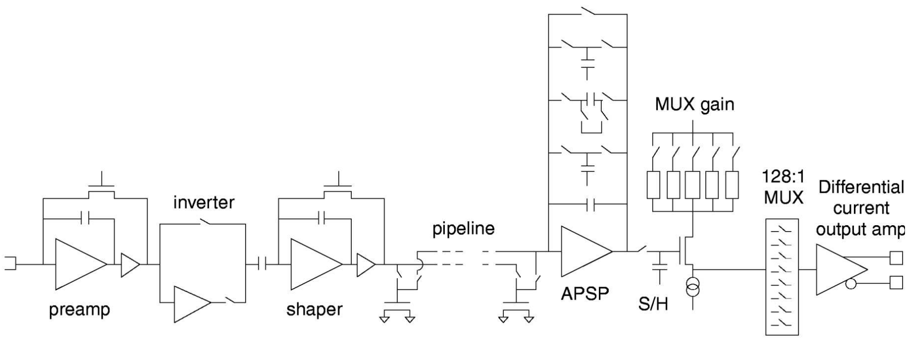

Figure 5.1: *APV block diagram, showing the schematic signal path of one channel from the input to its connection to* 128 : 1 *multiplexer and the differential output driver [fri01]*

Figure 5.1 shows a block diagram of one APV channel. The incoming signal from the detector is integrated in the preamplifier, afterwards the signal polarity can be changed in the inverter stage, giving the possibility to handle both signal polarities without loosing information due to the limited range of the chips power supply. The next stage is a $CR-RC$ shaper with 50 ns peaking time. The output of the shaper is stored into an analog pipeline with a 40.08 MHz sampling time (system clock). From the pipeline the signal is fed into the APSP, if requested by a trigger decision. From a sample and hold stage the data is sent to the 128 : 1 multiplexer, where all 128 channels are multiplexed to a single amplifier with a differential output.

5.1.1 Preamplifier and Shaper

The preamplifier (see figure 5.2) is a charge integrating amplifier made of a single-ended cascode amplifier with a 0.15 pF feedback capacitor. A switchable inverter with unity gain is placed at preamplifier's output to allow the use of the full dynamical range of the shaper for either signal polarity, only limited by the 2.5 V of the power supply. The preamplifier bias

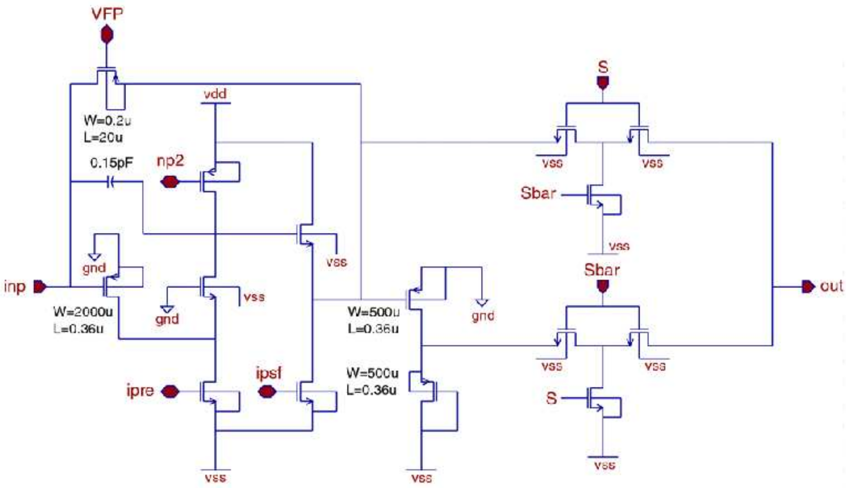

Figure 5.2: *Schematic of the APV preamplifier stage [jon99]*

current (IPRE), the cascode bias current (np2), the source follower bias current (IPSF) and the feedback bias voltage (VFP) can be adjusted to compensate radiation induced detoriations or temperature effects [ray00, jon01].

The shaper (see figure 5.3) is a $CR-RC$ filter, with a 0.15 pF capacitor and shaping time constant of 50 ns. Its input is coupled to the preamplifiers output with a 1.4 pF capacitor. The shaper input bias current (isha), the shaper feedback voltage (VFS) and the shaper source follower current can be adjusted to partly compensate the degradation of the pulse shape caused by irradiation.

5.1.2 Pipeline Cells

The APV uses the analog pipeline to buffer the data, thus giving sufficient time for the *level one trigger* decision whether the data sample is read out or not. The pipeline is realized as ring buffer of 192 cells with cycling write and read pointers. This allows a maximum time for the trigger decision of up to 4.8 μs. In order to prevent data from being overwritten, the pipelines addresses marked for read-out are stored in a 32 addresses deep FIFO register. Once a pipeline cell is marked it cannot be overwritten until the data is read-out.

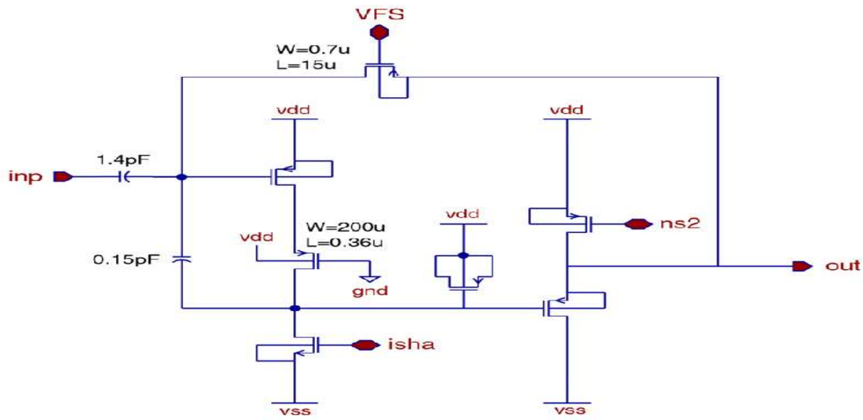

Figure 5.3: *Schematic of the APV shaper stage [jon99]*

5.1.3 Analog Pulse Shape Processor (APSP)

The signals arriving from the detector are integrated in the preamplifier, then shaped by the $CR - RC$ filter to well defined voltage pulses of $\approx$ 100 ns full width half maximum and afterwards stored in pipeline cells. Each channel marked for read-out passes the APSP circuit, which can be operated in two modes. In *peak mode* only one pipeline cell is read out, corresponding to the peak voltage of the shaped signal. The peak mode is used at low data rates, foreseen for the low luminosity phase of the LHC, when pile-up effects of the detector signals are negligible.

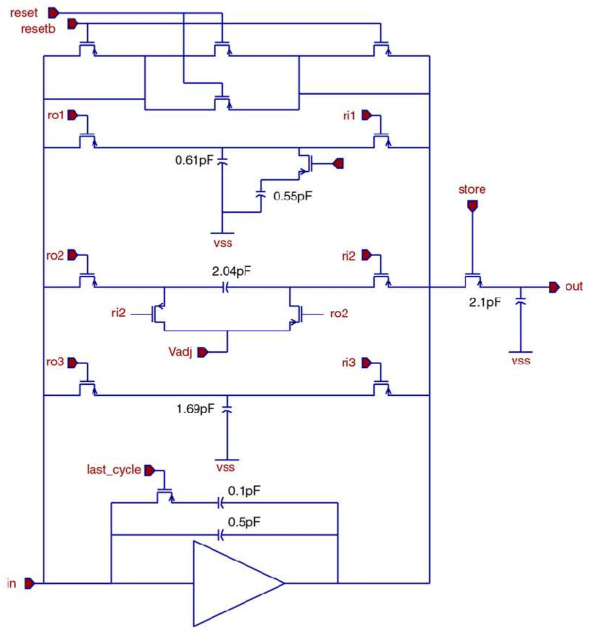

Figure 5.4: *Schematic of the APVs analog pulse shape processor (APSP) [jon99]*

For higher data rates the deconvolution mode is used. Here three pipeline cells are reserved by the trigger decision and read out in the APSP where their charge is amplified and stored in a capacitor network (see figure 5.4) which appropriately weights the charge of the three samples. The output of the APSP, the weighted sum, is stored on the sample and hold stage, waiting for read out via the multiplexer [gad92, bin93].

5.1.4 Multiplexer

The output from the APSP is sent to an analog 128 : 1 multiplexer. Due to the internal structure of the multiplexer the channel order seen on the output line does not correspond to the physical channel order. The physical channel number c can be calculated from the output channel number n by

$$c = 32(n \; mod \, 4) + 8 \, int\left(\frac{n}{4}\right) - 31 \, int\left(\frac{n}{16}\right) \tag{5.1}$$

5.1.5 APV Output Format

The output data format of the APV consists of 12 bit digital header and the 128 analog data samples. The digital header consists of three start bits, 8 bits for the events pipeline column address and one error bit. A tick mark is generated every $70th$ system clock cycle (1.75 μs) for synchronization with the data acquisition system. The digital header starts at the position of a tick mark. The output speed is selectable between the system speed (40.08 MHz) or half the system speed (20.04 MHz). The latter gives the possibility to use an external 2 : 1 multiplexer as it is done on the front-end hybrid (see section 5.4). Figure 5.5 shows the data output format of the APV.

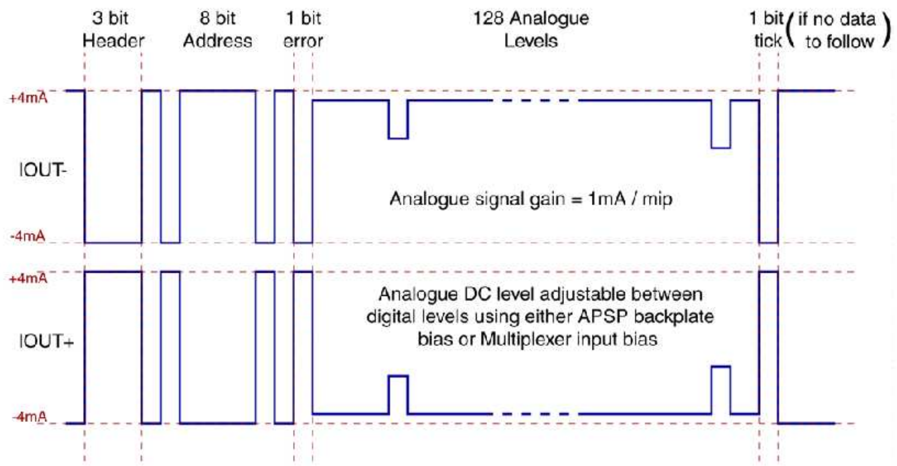

Figure 5.5: *Data format of the APV, both polarities of the differential signal are shown [jon99]*

5.1.6 Calibration Unit

The APV chip contains an internal calibration unit [nev99], designed for on-chip testing and measurement of the APV impulse response. The circuit generates and injects a current pulse of programmable total charge into a selected group of channels. The time between injection and sampling is programmable in steps of 25 ns and 3.125 ns for fine tuning.

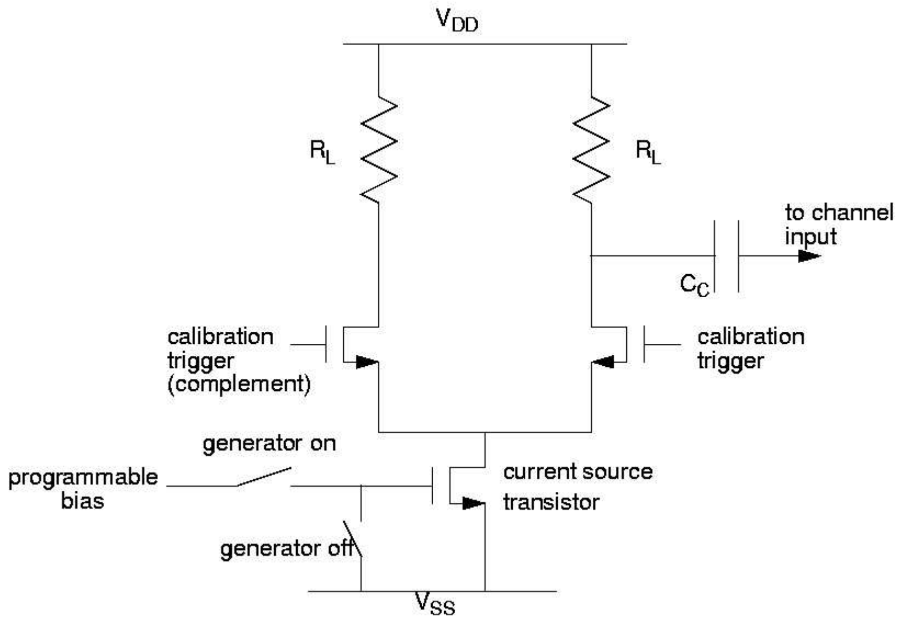

Figure 5.6: *Schematic of the APV internal calibration unit [nev99]*

Figure 5.6 shows the schematics of the APVs calibration unit. The charge injected into the channels is programmable by the voltage applied to the current source transistor (n-type MOS-FET) in steps of 0.01 fC (corresponding to 0.025 of the charge deposition of a MIP in a 320 μm thick silicon detector), covering a range from 0 to 6.4 MIPs [nev99]. The calibration unit for the 128 channels is grouped into 8 selectable sets of 16 channels each. The channel belonging to one set are separated by 7 channels of other sets, minimizing channel to channel interference.

5.1.7 Noise

The designed noise performance of the silicon strip detectors in CMS should be below 2000 electrons. Measurements of equivalent noise charge (ENC) performed for different detector capacities showed for peak mode $(246 + 36/\text{pF})$ electrons and for deconvolution mode $(396 + 59.4/\text{pF})$ electrons [fre01], in good agreement with simulations.

5.2 PLL

In the CMS tracker the system clock and the first level trigger decision are transmitted to the detector via a single line. Therefore, the first level trigger and the system clock are encoded to a single signal, see figure 5.7. The encoded signal is equal to the system clock, except if a trigger is sent one clock cycle stays at logic level “0” [pla00].

This scheme reduces the number of lines needed to transmit the clock and trigger signals to the detectors. The phase lock loop (PLL) chip is designed to decode the system clock and

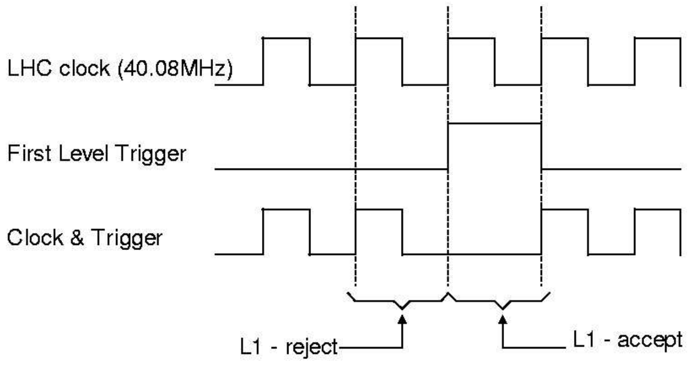

Figure 5.7: *Combined coding of the LHC clock and first level trigger signals [pla00]*

the trigger signal on the detector side. It provides also the possibility to correct the timing of the clock and trigger signals according to the physical position of the detectors in the tracker. An internal clock de-skew mechanism allows to shift the clock phase up to 25 ns in 1.04 ns steps, and a coarse skew compensation for the trigger allows a delay of the trigger signal up to 15 LHC clock cycles (375 ns).

5.3 DCU

The detector control unit (DCU) monitors supply voltages, bias current and temperature sensors placed on the front-end hybrid and the silicon sensors. Seven inputs and one internal thermistor are multiplexed to a 12-bit analog to digital converter (ADC) and read out via an I^2C interface. An internal band-gap voltage reference is used for calibration and a constant current source can be used to drive external thermistors [mag01].

5.4 APVMUX

The APV-MUX chip is placed between the APV and the output lines, multiplexing two APV chips into one single line. This reduces the number of data lines and ADC channels significantly. The output of two APVs are clocked with 20.04 MHz into APVMUX running with the system clock of 40.08 MHz. The output of the APV with odd I^2C address is delayed by 25 ns with respect to the one with even I^2C address [mur00].

5.5 Control Interface

For the communication with the APV chips and the ASICs like PLL, DCU and APVMUX, I^2C bus protocol (I^2C) is used [phi00]. Via the I^2C protocol the registers responsible for the APV settings, like the height of calibration signal or the readout mode, can be accessed and set to new values or read out.

Chapter 6

Detector Module Teststations

6.1 Hardware

The hardware components common for both test-stations developed for detector module qualification and diagnostics are described in this section. Starting with components developed by the CMS collaboration, such as the FED, I^2C card and the Aachen repeater card, followed by the multiple input/output card used for slow control. Finally the motherboard and its special purpose cards, developed by the Karlsruhe readout group are described.

6.1.1 Front End Driver

For the digitization of the data the front end driver (FED) is used. It is a PCI Mezzanine card with eight channels of nine bit ADCs[1], a 1 MByte data buffer, which can be operated at the LHC bunch crossing frequency of 40 MHz.

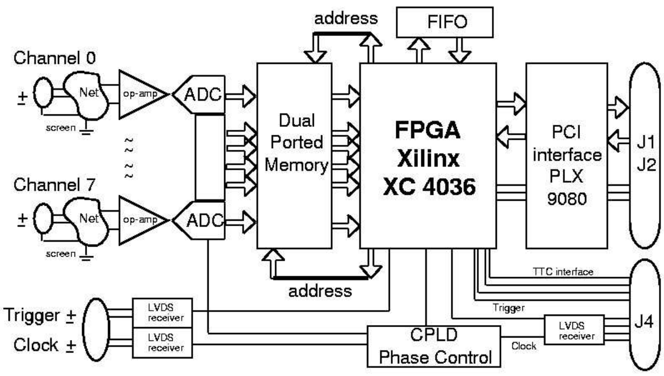

Figure 6.1: *Block diagram of the FED, showing the dual ported memory for storing the data of the 8 ADC outputs, FPGA for data processing and PLX 9080 bridge providing connection to PCI bus* [bai99]

Figure 6.1 shows the schematic layout of the FED. The analog input signal of the APV is converted to digital data and stored as a continuous block inside a dual port memory (DPM), capable to store 256 APV frames. The data is read out in parallel to the ADC via the PCI bus. A complex programmable logic device (CPLD) provides clock and trigger control. The field programmable gate array (FPGA) implemented on the FED supports header finding and a 32-bit deep clock and trigger counter.

[1] The ADC range is 10 bit, but the least significant bit (LSB) is not read out

6.1.2 I^2C Card

As I^2C controller a PCI Mezzanine card (PMC) developed by European Laboratory for Particle Physics (EP) group at CERN is used. This card hosts a PCF8584 chip from Phillips, which always acts as master, providing a maximum clock speed of 90 kHz.

The I^2C protocol is used for the communication with the APV, the ASICs on the front-end hybrid (see chapter 5) and voltage monitors implemented on the repeater card (see section 6.1.3).

6.1.3 Repeater Card

To drive the long lines between front-end hybrid and FED the ARCS repeater card [bei01, axe01] is used. This card consists of two PCB, one providing the power for the front-end hybrid and one hosting buffer chips for the analog data lines, chips to condition the clock and trigger lines and an I^2C level shifter.

The repeater card provides over current and over voltage protection and it is also possible to read out hybrid currents and voltages via an I^2C interface. The separation of high power dissipating part from the repeater part eases the integration into a cooling system. The voltage regulator part can be placed outside the cold box whereas the data buffers has to be placed as close as possible to the front-end hybrid.

6.1.4 Multiple I/O Card (MIO)

As multiple input output card the PCI-6035E from National Instruments [ni 02] is used. It provides eight digital I/O lines, eight timing I/O lines and 16 analog I/O lines with a 16-Bit ADC and a selectable input range of ±10 V, ±5 V, ±0.5 V and ±0.05 V, at a maximum sampling rate of 200 k samples/s.

This card is used to read-out temperature probes, to record the measurements of the leakage current and the bias voltage (see section 6.1.7) via the analog channels, to control the multiplexer of temperature sensors (see section 6.1.8) via its digital lines and to measure the frequency output of the humidity sensor via its timing input.

6.1.5 Motherboard

The motherboard (see figure 6.2) functions as backplane for all hardware components developed by the Karlsruhe CMS read-out group. It consists of an interface card for the connection to a PC and a low voltage regulation card, providing the voltages ±5 V and +3.3 V. It can host up to eight special purpose cards, such as high voltage card, sequencer or led control system. All slots are connected to the power lines of the motherboard and to the parallel data bus, consisting of eight data lines, a reset line, a data strobe and an acknowledge line.

An Altera EPM7064-SLCC-44 programmable logic device (PLD) on the motherboard controls the communication with the PC [alt03]. The control lines for the special purpose cards are active low[2] and the control lines for the PLD are active high[3]. The communication is done in three steps: selecting a slot on the motherboard, sending data and releasing the slot. In the first step the PLD compares the four most significant bits with the board ID, if they are equal the three least significant bits indicate the slot number to be selected. The

[2]logic true level is represented by zero
[3]logic true level is represented by one

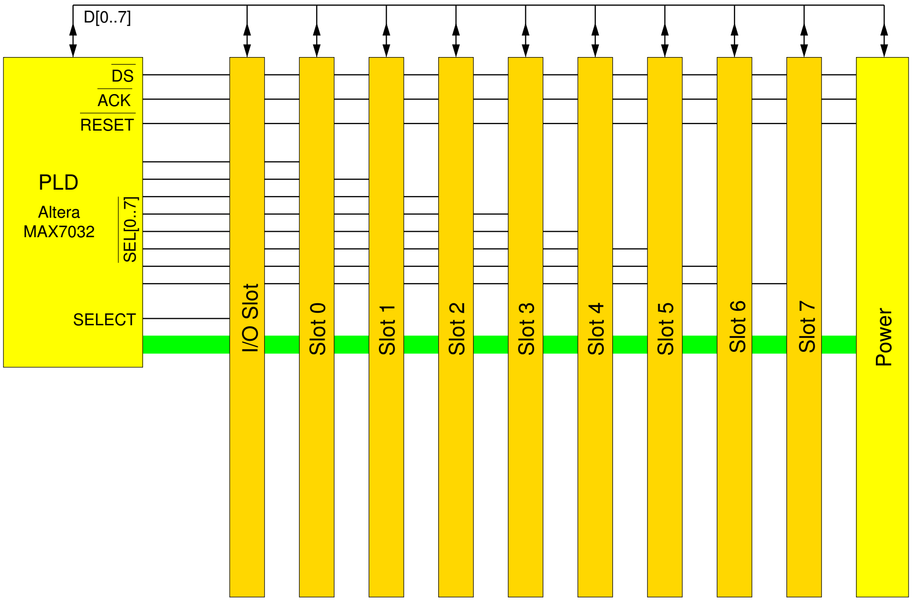

Figure 6.2: *Schematic of the Karlsruhe read-out motherboard* [hei01]

select line of the corresponding slot is set to zero. This slot is active until it is released by the same procedure as for the slot selection. In between data can be sent and received from the card in the selected slot. Every command is confirmed by a hand shake (data strobe, acknowledge) between PC and selected card [hei01].

6.1.6 Sequencer

The sequencer is the key-part of the Karlsruhe read-out system, its an inexpensive replacement for the final control path. It provides all clock and trigger signals needed by the FED and the front-end hybrid. The sequencer also provides the possibility to process external trigger signals coming from cosmic ray or radioactive source setup, as well as to generate a trigger signal for a laser diode or the infrared LED system (see section 6.1.9) [hei01].

6.1.7 High Voltage Card

The high voltage supply for the bias of the detector modules of the two read-out systems uses an ISEG-BPp 10 105 5 module, with maximum ratings of 1000 V and 1 mA. The voltage ripples are smaller than 200 mV_{pp} [ise02].

The voltage output is set via a 8-Bit DAC (AD 557JP), which is controlled by a PLD. The ISEG high voltage module owns a voltage monitor which is read out by the multiple I/O card (see section 6.1.4). For the current monitor an isolation operational amplifier measures the voltage drop over a 4.7 $k\Omega$ resistor in the high voltage line, because the sensors ground is connected to the front-end hybrid and therefore not accessible to high voltage card. The voltage output of the isolation amplifier is compared with a reference voltage set by a second 8-bit DAC. A kill signal is generated by the comparator chip (Max 961) in case of an over current, setting the high voltage to zero.

The isolation amplifier on this card needs a supply voltage of +15 V which is provided by a separate PCB using the +5 V from the motherboard and transforming it by a DC-DC converter and voltage regulator to +15 V.

6.1.8 Slow Control Mux

In the test-stations a large number of temperature probes has to be read out. For this a slow control mux was developed, which multiplexes 32 input channels to one output channel connected to the analog I/O card (MIO). For calibration purpose a reference voltage is applied to one input channel of the slow control mux.

6.1.9 LED System

The CMS tracker consists entirely of silicon detectors, giving a huge test load to participating institutes to ensure a high performance tracker. Therefore a test system was developed capable of qualifying detector modules in a secure and fast way. To test the detector modules a physical signal is generated in the detector by illumination with infrared light. Light from lasers or light emitting diodes (LEDs) of an appropriate wavelength is more comfortable to handle as radioactive sources or cosmic rays and allows shorter testing times. In order to ensure a penetration depth of more than 45 μm to reach the bulk material of a sensor and being independent of surface effects, light with a wavelength greater than 850 nm is needed(see figure 4.4).

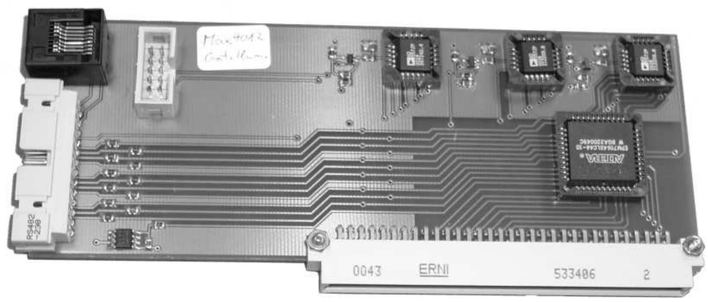

Figure 6.3: *LED array control card, showing three DACs for setting the voltage for the pulse height and constant illumination independly for two groups of arrays. The PLD control the communication between motherboard and LED array*

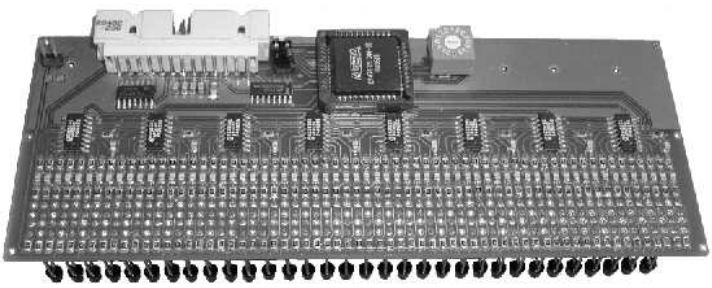

Figure 6.4: *LED array, with 64 infrared LEDs connected to eight 8 : 1 multiplexer chips, the PLD selects a single LED and enables the feed through of the trigger line, which is converted from LVDS to TTL on board*

The LED system consists of two printed circuit boards (PCBs). The LED array card (see figure 6.4) hosting 64 LEDs, a driver circuit, a PLD for selecting a single light emitting diode (LED) and enabling the feed through of the trigger line. The second board, the LED control card (see figure 6.3), is responsible for the communication with the PC and hosts three 8-bit DACs to adjust the applied voltage pulse to the LEDs and a constant bias to the LEDs. For details about the communication and the connection possibilities to a PC see [wei03, wei02].

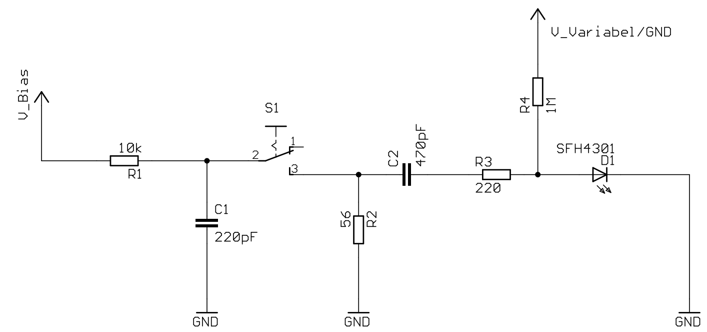

Figure 6.5: *Schematic of the LED driver circuit, eight of these drivers are connected to one multiplexer chip. One complete LED array hosts eight multiplexer chips and 64 LEDs in total. The voltage pulse applied to LED is defined by the resistors* R_2 *and* R_3

Figure 6.5 shows the LED driver circuit, eight of these driver circuits are connected to one multiplexer chip and eight multiplexer chips placed on the LED driver card. The selection of a LED and the connection of the trigger signal to the corresponding multiplexer chip is done by a PLD.

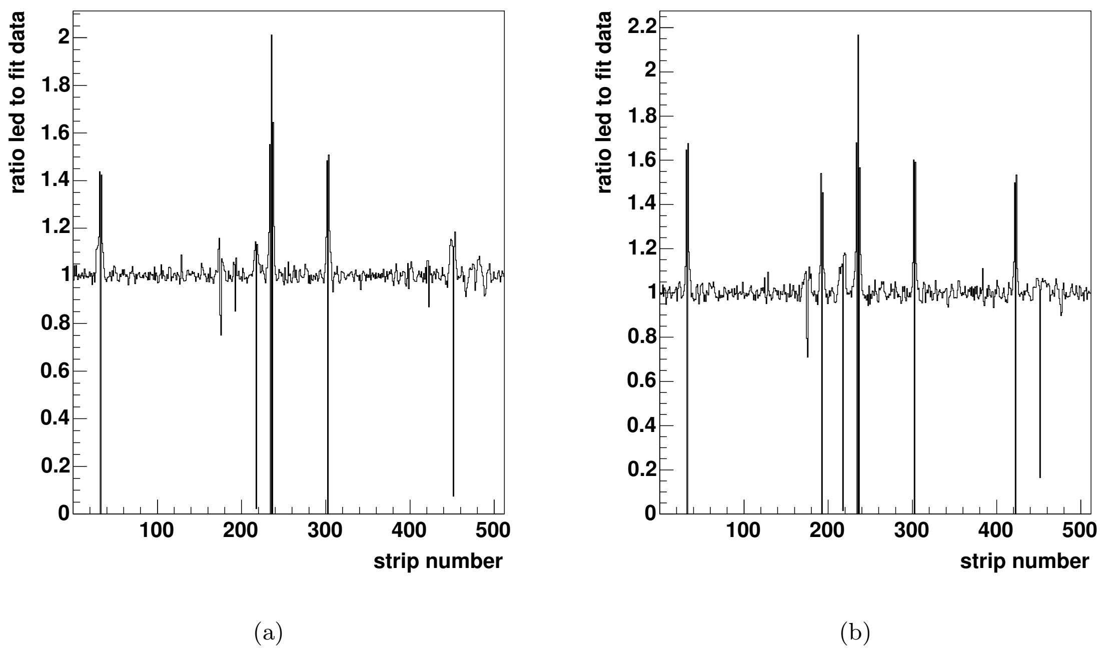

Figure 6.6: *Failure tagging with the LED system done on a TEC ring 6 module in the fast-test station. This graph shows the raw led data divided by a polynomial fit to the LED signals (see appendix D). A deviation from one indicates a strip fault. In (a) the array placed above sensor W6B (sensor next to the hybrid) and in (b) the array placed above sensor W6A (sensor at the far end of the module), tagging with two arrays allows to identify missing bond connections between sensors, here strip number 193 and 423*

The LED system is capable to detect failures like pinholes (ohmic contact between implant and aluminum strip) and unbonded strips. The usage of one or more LED arrays on each sensor allows to predict the position of the missing bond, whether missing between sensor and pitch-adapter or between the two sensors. Figure 6.6 shows the processed LED data, in these plots the raw LED signals are divided by a polynomial fit to the LED signals [fah04] (see appendix D).

Another feature of the LED system is to increase the detectors leakage current artificially by a constant illumination with infrared light. Figure 6.7 shows the behavior of the calibration amplitude of pinholes with increasing leakage current. Genuine good strips show the same response to calibration pulses independently from the leakage current. Strips with pinholes instead can easily be identified by the changing response. In fact the voltage drop over the poly-resistor (1.8 MΩ) and the bias resistors (22 kΩ and 2.2 kΩ) at a leakage current of 30 μA is equal to the virtual ground of the APV input (0.7 V), see figure 6.7a. On the final version of the front-end hybrid the value of the bias resistor changed to 1 kΩ and 2 kΩ respectively. This shifts the leakage current, at which the voltage drop over the resistors equals the APVs virtual ground, to 180 μA (see figure 6.7b). This behavior can be explained by considering the APV input stage as an operational amplifier with feedback loop, which attempts to make the voltage difference between the two inputs to zero [hor89]. In the case of the APV one input is connected to the aluminum strip of the silicon sensor and the other to the virtual ground. This implies the that the aluminum strips are kept by the APV on the same potential as the virtual ground. A Pinhole short circuits the aluminum strip to the p-implant, driving the amplifier into saturation. Only if the voltage drop over the bias resistors and poly resistor reaches the is of the same order as the virtual ground (0.7 V) the amplifier will operates normally.

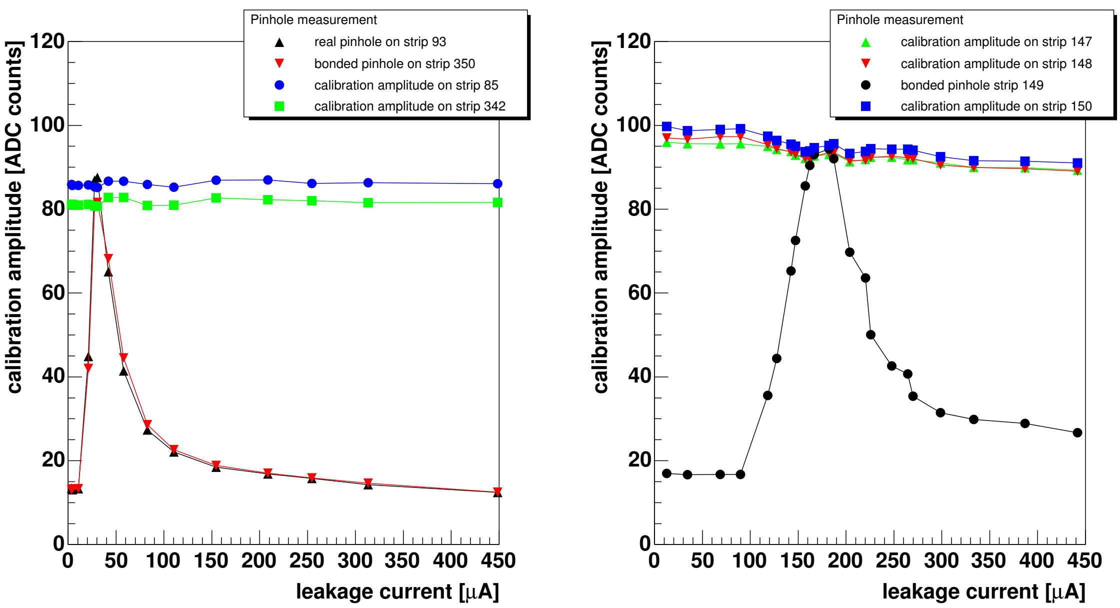

(a) (b)

Figure 6.7: *Pinhole identification using the LED system (a) TEC ring 6 module with bonded and real pinhole with old front-end hybrid version, (b) TOB module with new front-end hybrid version and one bonded pinhole*

6.2 Karlsruhe Readout Software

An object oriented approach was chosen for the readout software. The modular design is well suited for the hardware described in the previous sections and gives maximum flexibility for the integration of further hardware. Figure 6.8 shows the basic design of the Karlsruhe readout software. The hardware is accessed via device drivers, the basics functionalities are placed in shared libraries and the readout tasks and environmental control are combined in a multi-threaded program [dir03].

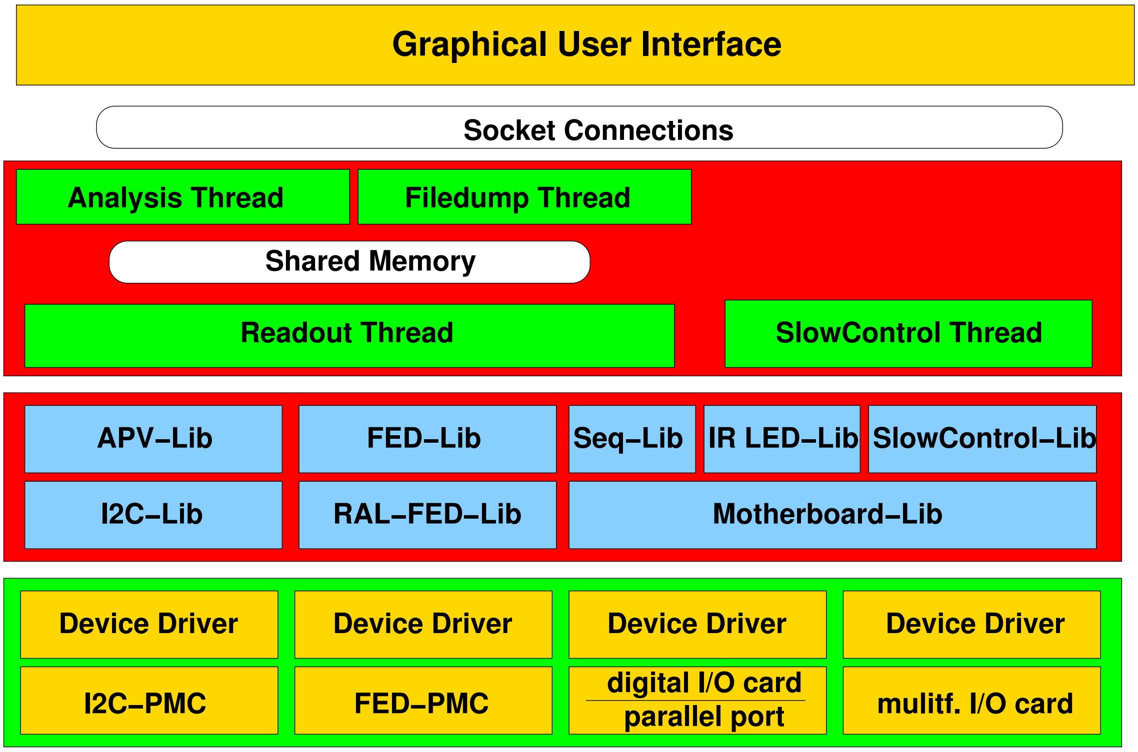

Figure 6.8: *Basic design of the Karlsruhe read-out software. Linux is used as operating system, device drivers for I^2C are developed or adapted (FED,MIO,DIO) and the basic functionalities are placed in shared libraries. All task necessary to read-out a module and control the environment are integrated in a multi-threaded program. The graphical user interface is realized in LabView, which communicates with the different threads by TCP/IP sockets* [dir03]

6.2.1 Graphical User Interface

The graphical user interface (GUI) combines the data visualization and process control. The user can control environmental parameters such as temperature and humidity, apply bias voltage to detector or start readout runs. The data received from the detector are analyzed by a dedicated analysis thread and displayed online. Process control ensures that all processes are executed as defined by the users and displays exceptions and errors [fah04]. Figure 6.9 displays the main window of the GUI.

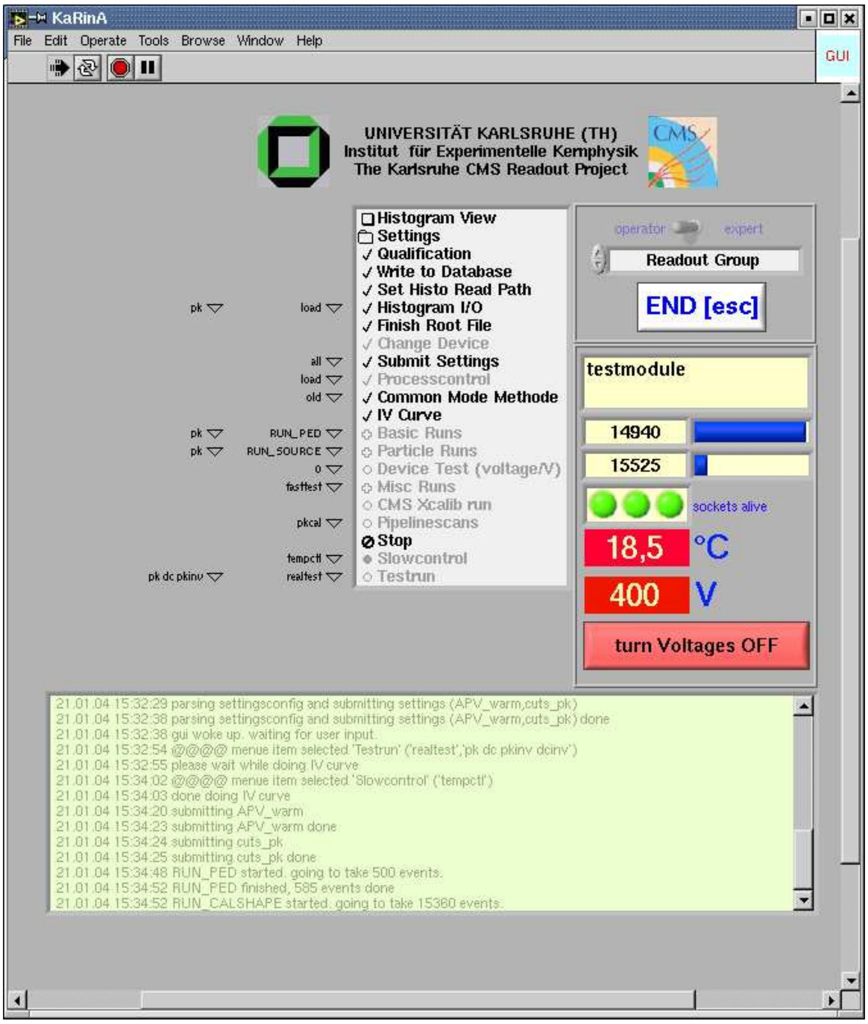

Figure 6.9: *Main window of the GUI. Out of this window all functionalities of the Karlsruhe read-out can be accessed. Processes executed by the GUI or the status of data runs are displayed in the log monitor. Some important parameters, such as high voltage and temperature, are displayed in this window*

6.3 Fast Test Station

The fast-test station (see figure 6.10) is designed to test the functionality and quality of CMS silicon micro-strip modules, following the CMS testing procedure specifications [dir02]. The station is able to thermo-cycle detector modules, testing the detector under mechanical stress as expected in the experiment during cool down and warm up phases.

The main part of the fast-test station is a huge insulated box, which can host one CMS detector module mounted on a transport plate. The insulation material is stacked in different layers of total thickness of 10 cm, limiting the heat flow through the insulation to 2 W, which is approximately the heat dissipated by the front-end hybrid. Four copper cooling towers built the structure of the lower half the box. Each tower has a two stage peltier cooling, connected to the in-house water cooling system. The upper half of the box hosts four LED arrays arranged to illuminate the sensors of a CMS ring 6 module (consisting of two sensors) on each end.

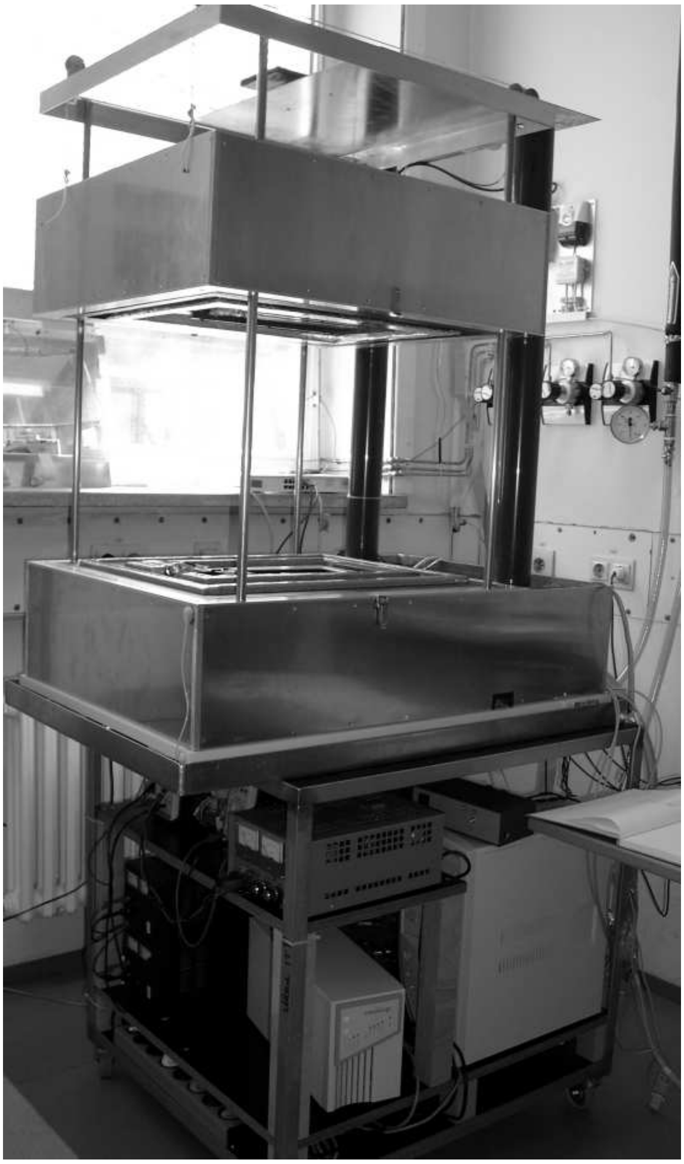

Figure 6.10: *View on the fast-test station. The cover can be lifted on rails, to access inside of the box. The picture of the box gives an impression of the dimension of the thermal insulation. On top of the test station (partly visible) and below a set of scintillators is installed to calibrate the test station and the detector modules with cosmic ray particles. The readout electronics is placed behind the test station and the power supplies, the power pack and PC below [dir03]*

6.3.1 Power Pack

The power for readout components and the peltier cooling system is controlled by the power pack (see figure 6.11). The power pack hosts four batteries (6 V / 12 Ah), two battery chargers and serves connections for several external power supplies. Each battery can be connected independently to a special load, e.g. the positive or negative motherboard supply voltage. Two external power supplies (3...30 V / 20 A) are foreseen for the supply of the peltier cooling and another power supply ensures the functionality of the readout components at the power up, regardless of the charge state of the batteries.

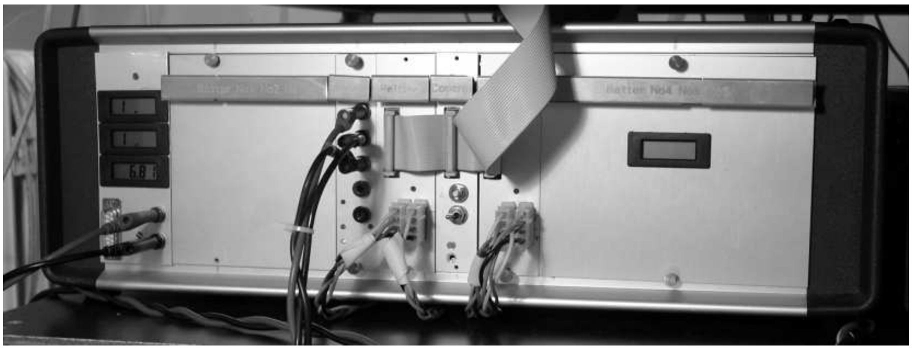

Figure 6.11: *View on the power pack. The power pack controls the power supply of the fast-test station and the peltier element*

6.3.2 Peltier Control

The peltier control is a simple switching matrix, integrated in the same crate as the power pack (see figure 6.11). It applies power to peltier elements and inverts the polarity of the voltage, so that one can cool down or heat up the detector module.

The reference temperature for the peltier control is a temperature probe mounted on the aluminum transport frame of the detector module. When the box is cooled and measured value is below the appointed value by 2°C the peltier elements of the upper cooling layer will be switched off, if the measured value exceeds the appointed value by 1°C the cooling continues. The lower layer cools continously to minimize the time needed to cool down the box again. To avoid damage to the detector module due to thermal runaway, a watchdog was implemented in the control PLD, which switch off the power every 30 sec. after the last command arrived from the PC.

6.3.3 Cosmic Setup

For calibration of detector modules with cosmic ray particles a set of plastic scintillators with photo multiplier tubes (PMTs) are used. One scintillator is mounted on the bottom and the other one on top of the station, the distance between them is around 1.85 m. The scintillators have an active area of 12×22 cm^2, sufficient to cover all types of CMS detector modules. Due to the large distance between both scintillators the particles pass the detector nearly perpendicular and therefore a uniform energy deposition is observed [wal02]. Figure 6.12 shows the schematic of the trigger setup. The large distance of the scintillators restrict the trigger rate to approximately 1 per minute.

6.4 Diagnostic Test Station

The diagnostic test station is designed for the deep investigation of silicon detector modules, especially with radiation sources, such as ^{90}Sr, infrared laser light or by the use of micromanipulation probes. To provide enough space inside the box for dedicated test setups, the outer dimensions of the shielding are kept voluminous.

The main component of the diagnostic-station is the linear gate system (see figure 6.14), which can be equipped with a laser optic, radioactive source or a microscope. The linear gate

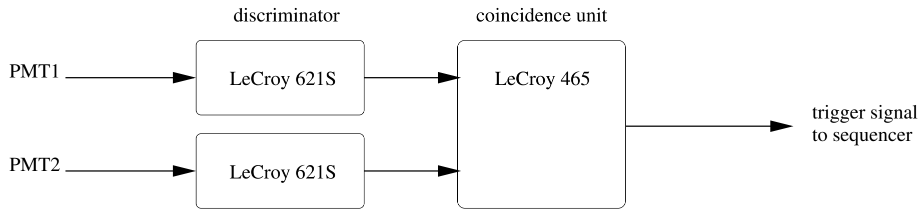

Figure 6.12: *Schematic of the cosmic trigger setup, the PMT signals are converted to TTL in a discriminator and the trigger signal is generated by the coincidence unit*

Figure 6.13: *View on the diagnostic-station. The large front door gives the operator enough space to position micromanipulation probes, adjust the laser optics or inspect the whole detector module with the microscope. Above (as seen in top of the picture) and below the box scintillators with PMT are installed for detector calibration with cosmic ray particles. For source measurements another pair of PMTs placed below the detector module* [dir03]

system can scan an area of 28×45 cm^2, with an accuracy of 6 μm in x-direction (perpendicular to the readout strips) and 150 μm in y-direction (parallel to the readout strips) [sch02]. The linear gate system is mounted on an aluminum plate, which is placed on 10 cm thick granite plate to decouple mechanical vibrations from the detector module under investigation. This is important to avoid scratches on the detector module when micromanipulation probes are attached.

The read-out electronics is based on the components described in the previous sections. The sequencer for the generation of clock and trigger, the repeater to drive the signals between APV and PC, the FED for the digitization of the data, the control card for the LED system. However, the LED array is equipped with an additional matrix of 4×4 LEDs of 1050 nm wavelength to increase the leakage current artifically by constant illumination. This 4×4 matrix allows a more homogenous increase of the leakage current over the whole detector area. Moreover, the current is generated across the whole bulk material due to the larger penetration depth of the photons (see figure 4.4).

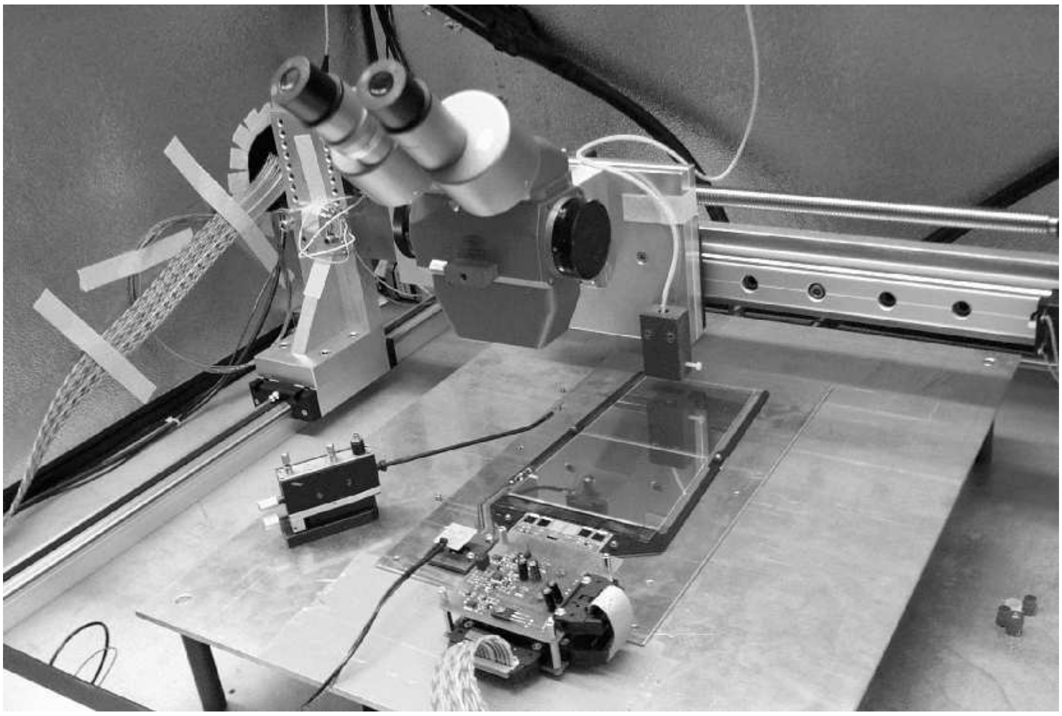

Figure 6.14: *View inside the diagnostic-station. A microscope is mounted on the linear gate system, for visual inspection or the positioning of micromanipulation probes, as they are used for strip measurements or the connection of the bias ring, to test unbonded sensors. Beside the microscope the laser optics is attached for strips scans and efficency measurements. PMT with plastic scintillators are placed below the detector module and a radioactive source can be mounted to the linear gate system* [dir03]

6.4.1 Laser Setup

In the diagnostic-stations a 1060 nm laser with a 1 ns rise and fall time is used. Figure 6.15 shows the trigger scheme for the laser setup. The sequencer card triggers a pulse generator, which supplies the laser with an in height and width adjustable pulse. The intensity of the laser is proportional to the pulse height of the pulse generator's output signal and the pulse width defines the duration of the laser pulse.

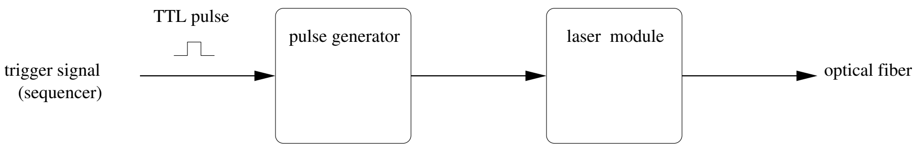

Figure 6.15: *Schematic of the laser trigger setup. The trigger signal from the sequencer card triggers a pulse generator, which is connected to the laser. The height and width of pulser signal defines the intensity and duration of the laser. The laser light is guided to to detector via an optical fiber and focused by a lens*

6.4.2 Source Setup

For signal to noise measurements a radioactive source can be installed to the linear gate system. The source is placed about 5 cm above the detector. Two PMTs with plastic scintillators placed below the detector generate the trigger signal as shown in figure 6.16.

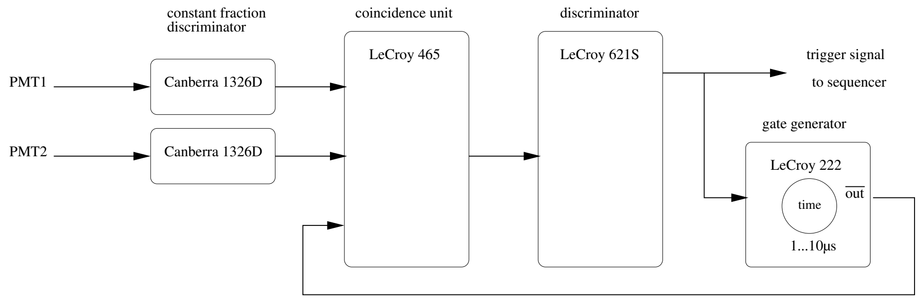

Figure 6.16: *Schematic of the source trigger setup. The PMT signals are fed into constant fraction discriminators, then the coincidence of the signals is checked and the trigger signal (TTL) is generated in a discriminator. With a gate generator the trigger rate can be reduced, due to a in width adjustable veto signal fed into the coincidence unit*

6.4.3 Dry Air Cooling

Irradiated modules have to be operated at low temperatures, due to increased leakage current caused by radiation damage. To achieve a reliable cooling with minimal effort, the modules are cooled by a laminar air flow. Dry air is blown through a pipe which transverses a volume of liquid nitrogen. This pipe is connected to a box in which the module to be tested is installed. Holes in the top and bottom cover of this box allow measurements with radioactive source and usage of micromanipulation probes for measurements on sensor basis. The temperature can be controlled by the flow of the cooled air and additionally by mixing the cooled air with air of room temperature, this is done by valves.

Chapter 7

Irradiation Studies

7.1 Radiation Damage on Semiconductor Devices

In this section the basic damage mechanism of radiation in semiconductors and their macroscopic effects on the properties of silicon detectors are summarized.

7.1.1 Formation of Lattice Defects

Radiation interacts with the electron cloud of semiconductors, creating electron hole pairs (see section 4.1.5.2 and 4.1.5.3), this fact is exploited for particle detection. However, radiation can also interact with the nuclei in the semiconductors lattice. The first process is reversible, the latter may lead to permanent changes in the material, namely in displacements of lattice atoms, creating interstitials (atoms between regular lattice sites) and vacancies (empty lattice sites), or nuclear interaction like neutron capture by a lattice atom.

The minimum energy needed to displace a silicon atom from its lattice site is $E_{\mathrm{min}} = 15$ eV. However the threshold for the displacement depends on the direction of the recoil. A much higher energy is needed if the recoil direction points to neighboring a atom. Therefore the displacement energy E_d is defined as the energy when the probability function for displacement is one half. In silicon the displacement energy is $E_d = 25$ eV. Below this value the transferred recoil energy is dissipated by phonons, above this value in addition to the phonons a silicon atom can be displaced from its lattice site, creating an interstitial and vacancy pair.

Radiation	Electron	Proton	Neutron	Si^+
Scattering	Coulomb	Coulomb and Nuclear	Nuclear	Coulomb
T_{max}[eV]	155	133700	133900	1000000
T_{av} [eV]	46	210	50000	265
E_{min} [eV] point defects	26000	190	190	25
E_{min} [eV] defect cluster	4600000	15000	15000	2000

Table 7.1: Characteristics of radiative interaction with silicon. Represented are the main scattering processes, the maximum possible kinetic energy transfer by recoil (T_{max}), the mean recoil energy (T_{av}) for incident particle of 1 MeV and the minimum energy (E_{min}) needed for creation of a point defect and a defect cluster [lut99]

Depending on the energy transferred to the primary knock-on atom (PKA) by the scattering process, the displaced lattice atom can create further interstitials and vacancies pairs, these defects can be either single point defects or accumulate to clusters (see table 7.1). For example at an energy below 1 keV to 2 keV only isolated point defects are created. At energies between 2 keV and 12 keV the energy is high enough to create a defect cluster and several point defects and above 12 keV several clusters and point defects will be produced [lut99].

7.1.2 NIEL Scaling

As mentioned in the previous section the primary interaction depends on type and the energy of the radiation. A tool to compare the radiation induced damage in the semiconductor for different particles is the non ionizing energy loss (NIEL) hypothesis. The assumption for the NIEL scaling is, that the induced damage in the semiconductor scales linearly with the energy lost in displacing collisions. This could be described by the displacement damage function

$$D(E) = \sum_i \sigma_i(E) \int_0^{E_r^{max}} f_i(E, E_r) P(E_r) dE_r \ , \tag{7.1}$$

where it is summed over all possible interactions, σ_i is the cross section of the ith interaction, $f_i(E, E_r)$ the probability for a collision of a particle with energy E transferring the recoil energy E_r and $P(E_r)$ the Lindhard partition function [mol99].

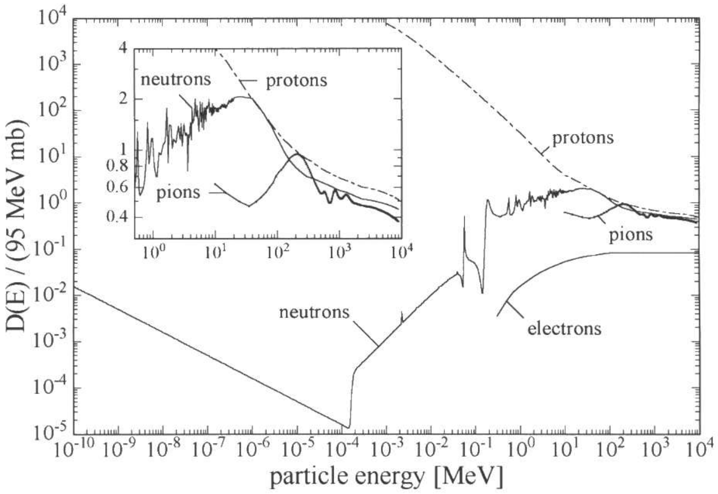

Figure 7.1: *Displacement damage function $D(E)$ normalized to 95 $MeV mb$, for neutrons, protons, pions and electrons. The inserted graph shows a detail of the figure around relevant energies for high energy physics* [mol99]

For the investigation of radiation damage it is common practice to scale fluence ϕ of the used radiation to the equivalent fluence ϕ_{eq} needed to obtain the same damage with 1 MeV neutrons. This can be achieved using the *hardening factor*, which gives the connection between the particle fluence and the equivalent fluence of 1 MeV by

$$\kappa = \frac{\int D(E)\phi(E)dE}{D(E_{\text{neutron=1 MeV}}) \int \phi(E)dE} = \frac{\phi_{eq}}{\phi} \ , \tag{7.2}$$

here $D(E)$ is the displacement damage function and $\phi(E)$ the energy spectra of the incident particle beam. Figure 7.1 shows the displacement damage function normalized to 95 MeV mb for different particles and particle energies.

7.1.3 Stable Defects

The interstitials and vacancies created by displacement damage are mobile at room temperature. They can move through the lattice and recombine by interstitials filling vacancies or diffuses out of the surface. This process is called beneficial *annealing*. Another possibility for the reduction of the number of defects is that they got trapped by impurity atoms, other defects or defect complexes, which are already present in the crystal lattice or generated by radiation damage. These defects are point like defect complexes and stable at room temperature.

Defect	Charge states	Energy levels
interstitial	I^-	$E_c - 0.39$
	I^0	
	I^+	$E_v + 0.4$
vacancies	V^{--}	$E_c - 0.09$
	V^-	$E_c - 0.4$
	V^0	
	V^+	$E_v + 0.05$
	V^{++}	$E_v + 0.13$
divacancy	V_2^{--}	$E_c - 0.23$
	V_2^-	$E_c - 0.39$
	V_2^0	$E_v + 0.21$
	V_2^+	
A-center	$(V-O)^-$	$E_c - 0.18$
	$(V-O)^0$	
E-center	$(V-P)^-$	$E_c - 0.44$
	$(V-P)^0$	
Dopants		
phosphorous	P^0	$E_c - 0.045$
	P^+	
boron	B^-	$E_v + 0.045$
	B^0	

Table 7.2: *Charge states and energy levels for important defects and dopants in silicon. I interstitial, V vacancies, O oxygen, P phosphorous and B boron* [lut99]

In n-type silicon the most common defect complexes are A-centers, divacancies and E-centers. An A-center is a vacancy oxygen pair (V-O), where the oxygen is still present from the crystal growth, a divacancy (V-V) is a defect complex of two vacancies on neighboring lattice sites and the E-center is defect complex formed by vacancy and a phosphorous doping atom (V-P).

The electrical properties of defect complexes are more complicated than those of normal flat donors and acceptors used for doping the silicon material (see table 7.2). They can act as generation and recombination centers, capturing and emitting electrons and holes, leading to an increase in leakage current. The charge density in the space charge region is increased, altering the voltage where the detector is fully depleted and therefore the sensitivity of particle detection might be effected. Defects can also appear as trapping centers, capture and remit electrons or holes with some delay, decreasing the detected signal, because the trapped charge is released too late for the current read-out cycle.

7.1.4 Annealing

As mentioned before the radiation induced interstitials and vacancies are not stable at room temperature and can move through the detector. Some defects will dissappear due to filling up vacancies by interstitials, diffusing out through the surface or dissociation of defect complexes, this is called beneficial *annealing*. The annealing is a temperature and time depend process and could be described by

$$N_D(t) = N_D(0)e^{-\frac{t}{\tau}} , \tag{7.3}$$

where N_D is the defect concentration and $\frac{1}{\tau}$ the rate constant, described by the relation $\tau(T) \propto e^{\frac{E_A}{k_B T}}$. The reaction rate depends on the activation energy E_A, needed to dissociate defect complexes and the temperature [lut99].

As new defect complexes are formed and formerly electrically inactive defects are transformed into active defects, the annealing process is not always beneficial for the detector performance.

7.1.5 Effects of Radiation Damage on Detector Parameters

Radiation induced defects in the crystal lattice changes the detector properties. In this section the influence of the radiation damage and the annealing process on the leakage current, depletion voltage and charge collection efficiency is discussed.

7.1.5.1 Leakage Current

The radiation induced defects can change their charge state due to the capture and emission of electrons and holes. The emission probability is exponential and depends on the energetic level of the defects in the band gap, the closer the defect levels are to the band gap center the more effective they contribute to leakage current.

The increase of the volume generated leakage current is described by the parameter α

$$\frac{\Delta I}{V} = \alpha\phi_{eq} , \tag{7.4}$$

where ϕ_{eq} is the equivalent fluence of 1 MeV neutrons, α the *current related damage rate.* This parameterization holds for a wide range of fluence from 10^{10} to $10^{15} n_{1MeV}$ cm^{-2}.

The current related damage was found to continuously decrease with increasing annealing time (see figure 7.2b), described by [mol02]

$$\alpha(t) = \alpha_0 e^{-\frac{t}{\tau_I}} + \alpha_1 - \alpha_2 \ln\frac{t}{t_0} , \tag{7.5}$$

where $\alpha_0 \approx 1.23 \times 10^{-17}$ Acm^{-1}, $t_0 = 1$ minute, $\alpha_2 \approx 3.07 \times 10^{-18}$ Acm^{-1}. The parameters $\frac{1}{\tau_I}$ and α_1 are temperature dependent and may be calculated by the Arrhenius relation

$$\frac{1}{\tau_I} = k_{0I} e^{-\frac{E_I}{k_B T_a}} , \tag{7.6}$$

with $k_{0I} \approx 1.2 \times 10^{13}$ s^{-1}, $E_I = 1.11$ eV and

$$\alpha_1(T_a) = \alpha_{10} + \alpha_{11}\left(\frac{1}{T_a}\right) , \tag{7.7}$$

with $\alpha_{10} \approx -8.9^{-17}$ Acm^{-1}, T_a the annealing temperature and $\alpha_{11} \approx 4.6^{-14}$ Acm^{-1} [mol02].

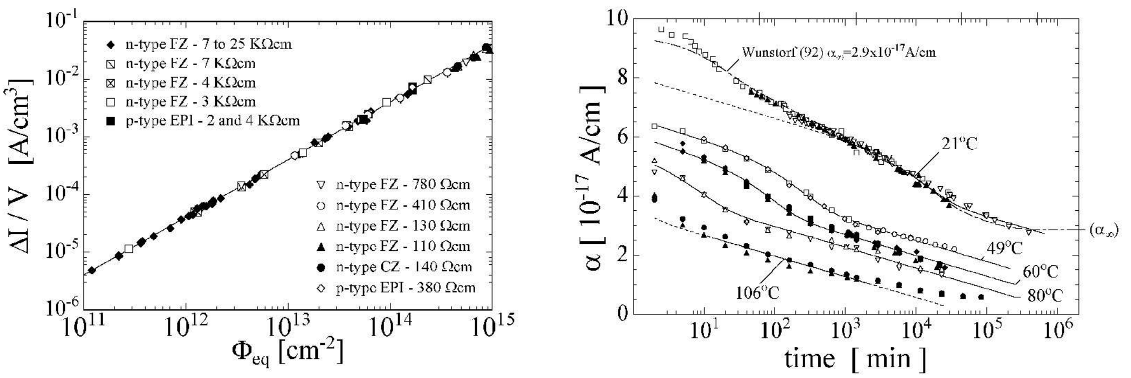

(a) (b)

Figure 7.2: *(a) Fluence dependence of the leakage current for silicon detectors for several material. (b) Current related damage rate α as function of annealing time at different temperatures* [mol99]

7.1.5.2 Depletion Voltage

The effective doping concentration changes due to radiation induced damage. The original dopants may be captured by defects or impurities, forming defect complexes which have different charge states as the dopant itself. This is called *donor removal* in a n-type semiconductor. Additional to these defects others like divacancies can be induced (see table 7.2). This change in the effective doping concentration reflects in the depletion voltage (see equation 4.24).

In contrast to the current related damage rate the *annealing* behavior of the effective doping concentration is not always beneficial, there is also a contribution called *reverse annealing*. As long as the *beneficial annealing* dominates the defect concentration decreases. When the reverse annealing dominates the defect concentration increases. The *Hamburg Model* [mol99] proposes a parameterization of the change in the effective concentration in the space charge region by

$$\Delta N_{eff}(\phi_{eq}, t) = N_A(\phi_{eq}, t) + N_C(\phi_{eq}) + N_Y(\phi_{eq}, t) . \tag{7.8}$$

Where N_A describes the short term annealing behavior, N_C the stable damage and N_Y the long term annealing.

Immediately after irradiation a change in the depletion voltage is observed. Before type inversion the depletion voltage increases with time. After type inversion the depletion voltage decreases. Both cases can be interpreted by an increase in the effective charge carrier concentration N_{eff}. For the not type inverted detector N_{eff} is positive and becoming more positive. For the type inverted detector N_{eff} is negative and becoming less negative. This behavior is called *short term annealing* and could be expressed as a sum of exponential terms

$$N_A(\phi_{eq}, t) = \phi_{eq} \sum_i g_{a,i} e^{-\frac{t}{\tau_{a,i}}} \ , \tag{7.9}$$

where the average introduction rate $g_{a,i}$ for the longest decay time, relevant for high energy physics experiments, was measured by [mol99] to be $g_a = (1.81 \pm 0.14) \times 10^{-2}\ \mathrm{cm}^{-1}$.

Over a longer annealing period the depletion voltage for an inverted detector increases, because the space charge region becomes more negative. This is due to the creation of acceptor type defects, described by

$$N_Y(\phi_{eq}, t) = N_{Y,\mathrm{inf}} \left(1 - \frac{1}{1 + k_Y N_{Y,\mathrm{inf}} \cdot t}\right) \ , \tag{7.10}$$

with the reverse annealing amplitude $N_{Y,\mathrm{inf}} = g_Y \cdot \phi_{eq}$, where g_Y is measured to be $(5.16 \pm 0.09) \times 10^{-2}\ \mathrm{cm}^{-1}$. The time constants (see table 7.3) can be calculated using the Arrhenius relation for short term annealing $\frac{1}{\tau_a} = k_{0,a} e^{-\frac{E_{aA}}{k_B T_a}}$ and reverse annealing $\frac{1}{\tau_Y} = k_{0,Y} e^{-\frac{E_Y}{k_B T_a}}$, with the activation energy $E_{aa} \approx 1.09$ eV, $E_Y \approx 1.33$ eV and $k_{aa} \approx 2.4 \times 10^{13}\mathrm{s}^{-1}$, $k_Y \approx 1.5 \times 10^{15}\mathrm{s}^{-1}$.

annealing temperature [°C]	−10	0	10	20	40	60	80
short term annealing τ_a	306 d	53 d	10 d	55 h	4 h	19 min.	2 min.
long term annealing τ_Y	516 y	61 y	8 y	475 d	17 d	21 h	92 min.

Table 7.3: *Temperature dependence of the time constants τ_a for the short term annealing and τ_Y for the reverse annealing* [mol99]

$N_C(\phi_{eq})$ describes the stable component of the radiation induced damage, which is not influenced by temperature and time.

$$N_C(\phi_{eq}) = r_c \cdot N_{eff,0} \left(1 - e^{-c\phi_{eq}}\right) + g_C \cdot \phi_{eq} \ . \tag{7.11}$$

The stable damage consists of two terms. One describing the incomplete donor removal depending on the accumulated fluence, the initial resistivity $N_{eff,0}$ and the incomplete donor removal constant r_c, describing the fraction of initial donors removed [fur04]. The second term describes the increasing number of stable acceptors which is proportional to the fluence. Figure 7.3 shows the calculated dependence of the depletion voltage on the fluence and on the annealing time.

7.1.5.3 Charge Collection Efficiency

The charge created by a particle traversing the detector could be captured by lattice defects and defect complexes, deteriorating the signal to noise ratio (SNR). Defect states with energy levels above the intrinsic Fermi level will trap electrons and those with energy levels below holes. The capture probability per time is given by

$$\frac{1}{\tau_{t,n/p}} = \sigma_{n/p} v_{th,n/p} N_{t,n/p} \ . \tag{7.12}$$

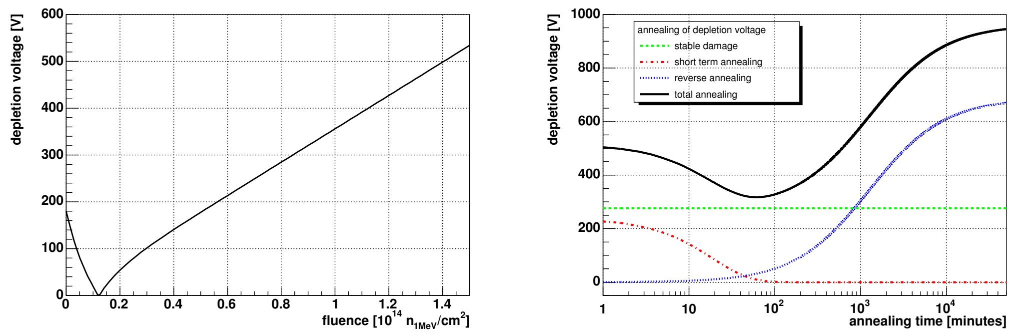

(a) (b)

Figure 7.3: *Behavior of the depletion voltage under irradiation, (a) fluence dependence and (b) annealing behavior of the depletion voltage after irradiation to* 0.7×10^{14} n_{1MeV} cm^{-2} *for annealing at* $60°C$. *These curves are calculated for the values mentioned in the text*

Here $N_{t,n/p}$ is the trap concentration for electron/holes, $\sigma_{n/p}$ the cross section and $v_{th,n/p}$ the thermal velocity. It is assumed that the traps have only one energy level within the bandgap of the silicon and the thermal velocity of the charge carrier is higher than the drift velocity.

7.1.6 Radiation Damage to MOS Structures

In the previous sections the radiation induced damage and its consequences for operation of the detectors bulk material is presented. Further the radiation damage to the surface area, especially effects in the oxide has to be considered. The radiation damage in semiconductor insulator interfaces influences not only the detector itself, but also the read-out electronics, which consists of many metal oxide semiconductor (MOS) devices.

Already without irradiation the crystal lattice order of semiconductor insulator (e.g. Si/SiO_2) interfaces is disturbed over the depth of many lattice spacings, due to the different lattice spacing of the two components. The radiation induced damage to the crystal lattice can almost be neglect in consideration of the highly irregular crystal structure of the interface region. Therefore the charge generated by ionization plays the major role in the radiation induced damage to surfaces and interfaces [lut99, ma 89, cla02].

The large difference in the mobility of electrons and holes in the insulator is of great importance for defect evolution. Electrons can diffuse out of the insulator in the order of 1 ps. Only during this short time recombination of electrons and holes can take place, whereas the holes, which did not recombine, are captured in traps. The trapping takes place within the high defect densities near the interface, charging up the oxide. Due to the limited number of traps the oxide charge saturates at value $N_{ox} \approx 3 \times 10^{12}$ cm^{-2} [wun96], this depends on the oxide quality and the applied voltage.

7.2 The Irradiation Setup at the Karlsruhe Cyclotron

The proton irradiation took place at the compact cyclotron at the Forschungszentrum Karlsruhe, which provides 26 MeV protons with a beam spot diameter of 1 cm and a current of $1 - 2$ μA. The exposure time reflects the expected fluence in the detector after 10 years of LHC. In addition a safety factor of 1.5, due to uncertainties in the expected fluence and a hardness factor of ≈ 1.85 for 26 MeV protons were taken into account. The highest estimated fluence in the inner barrel detector is 1.6×10^{14} n_{1MeV} cm^{-2} and 0.5×10^{14} n_{1MeV} cm^{-2} for the outer barrel detector (see section 3.3.4).

The structures to be irradiated are placed in an insulated box, which can be cooled during irradiation by flushing the box with cooled nitrogen gas. The box is seated on a x-z stage in front of the beam pipe, giving the possibility to scan an area of 400×200 mm^2 (see figure 7.4).

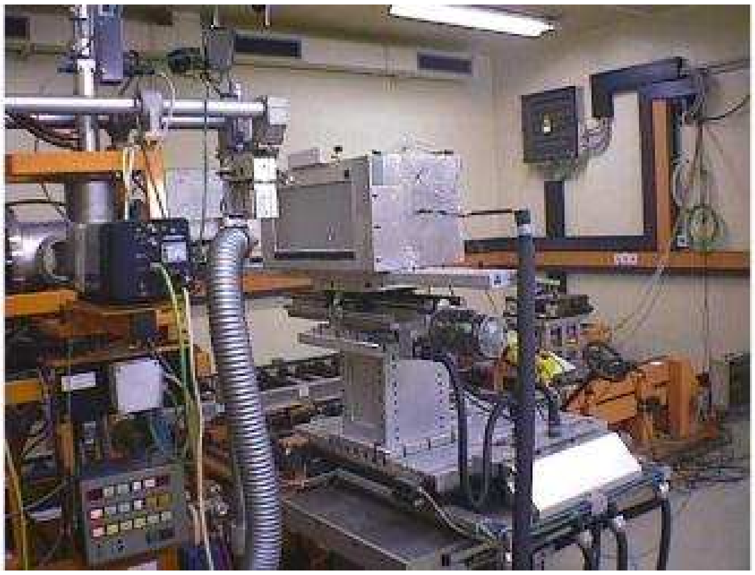

Figure 7.4: *The proton irradiation facility, at the compact cyclotron in the Forschungszentrum Karlsruhe, the beam line is coming from the left, the insulated box, in which structures to be irradiated are stored, is placed on a x-z stage in front of the beam line. A total area of* 400×200 *mm*^{2} *can be accessed*

7.3 The Neutron Irradiation Setup at Louvain-la-Neuve

The neutron irradiation was performed at the Louvain-la-Neuve isochronous cyclotron. To reach the fluence of 0.5×10^{14} n_{1MeV} cm^{-2} (outer barrel) to 1.6×10^{14} n_{1MeV} cm^{-2}, (inner barrel) expected at the LHC in a reasonable time scale, the neutron beam is created by steering a high intensity 50 MeV deuteron beam on a beryllium target, using the reaction $^9Be + d \rightarrow n + ^{10}Be$. To harden the neutron beam energy spectrum and reduce contamination a shielding of 1 cm polystyrene, 1 mm cadmium and 1 mm lead is placed after the stainless steal window of the target box [as+03]. Figure 7.5 shows the beam profile at 55 cm and 77 cm from the target.

7.4 Hybrid Irradiation

The irradiation level expected at the CMS experiment is a challenge for all components of the detector. Especially the central tracker located around the interaction point is exposed

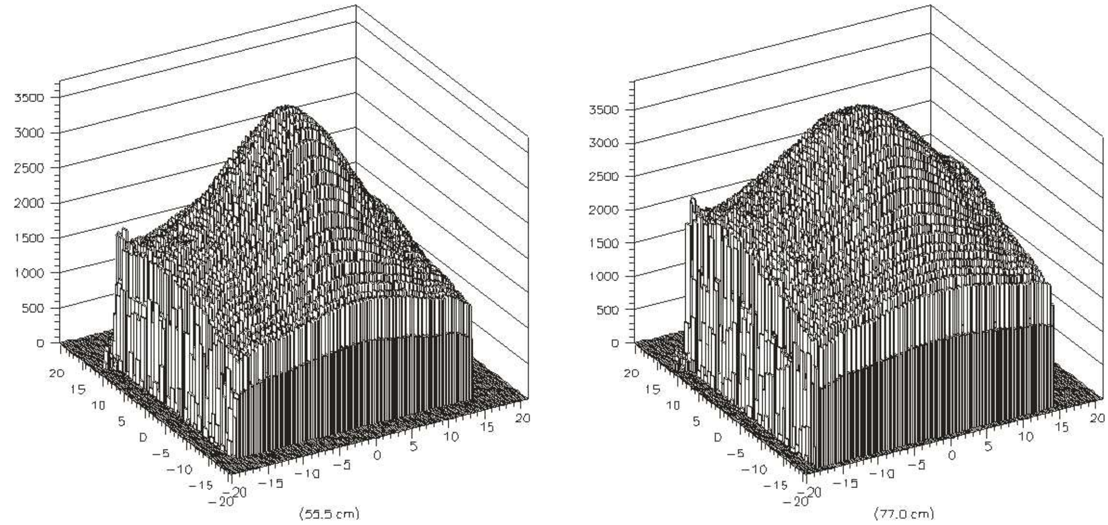

Figure 7.5: *Beam profile for the neutron beam at a distance of (a)* 55 *cm and (b)* 77 *cm from the target [ber01]*

to a high fluence, which has to be considered in the design and also in the testing procedures of these components.

The APV chip is manufactured in the 0.25 μm deep submicron process which is expected to be intrinsically radiation hard. The same process is used for the ASICs like DCU or PLL, placed on the front-end hybrid (see chapter 5). To ensure the operation of the front-end hybrid over the full LHC operation time of ten years with respect to the accumulated fluence (see figure 3.7) a qualification of the radiation hardness of the front-end hybrid has been performed. To be as close as possible to real operation conditions the front-end hybrid was powered, initialized with the standard settings (see [jon01]), supplied with clock signal and triggered for readout with a trigger rate of 50 kHz during the proton irradiation.

The front-end hybrid was qualified before and after the irradiation, both at room temperature and at the nominal operation condition of $-10°$C. The qualification procedure requests an optical inspection to detect mishandling e.g touched wire bonds or discoloration or lost adhesive joints due to irradiation. In the next step the front-end hybrid is tested electrically by connecting it to the test-station (see chapter 6), checking the I^2C communication, measuring pedestal, noise and testing calibration data and the functioning of all pipeline cells. The readout of noise, pedestals and calibration signals was performed in all modes (peak and deconvolution), with and without inverter stage and calibration unit on. This procedure allows to determine the source of possible failures.

Figure 7.6 shows the noise of the APV chips before and after irradiation for peak mode with inverter stage on and calibration unit on (figure 7.6a) and for deconvolution mode with inverter stage on and calibration unit on (figure 7.6b). There was no increase in noise and no additional channel show up to be noisy after irradiation. The only suspicious channels belong to chip boarders which are known to be sensitive to the grounding scheme of the station.

In contrast to the noise, an increase in the pedestals and the amplitude of the calibration signals was observed after irradiation. The same behavior had been found on a previous

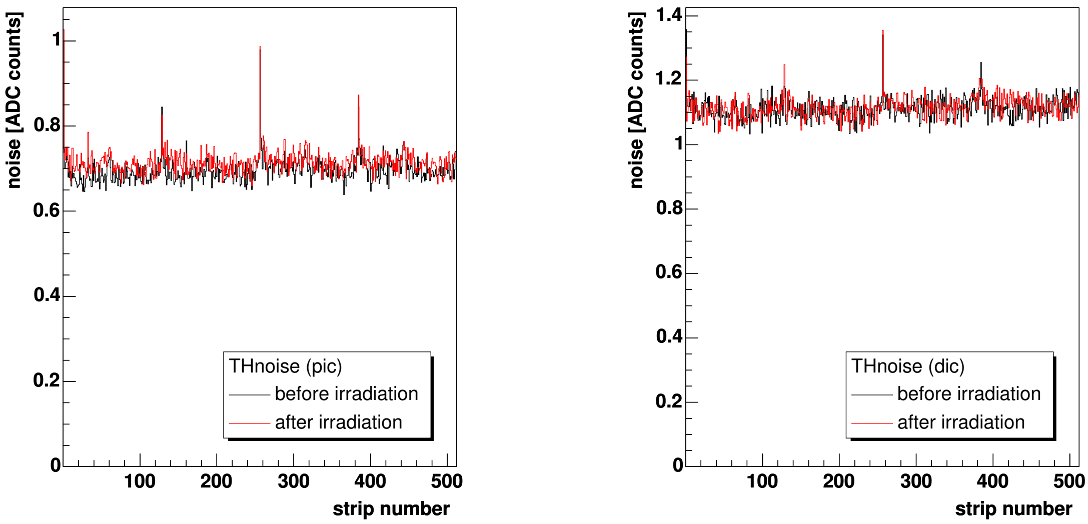

(a) (b)

Figure 7.6: *Common mode corrected noise for peak mode inverter on (a) and deconvolution mode inverter on (b) before and after irradiation*

version of the front-end readout hybrid. Figure 7.7 shows the pedestals for peak and deconvolution mode. The increase of the pedestals in peak mode is ≈ 70 ADC counts and ≈ 60 in deconvolution mode. A similar behavior shows figure 7.8 for the calibration amplitude and figure 7.9 for the calibration pulse shape (the calibration pulse shape is obtained by varying the time between calibration trigger and the readout trigger of the APV). Figure 7.10 shows the gain curve for the calibration unit in peak mode, which shows a different slope before and after irradiation but no off-set. This indicates a charge up of the NMOS transistor oxide-layer with which the charge injected into the preamplifier input is adjusted (for details about the calibration unit see section 5.1.6). As described in section 7.1.6 positive charge, created by ionizing radiation, will be trapped in the silicon oxide near the interface to the silicon bulk. These positive charges will decrease the voltage needed to be applied onto the gate of a NMOS device to get the same conductive channel as for the non irradiated case.

The irradiation of the front-hybrid shows that the readout electronic is fully operational after irradiation. The increased pedestal and calibration signals do not worsen the performance of the readout and could be adjusted to the values before irradiation by changing the corresponding APV settings.

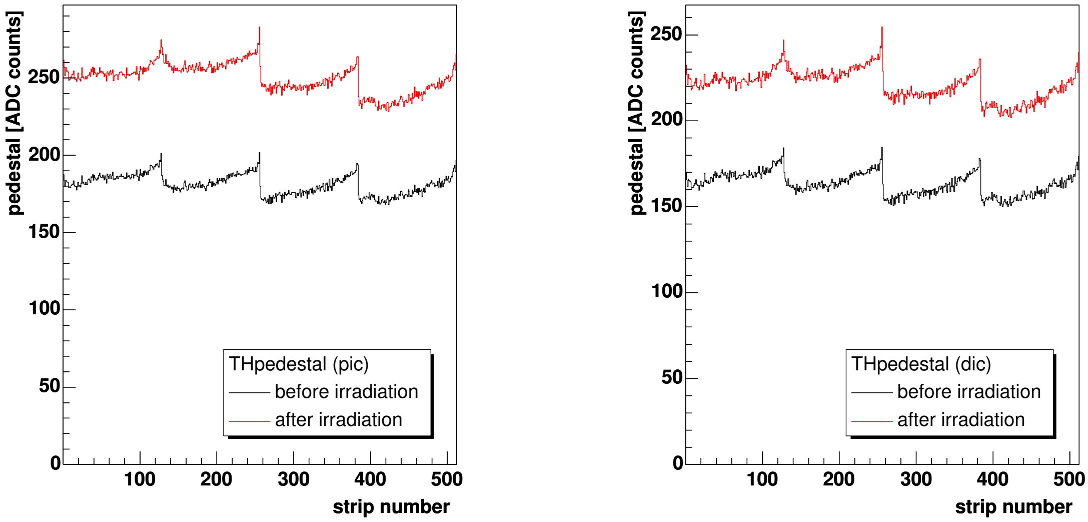

(a) (b)

Figure 7.7: *Pedestal for peak mode inverter on (a) and deconvolution mode inverter off (b) before and after irradiation*

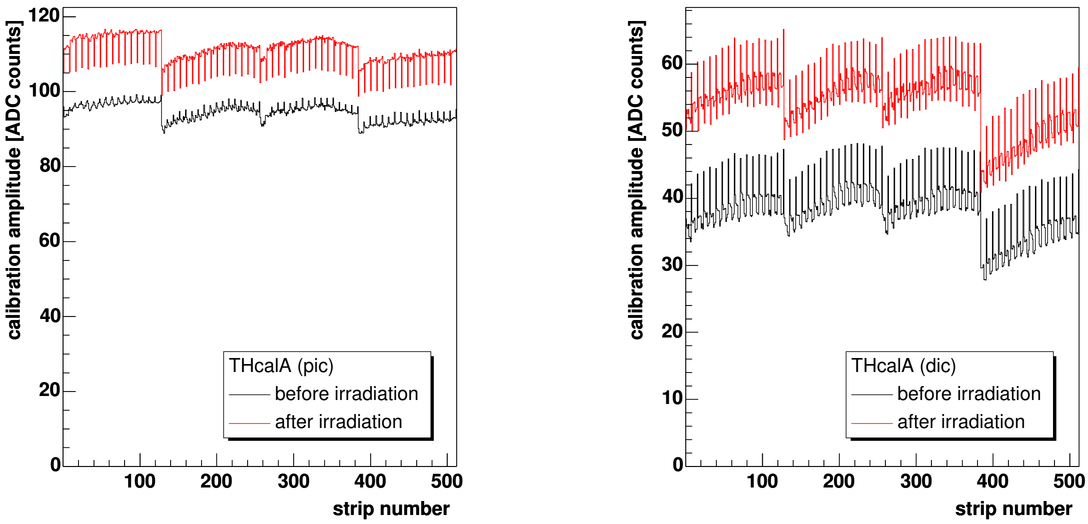

(a) (b)

Figure 7.8: *Calibration amplitude for peak mode inverter on (a) and deconvolution mode inverter off (b) before and after irradiation*

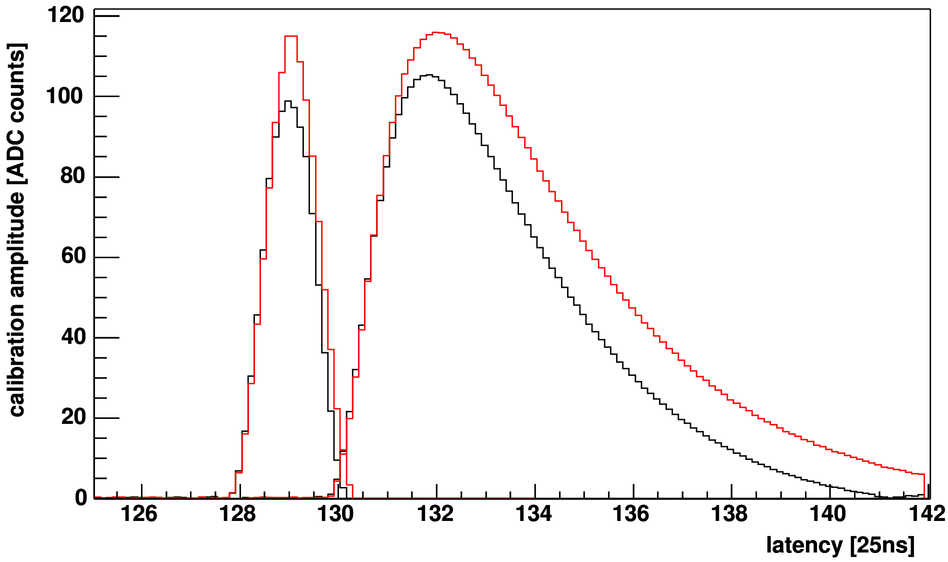

Figure 7.9: *Calibration pulse shape in Peak and Deconvolution mode, before and after irradiation. The slope for each mode is the same before and after irradiation only the pulse height increased in the irradiated case*

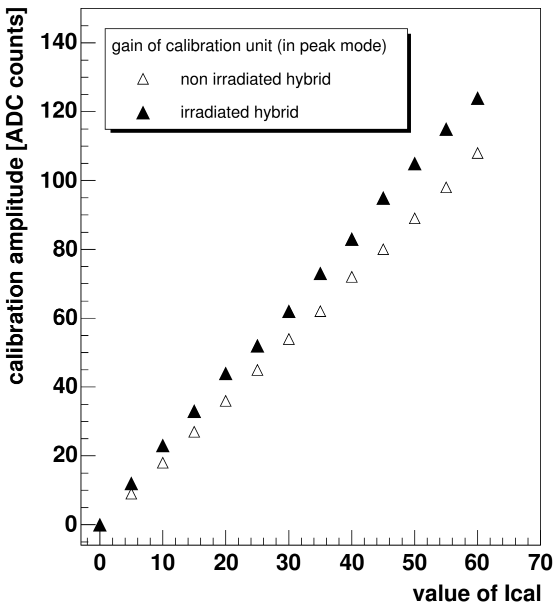

Figure 7.10: *Gain curve of calibration unit in peak mode, before and after irradiation. The slope of the gain-curve increases after irradiation, indicating an increase of oxide-charge in the NMOS transistor responsible for adjusting the injected charge*

7.5 Module Irradiation

After the irradiation study on a front-end hybrid the next step is to investigate complete detector modules. Therefore three TOB modules (500 μm thick sensor, for dimension see appendix C) were irradiated, two with protons to a fluence of 0.69×10^{14} n_{1MeV} cm^{-2} and one with neutrons. The fluence for the neutron irradiated module ranges from 1.3×10^{14} n_{1MeV} cm^{-2} below the front-end hybrid to 0.97×10^{14} n_{1MeV} cm^{-2} at the far end of the second sensor. The highest fluence obtained by the silicon sensor next to the front-end hybrid was 1.21×10^{14} n_{1MeV} cm^{-2}. This is due to the profile of the neutron beam (see figure 7.5) and the resulting positioning of the detector module.

The aim of the irradiation study is to qualify the robustness of the detector design, to proof the radiation hardness of the complete system and to show that the detector can be operated after 10 years of operation at LHC conditions with sufficient SNR. Therefore the annealing behavior of the depletion voltage, the evolution of the leakage current during the annealing steps and the SNR has been studied.

All annealing steps were performed at 60°C in an environmental controlled oven and afterwards stored at room temperature for at least two hours. Between the measurements and the individual annealing steps the modules were stored in a fridge at ≈ -20°C to freeze out annealing processes. The annealing temperature of 60°C is the one proposed by the irradiation qualification center (IQC) of CMS to do the measurements on a reasonable time scale (see table 7.3) and to be comparable with other measurements done throughout the CMS collaboration.

7.5.1 Depletion Voltage Characteristics

The modules depletion voltage can be accessed by the measurement of the modules capacitance voltage characteristic. Therefore the capacitance was measured by a LCR-meter, which modulates an alternating voltage on the reverse bias current and measuring the phase shift between induced current and voltage.

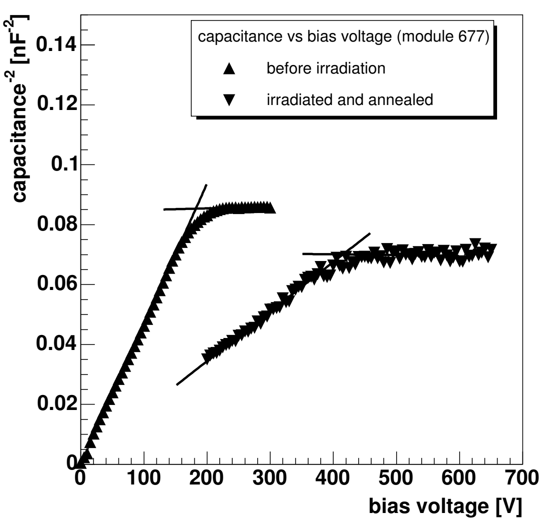

Figure 7.11: *Determination of the depletion voltage from the squared inverse capacitance plotted versus the applied bias voltage, for module 677 before irradiation and after irradiation (to* 0.69×10^{14} n_{1MeV} cm^{-2}*). The measurement after irradiation is shown for an annealing time of* 17.0 *hours at* 60° *C, this is far in the reverse annealing regime*

The CV-measurements were done at the Karlsruhe QTC. The bias voltage was applied through cable bypassing the modules filter capacitors and a micromanipulation probe connecting the ground potential to the bias ring. The module was embedded in the box and cooled as described in section 6.4.3. To extract the depletion voltage from the data, the inverse of the squared capacitance is plotted versus the reverse bias voltage (see figure 7.11), the point of intersection of the two linear regression lines gives the full depletion voltage. The values of the depletion voltage given throughout the text are usually averaged over two to four measurements, the deviation is ≈ 5% from the mean.

The annealing behavior of the detector is an important fact to know for the operation of the central tracker over a period of ten years at the LHC. During this time the are data taking runs intercepted by machine development and maintenance periods when the detector is warmed up to room temperature. In these periods the annealing processes are accelerated compared to the nominal operating temperature of $\approx -10°$C. On one hand it has to be avoided to reach the regime of reverse annealing, but on the other hand it is vital for the operation of central tracker to fully anneal the defects accumulated during the operation period to keep the depletion voltage as low as possible.

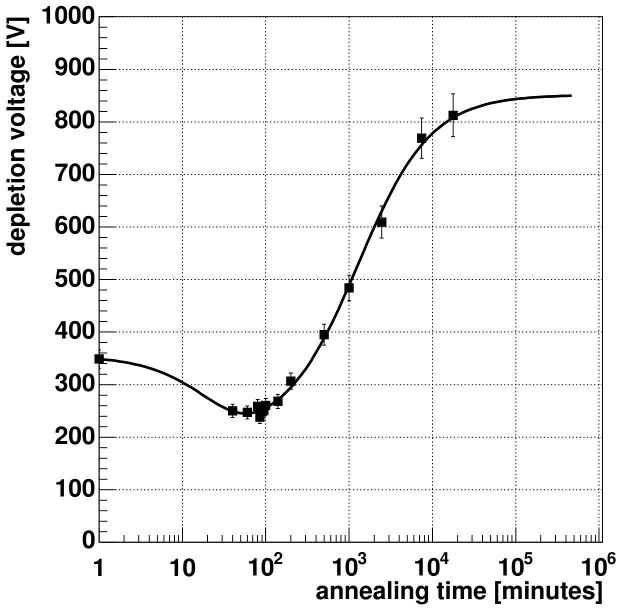

Figure 7.12: *Annealing of the depletion voltage for module 671 irradiated with protons to* 0.69×10^{14} n_{1MeV} cm^{-2}. *The data points are fitted with the "Hamburg model" specified in section 7.1.5.2. The depletion voltage shows a minimum around* 80 *minutes for an annealing temperature of* 60° *C, which corresponds to* ≈ 10 *days at room temperature*

Figure 7.12 and 7.13 show the annealing behavior for the three irradiated modules, all annealing curves show a minimum after 80 minutes annealing at 60°C corresponding to ≈ 10 days at room temperatures. The data for module 671 was fitted for all parameters from the "Hamburg model" using the average values from [mol99] as starting values, the data of module 666 was fitted in the same way but using time constants received for module 671 as fixed input. This was done due to missing data points near the saturation in the reverse annealing. Depletion voltages above 1000 V exceed the limits of the measurement setup and the operation capacity detector module. The data points of module 677 were approximated using the average fit results from two the other modules, the fit values are listed in table 7.4. Figure 7.14 shows the change in depletion voltage versus the accumulated fluence calculated using the fit values received for module 671 and measured values for various modules. From this figure one can estimate the expected depletion voltage during the operation at LHC.

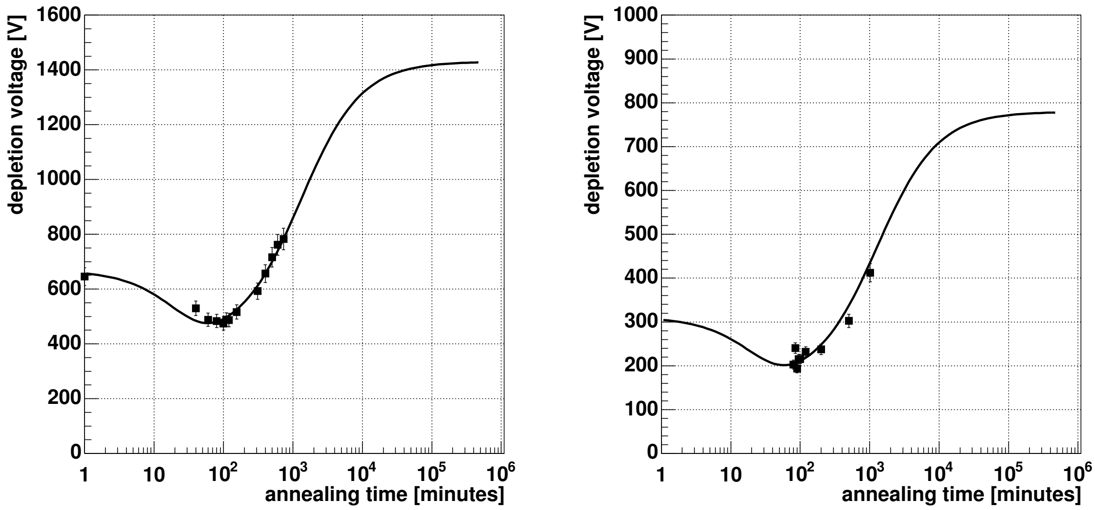

(a) (b)

Figure 7.13: *Annealing of the depletion voltage for modules 666 and 677 annealed at a temperature of* $60°C$. *Module 666 (a) was neutron irradiated to* 1.2×10^{14} n_{1MeV} cm^{-2} *and module 677 (b) was irradiated with protons to* 0.69×10^{14} n_{1MeV} cm^{-2}. *The parameters describing the annealing curve of module 677 are the fit values received from module 671*

module number	g_a $[10^{-2}\ \mathrm{cm}^{-1}]$	$t_a(60°C)$ [min.]	g_y $[10^{-2}\ \mathrm{cm}^{-1}]$	$t_y(60°C)$ [min.]
671	1.11 ± 0.16	21.0 ± 8.0	4.91 ± 0.27	1290 ± 262
666	1.11 ± 0.17	21.0*	4.45 ± 0.39	1290*
average	1.11 ± 0.17	21.0 ± 8.0	4.69 ± 0.34	1290 ± 262

Table 7.4: *Summary of the fit parameters from module 671 and module 666, the annealing times marked with* $*$ *are fixed input parameters for module 666, the averaged in the last row values were used to describe the data of module 677*

7.5.2 Leakage Current Characteristics

In this section the characteristics of the leakage current for the three modules is shown. The guard ring of the modules used in the CMS central tracker is not connected to ground potential, in fact it is floating. This may lead to wrong generation current density values due to the indeterminate active volume of the device, especially after type inversion (see [mol99]).

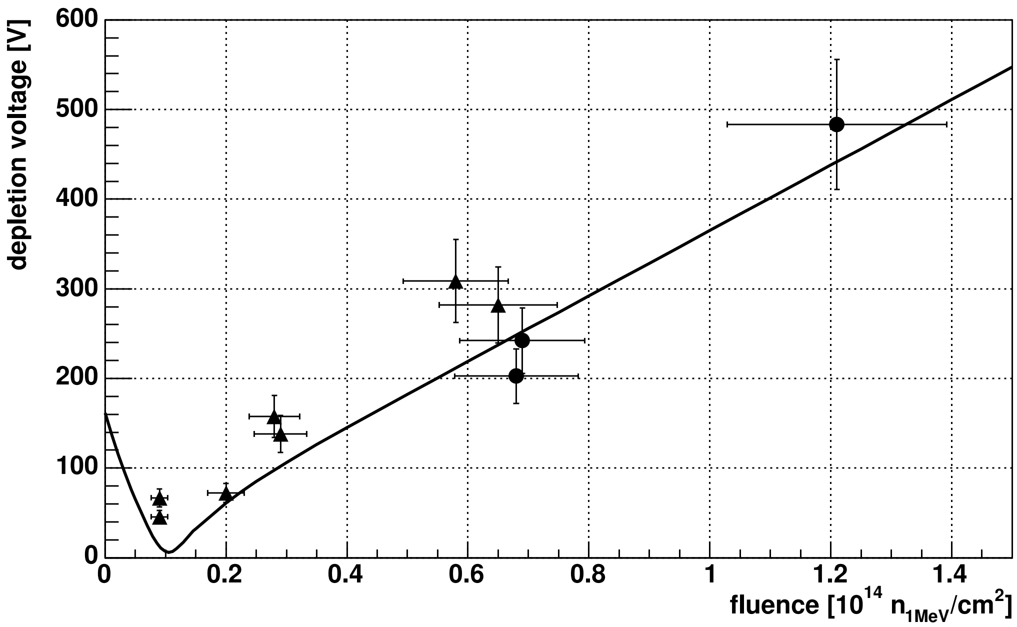

Figure 7.14: *Change in depletion voltage versus accumulated fluence. Calculated using the fit values from module 671, with a annealing time of* 80 *minutes and an annealing temperature of* $60°C$ *after each fluence step. The circles corresponds to the modules used for further investigations in this work, the triangles to modules measured for the irradiation quality control*

The modules studied in this work have been pushed by irradiation far beyond type inversion. The temperatures for the different measurements have been scaled using [mol99]

$$I(T_{ref}) = I(T_m)\left(\frac{T_{ref}}{T_m}\right)^2 e^{\left(-\frac{E_g}{2k_B}\cdot\left[\frac{1}{T_{ref}}-\frac{1}{T_m}\right]\right)} \quad . \tag{7.13}$$

T_{ref} is the reference temperature the current should be scaled to, T_m is the temperature at which the current was measured, E_g is the band gap energy and k_B the Boltzmann constant. The temperature during the annealing study was measured with a Pt-100 sensor, mounted onto the transport frame (aluminum plate to support the module during the qualification procedures before installing it onto a rod or petal). To avoid damages to the sensors or influence the modules noise behavior the temperature at this point was cross checked with six temperature probes mounted on the silicon after the annealing study was finished. The measured leakage current was corrected to the average temperature seen by these probes.

Figure 7.15 shows the annealing behavior of the leakage currents for the cumulated annealing time at 60°C, all currents were scaled to −10°C the operation temperature of the central tracker. The leakage currents show the expected annealing behavior, taking into account uncertainties in the temperature measurements. For annealing times of 80 minutes at 60°C the current related damage rate is calculated, using equation 7.4, to $3,97 \cdot 10^{-17}$ A/cm for module 666, $4,06 \cdot 10^{-17}$ A/cm for module 671 and $3,34 \cdot 10^{-17}$ A/cm for module 677. For the calculations the leakage current was scale to room temperature (20°C), 4.3 cm^3 was

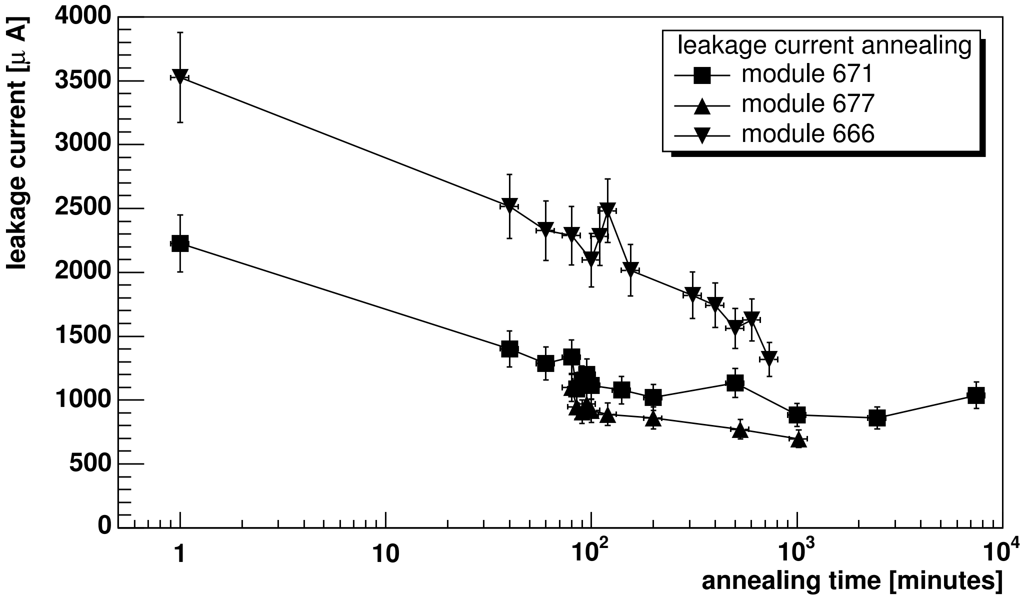

Figure 7.15: *Annealing behavior of the leakage current at* $60°\,C$ *for the three modules. The leakage currents are scaled to* $-10°\,C$*, the operation temperature of the central tracker. Module 666 was irradiated with neutrons to* 1.21×10^{14} n_{1MeV} cm^{-2} *and module 671 and 677 with protons to* 0.69×10^{14} n_{1MeV} cm^{-2}

assumed as active volume per sensor and the appropriate fluence the modules was exposed to. Considering that the guard ring was not connected, the uncertainties in determination of the fluence and the uncertainties in the temperature measurement of at least $\approx 1°$C, these values are comparable to measurements on sensor basis, see [mol99, die03a].

7.5.3 Signal to Noise

The signal to noise ratio is an important variable for the understanding of the detectors response and a vital test for the qualification of irradiated detector modules. Most of the test are done using a ^{90}Sr source (compare section 6.4.2). The SNR obtained from cosmics and source measurements are comparable (see e.g. figure 7.16a). However, the much shorter exposure time for the SNR measurement with the radioactive source compared to that with cosmics ray particles is in favor of the source measurement. A detailed study of the behavior of the SNR for non-irradiated CMS silicon strip modules can be found in [dir03].

All measurements were carried out in the diagnostic test-station described in section 6.4. The modules were cooled to $\approx -15°$C to guarantee a leakage current below 1 mA, the limit of the power supply used. The delay time between the trigger signal generated by the particles coincidence and the trigger send to readout electronics was adjusted after each annealing step if necessary to obtain the optimum SNR. For each voltage step around 5000 events were recorded and the resulting energy loss distribution analyzed by fitting a Landau distribution convoluted with an Gaussian distribution (see appendix E).

The SNR is expected to increase with voltage below full depletion, due to the increase of the space charge region scaling with the square root of the bias voltage (see equation 4.24). After full depletion of the detector is reached the SNR saturates in a plateau. Still a small increase with bias voltage is observed. This increase of the SNR after full depletion depends on the increase of the electric field strength and therefore on the increase of the drift velocity, this means that more charge is collected during the sampling time of the preamplifier.

In figure 7.16 to 7.18 the SNR versus bias voltage is plotted. Before irradiation all modules show the expected behavior, the saturation of the SNR start at bias voltage which is about a factor of 1.4 larger than the measured depletion voltage. This is in good agreement with previous measurements [dir03] and test beam results [fri01].

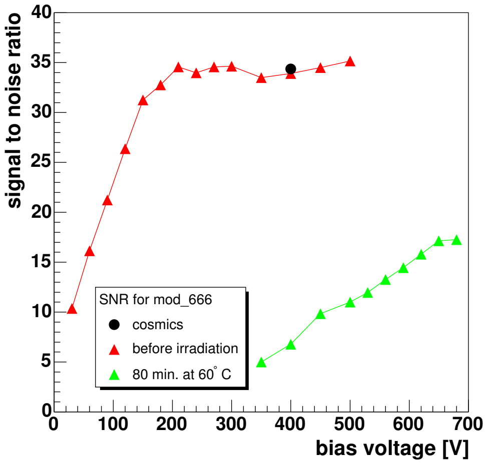

(a)

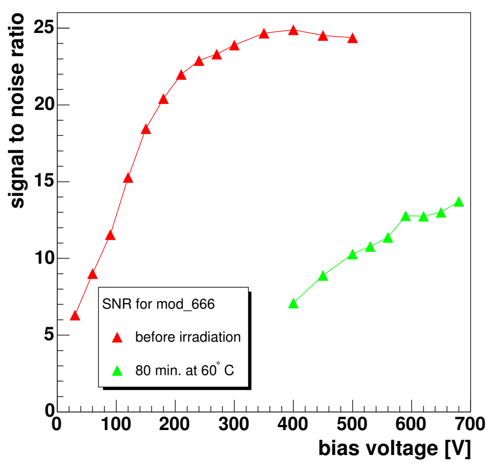

(b)

Figure 7.16: *Signal to noise ratio for module 666 (a) peak mode inverter off, (b) deconvolution mode inverter off, before and after irradiation to* 1.21×10^{14} n_{1MeV} cm^{-2}

module number	**particle type**	**fluence** $[10^{14}$ n(1MeV)/cm$^2]$	**SNR** peak mode	**SNR** deconvolution mode
666	neutron	1.2	33.9 → 17.3	24.9 → 13.7
671	proton	0.7	35.5 → 21.3	23.2 → 15.7
677	proton	0.7	35.5 → 24.3	23.2 → 18.0

Table 7.5: Summary of signal to noise data for all measured modules. The SNR values before irradiation correspond to a reverse bias voltage of 400 V for all modules, after irradiation the values for module 666 correspond to a reverse bias voltage of 680 V and 400 V for the two proton irradiated modules

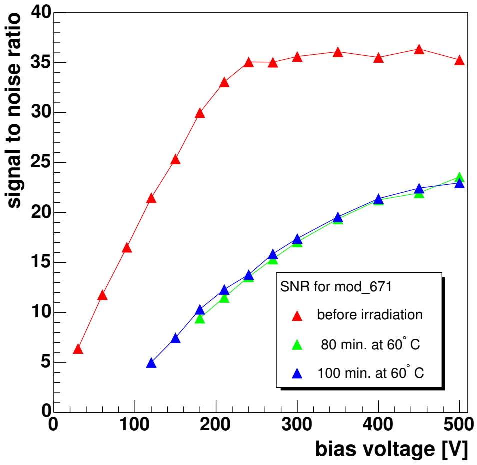

(a)

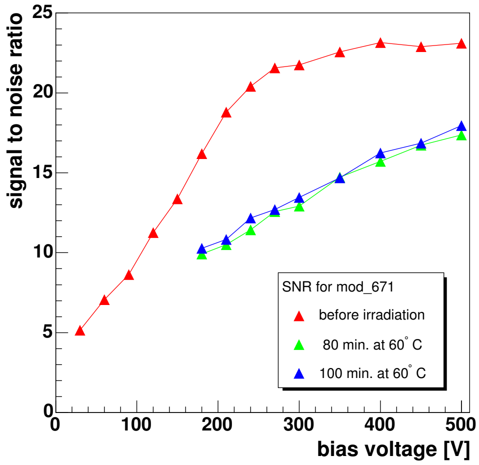

(b)

Figure 7.17: *Signal to noise ratio for module 671 (a) peak mode inverter off, (b) deconvolution mode inverter off, before and after irradiation to* 0.69×10^{14} n_{1MeV} cm^{-2}

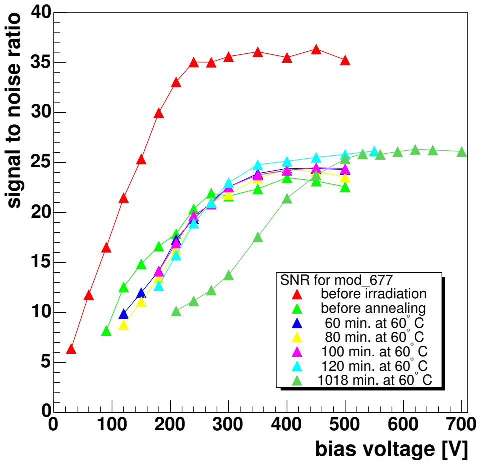

(a)

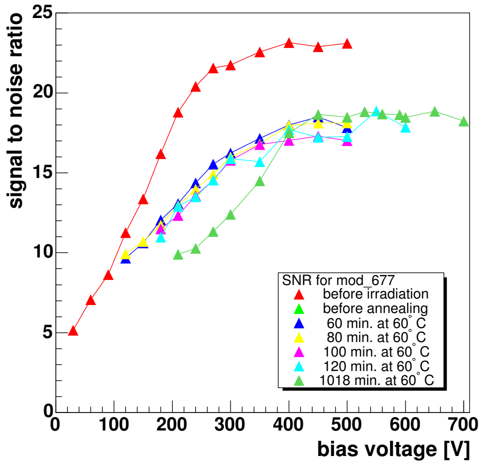

(b)

Figure 7.18: *Signal to noise ratio for various annealing steps on module 677 (a) peak mode inverter off, (b) deconvolution mode inverter off. Before and after irradiation to* 0.69×10^{14} n_{1MeV} cm^{-2}

After irradiation the start of the plateau is expected to be shifted to higher bias voltages due to the increase of the depletion voltage. For module 677 (see figure 7.18) the data fits good to the values expected from the measured depletion voltage. Module 666 was irradiated to a much higher dose and therefore the plateau in the SNR is expected to start above ≈ 650 V reaching the voltage limit of the used high voltage supply. For module 671 (see figure 7.17) the change in the slope starts at around 400 V but no real saturation shows up in the data up to 500 V.

In table 7.5 the measured SNR for the nominal operation voltages are summarized. The SNR measurement shows that the CMS silicon-strip detector modules can still be operated with sufficient safety margin at higher fluences.

7.5.4 Cluster Size

The cluster size is not expected to change due to radiation damage, since the charge creation and drift processes should stay the same as for a non-irradiated detector. Only some amount of the charge created by an ionizing particle passing through the detector may be trapped as explained in section 7.1.5.3 and therefore not contributing to the signal.

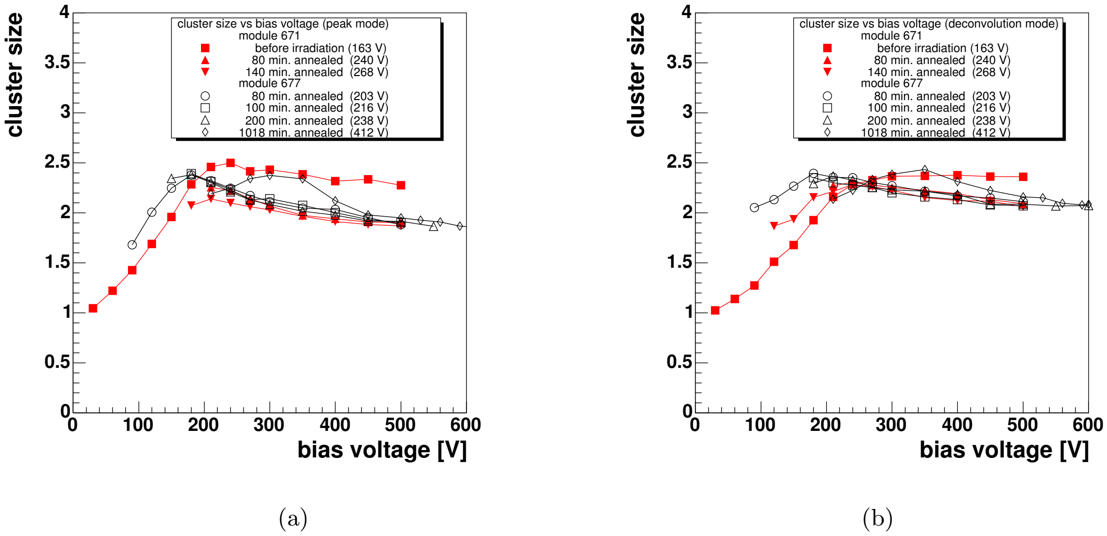

Figure 7.19: *Cluster size versus voltage for module 671 and module 677 (a) in peak mode and (b) deconvolution mode. The voltages in brackets are the measured depletion voltages. The criteria applied for a strip contributing to the cluster signal (see appendix E) was not changed, which explains the smaller cluster size after irradiation due to the increased noise (see text)*

In figure 7.19 the cluster size for module 671 and module 677 versus the bias voltage before and after irradiation for different annealing times are shown for both peak and deconvolution mode. The different cluster size for peak and deconvolution mode is due to the clustering algorithm (see appendix E). Every strip which has a signal with at least three times the noise contributes to the cluster signal. Taking into account that the deconvolution mode noise is higher than that of the peak mode (see table 4.1), one expects a smaller cluster size for the deconvolution mode. After irradiation the detector noise is increased due to the increased leakage current and change in total capacitance, which explains the decreased cluster size. The decrease in the cluster size for higher bias voltages seen in the data is due to increased electrical field limiting the transverse diffusion.

7.5.5 Inter-strip Capacitance

During radiation qualification measurements on neutron irradiated sensors which have been done at the IQC in Karlsruhe, it was observed that the inter-strip capacitance reaches its minimum value only if the sensor is over-depleted. Figure 7.20a shows this behavior of the inter-strip capacitance for a neutron irradiated W6a sensor (for the various sensor geometries used in the CMS tracker see appendix C).

The inter-strip capacitance enters directly into the detector noise (see section 4.3.3 and table 4.1). As seen in figure 7.20 the behavior of the inter-strip capacitance is also seen in the detectors noise. The modules noise decrease significantly after full depletion is reached. The voltage range of this decrease is comparable with the one seen in the inter-strip capacitance. It should be mentioned that the sensor data is from W6A type sensor,which was irradiated with neutrons to a comparable fluence as module 666.

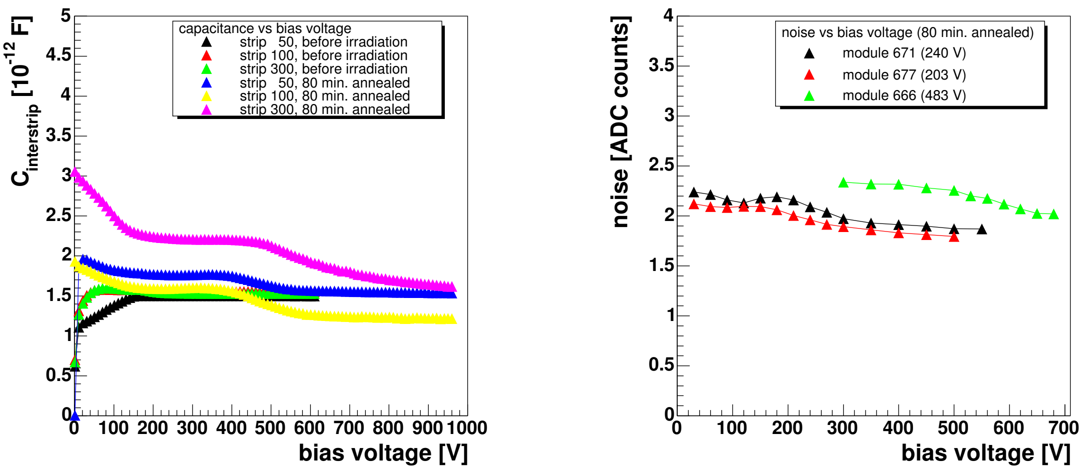

Figure 7.20: *(a) Inter-strip capacitance C_{int} for sensor irradiated with neutrons to a fluence of $\approx 1.0 \times 10^{14}$ n_{1MeV} cm^{-2}. The depletion voltage is measured to 564 V after 80 minutes annealing at 60° C. (a) the average noise versus voltage for all three irradiated modules, after 80 minutes annealing at 60° C, the values in brackets are the corresponding depletion voltages*

7.5.6 Conclusion

The irradiation studies on full detector modules proves the robustness of the CMS detector design. No electrical, as well as, no mechanical problems on the three detector modules and one front-end hybrid occurred after irradiation to a fluence corresponding to 10 years operation at LHC. The characteristics of the depletion voltage and the leakage current are in good agreement with measurements performed on sensor basis. The measured SNR before and after irradiation comply with the requirements needed for CMS and still offers sufficient margin in the case that the expected fluences were underestimated.

Chapter 8

Investigation of Module Faults

Quality control measurements reveal on silicon strip sensors from one of the manufacturers (ST Microelectronics) various problems. One type of these problems applies to the inter-strip resistance, whose saturation behavior deviates strongly from the normal one. Another problem is found in the strip leakage current, where some strips show up to some μA instead of the typical 10 nA. Moreover in some cases the leakage current is depending on mechanical stress. Therefore strong concerns came up on the longterm performance and stability of detector modules built out of such sensors. In this section measurements performed on modules built of such sensors, one with bad inter-strip resistance and two with leakage current problems, are presented. Finally, irradiation induced strip faults are studied.

8.1 Influence of Inter-strip Resistance on Module Performance

Measurements of the inter-strip resistance (R_{int}) on some sensor batches showed a strange behavior. Normally the resistance raises steeply with the bias voltage and saturates around $\approx$ 30 V. On some sensors problematic regions are observed, where the inter-strip resistance did not saturate below 100 V or even not below the depletion voltage. Figure 8.1 shows the inter-strip resistance versus the bias voltage for a sample of strips across such defective sensors. The saturation of R_{int} starts for some strips around the nominal voltages, other strips, in the region between strip 63 to 313, saturate above 100 V. As it is expected that R_{int} affects the noise performance of a strip this has to be investigated.

In figure 8.2 and 8.3 the noise behavior and calibration amplitude in peak and deconvolution mode for the module built of sensors with low inter-strip resistance is shown. For these plots the bias voltage was ramped up to 300 V in 30 V steps and further on in 50 V steps up to 550 V. The noise decreases from around 4 – 6 ADC counts at 30 V (the upper line in figure 8.2a and b) to $\approx$ 2.2 ADC counts after full depletion ($\approx$ 180 V). In peak mode there is still a conspicuous pattern in the noise distribution in the region where the lower inter-strip resistances have been measured. The same behavior can be observed in the calibration amplitude (see figure 8.3), which starts at lower values and saturates after depletion. Figure 8.4 shows for comparison scans of noise and calibration amplitudes in peak mode over bias voltage for a module with normal inter-strip resistance behavior. The noise is slightly increased before full depletion due to the increased detector capacitance before full depletion is reached (see section 4.3.3). This effect is small compared with these seen in figure 8.2 and 8.3.

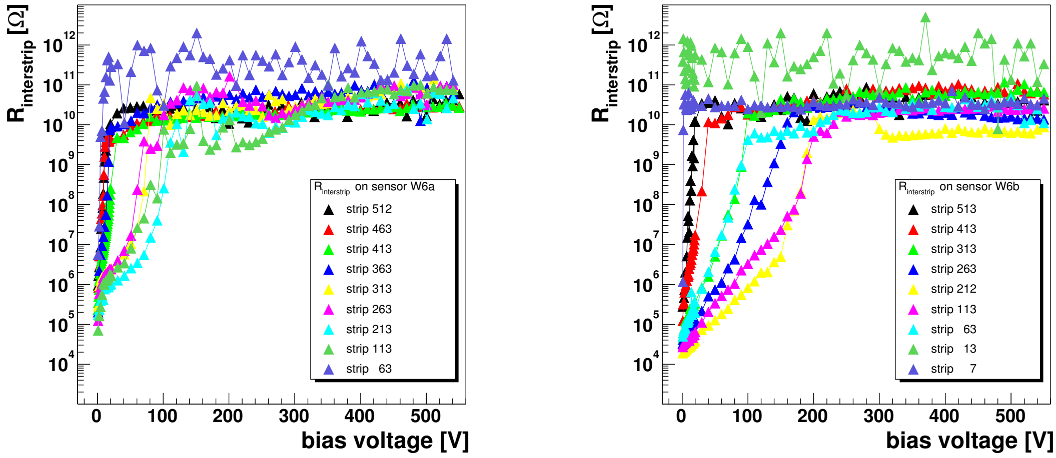

(a) (b)

Figure 8.1: *Measurement of inter-strip resistance versus bias voltage on (a) W6A and (b) W6B sensors for a sample of strips across the sensor*

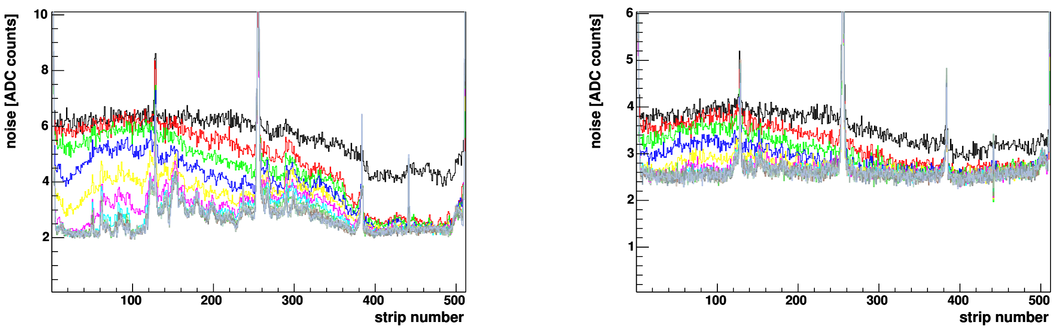

(a) (b)

Figure 8.2: *Noise of a module, whose inter-strip resistance saturates after the module is fully depleted, scanned in steps of* 30 *V up to* 300 *V and from there to* 550 *V in steps of* 50 *V. The noise decreases from* 4 *–* 6 *ADC counts (black line) at* 30 *V down to around* 2.2 *ADC counts after full depletion. (a) In peak mode there are still regions with strong deviations from the mean which correlates perfectly with the region of low inter-strip resistance, while in deconvolution mode (b) this is less distinct*

The behavior of the inter-strip resistance seen in figure 8.1, indicates the presences of negative charges in one of the oxide layers. If the negative charges overcompensate the positive charges normally present in the silicon to silicon oxide interface, then a conductive channel

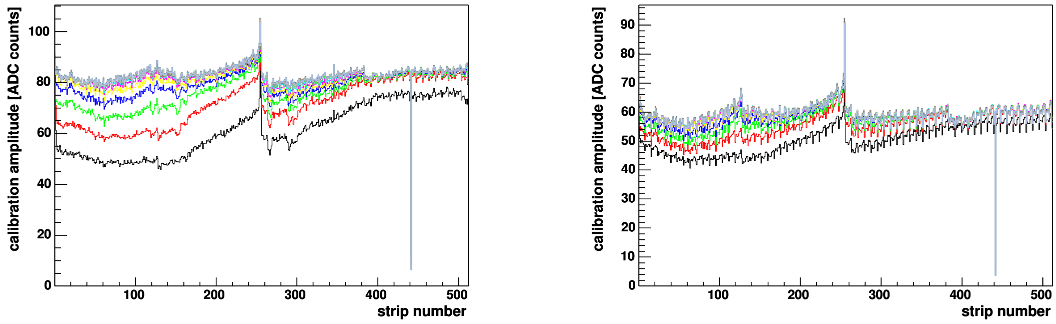

(a) (b)

Figure 8.3: *Calibration amplitude for the low R_{int} module, the voltage ramps are the as for figure 8.2. The calibration signals start at lower values (black line) and saturate above the depletion voltage, (a) peak mode and (b) deconvolution mode*

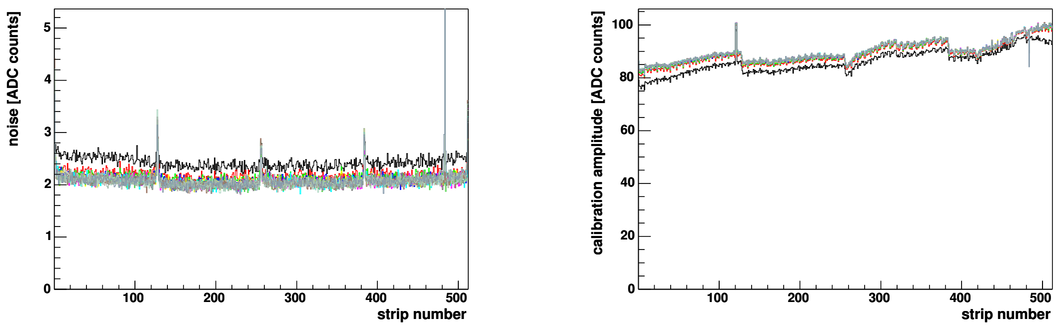

(a) (b)

Figure 8.4: *(a) Noise and (b) calibration amplitude in peak mode, for module 671 (TOB geometry) with normal behavior in inter-strip resistance. In both plots the curves saturate above a bias voltage of* ≈ 60 *V*

between the p-implants is formed, lowering the inter-strip resistance (compare figure 8.5). Investigations throughout the CMS collaboration and by the manufacturer suggested, that the passivation layer (see figure 8.5) contains a high concentration of negative charges. In a study of the CMS group in Strasbourg on the same module presented in this section, the passivation layer was etched away with a special solvent and the noise distribution was compared before and after this treatment. Figure 8.6 shows the results of these measurements. Curve (a) shows the noise distribution for a normal module, where the noise is well distributed around 1.6 ADC counts. Curve (b) shows the noise for the module built of the low R_{int} sensors before the passivation layer was removed. A higher noise contribution of the affected area is seen. After the passivation layer was etched away the noise behavior changed dramatically, see curve (c). The former noisy region became flat, as expected from a normal detector module. However, now the edges of the modules show a highly increased noise.

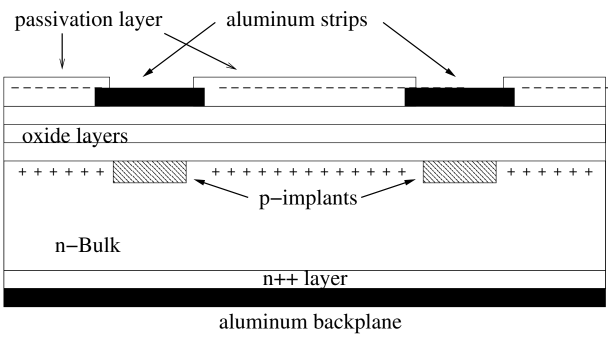

Figure 8.5: *Schematic structure of a silicon strip detector. This schematic shows two aluminum strips with their underlying p-implants. In between there are several oxide layers. The surface of the upper oxide layer is coated by a passivation layer. If this passivation layer inclose enough negative charge to overcompensate the positive charge in the silicon to silicon-oxide interface, a conductive channel of p-type between the p-implants will be formed*

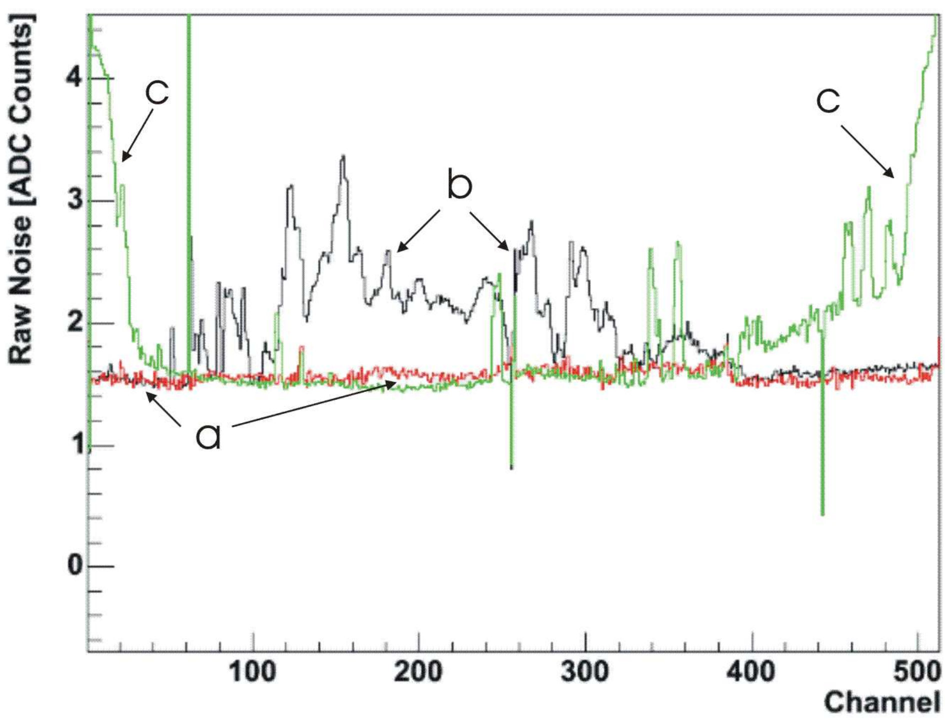

Figure 8.6: *Comparison of data from normal module curve (a) with the low R_{int} module curve (b) and the low R_{int} module after removing the passivation layer over the aluminum strips and the oxide layer curve (c). These measurements were done in Strasbourg* [hov04]

8.2 Influence of Leakage Current on Strip Noise

On some sensor batches, measured by the QTC throughout the CMS collaboration, a dependence of the leakage current on mechanical deformations of the sensor was observed. This leakage current is driven by only a few strips, while the sensor was sucked by vacuum to the QTC measurement jig. On some of these sensors strips with a leakage currents up to a few μA were measured. Figure 8.7 shows the behavior of the global leakage current versus bias voltage for such a sensor. The leakage current exceeds 10 μA at 500 V in the case of strong deformation of the sensor. It is obvious that such a behavior may influence the performance

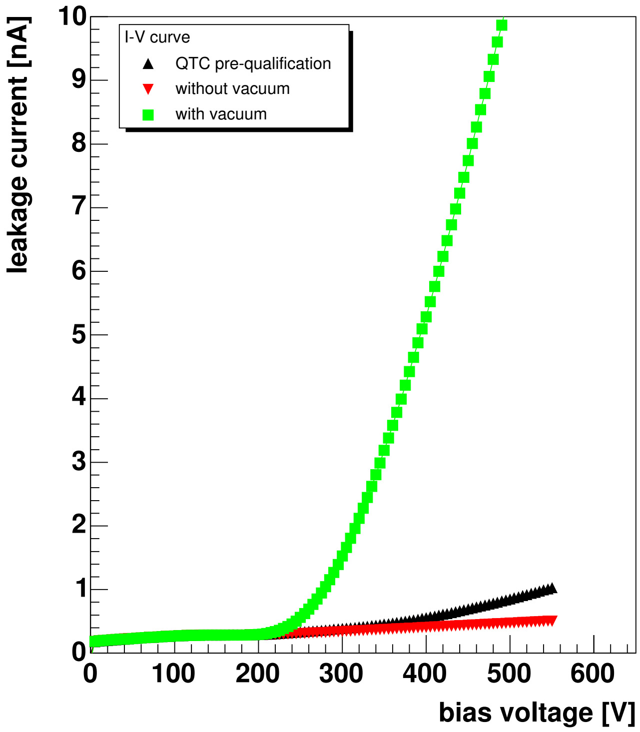

Figure 8.7: *Dependence of the sensor leakage current on mechanical stress. This measurement was done on a W6A sensor. The leakage current increases up to* 10 μA *at around* 500 *V in the case of strong deformation of the sensor*

of the whole tracker, since modules are mounted on rods or petals and thus exposured to a certain amount of mechanical stress, which will possibly increase when the system is cooled to the operation temperature.

Two ring 6 modules (in the text and figures just called module 1 and module 2) were built out of such sensors to investigate these problems. The aim of these measurements was to reproduce the leakage current behavior on fully equipped modules and to study the influence of the strip leakage current on the noise. Both modules were built with the final components and glues used in the experiment to achieve the most realistic testing conditions. The deformation was applied by placing weights on the sensor. To avoid damage to the surface by scratches or the short-circuit of strips the sensor was protected by glueing Teflon tape to the weights or inserting Teflon paper between weight and sensor. Figure 8.8 shows a view inside the diagnostic station with weights applied on a module. With a micromanipulation probe the strip leakage currents were measured strip by strip. The global leakage current was monitored for each of these measurements. Furthermore the noise was measured in separate runs, because the micromanipulation probe strongly affects the modules noise behavior, since it acts as an antenna.

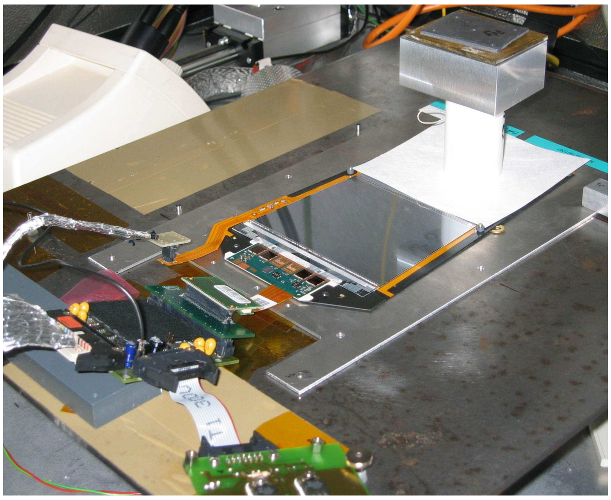

Figure 8.8: *View inside the diagnostic test-station, a weight of ≈ 600 g is applied on the module, a Teflon paper (white tissue) between the sensor and the weight avoids scratches on the surface and short-circuits*

Figure 8.9 shows the global leakage current of module 2 recorded during the measurements of the different strip leakage currents. Comparing the characteristics of this plot with a normal I-V curve (lower curve in figure 8.7), two kinks in the slope can be identified. The positions of these two kinks correlate with the increase of the leakage current of affected strips shown in figure 8.10. While the lower kink arises from sensor W6A, is the upper kink driven by strip 408 on the W6B sensor.

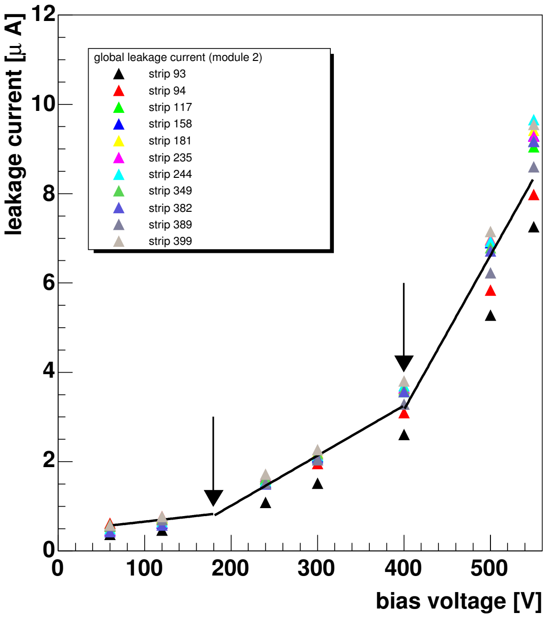

Figure 8.9: *Global leakage current measured on detector module 2. Each curve was taken during the measurement of the leakage current on a single strip. The curve shows two kinks (indicated by arrows) correlated to the increase of the leakage current of certain strips. See figure 8.10 for the corresponding strip leakage currents*

In figure 8.11 the noise distribution for both modules is plotted for a bias voltage of 450 V without any stress applied. Module 1 shows three noisy strips (12, 308, and 341) and one

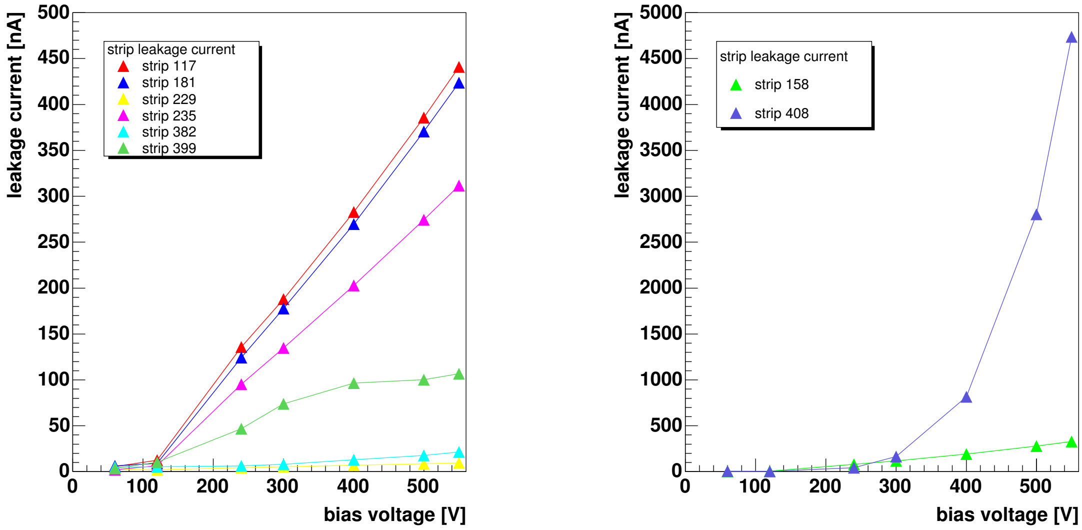

(a) (b)

Figure 8.10: *Strip leakage current for strips showing an increased leakage current measured on sensor W6A (a) and sensor W6B (b), these few strips are responsible for the main part of the global leakage current of the module*

short (191/192). Module 2 shows two noisy strips (399 and 408), one short (104/105) and one pinhole at strip 229 (see figure 8.11). From equivalent noise charge (ENC) calculation according to table 4.1, the additional noise expected from a strip leakage current of 400 nA due to shot noise is approximately 0.2 ADC counts. Therefore most of the leaky strips shown in figure 8.10a are not expected to been prominent in the noise distribution, as long as they show a shot noise behavior. The strips at the borders of an APV chip exhibit an increased noise as well, which however, can be reduced by a proper grounding.

Figure 8.12 shows the noise for strip 308 and 341 on module 1 with different weights loaded and additional deformations induced by bending the detector module frame. The bending of the frame was done by putting on one side a spacer underneath the frame near the fixation screws. This introduces a certain amount of torsion to the sensor. Moreover the modules were tested with thermal stress by cooling them down to ≈ -17°C. During this thermal test no additional weights were applied to the sensor. Strip 308 shows a small dependence in noise, whereas in case of strip 341 the dependence is much stronger but still not critical for the operation of this module. Another example of strip noise behavior is shown in figure 8.13 for strip 408 and 399 on module 2. Here strip 399 (figure 8.13b) shows a strong dependence on the applied stress. The noise distribution of strip 408 (figure 8.13a) shows the same shape for nearly all measurements done, except for the measurement with thermal stress and the measurement where a weight was applied on sensor B. This can be explained by the fact that the leaky strip is on the sensor next to the front-end hybrid (sensor B) and should therefore not be affected by stress applied on the sensor at the far end of the module (sensor A).

The noise and leakage current behavior as shown in figure 8.12 and 8.13 was measured

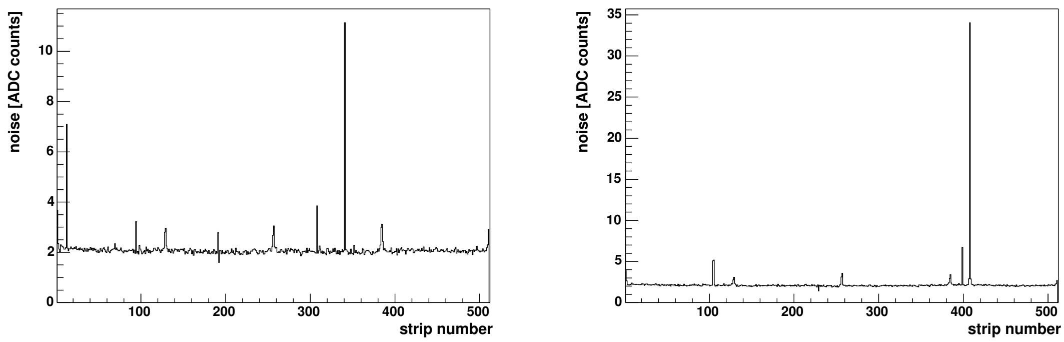

(a) (b)

Figure 8.11: *Global noise of modules with high strip leakage current for a bias voltage of* 450 *V. (a) module 1 strips* 12, 308 and 341 *have a very high noise, strips* 191/192 *are shorted, the boarders of the APV chip show also an increased noise. (b) In module 2 strip* 399 and 408 *show an increased noise, strip* 104/105 *are shorted, on strip* 229 *is a pinhole. Again the APV chip boarders are increased in noise*

on 22 different strips on two modules for different kinds of deformation. The values of the leakage current have been compared with the values measured by the QTC. For sensor A an additional post-qualification was done by the QTC. All these values for a bias voltage of 400 V are summarized in table 8.1 and table 8.2. Figures are collected in appendix F. The noise given in these tables corresponds to the unstressed case.

Comparing the strip leakage current results from the QTC on sensor basis with the module basis ones, it was observed that strips with very high leakage current seen by the QTC showed no increased leakage current on the module (e.g strips 265/266 on module 1). Removing those sensors from the modules and repeating the qualification of the sensors on the probe station showed no increase of the current, as well. On the other hand strips are observed (e.g. strip 308/341) in the module noise distributions, which showed no increased leakage current in the QTC pre-qualification but showed an increased leakage current on the module and in the post-qualification of the sensor.

A sharp limit for the leakage current at which the module noise increases significantly could not be given. Most of the problematic strips showed up in noise at a leakage current above 400 nA. This current creates a voltage drop over the bias resistor of ≈ 0.7 V, which is equivalent to the voltage on the aluminum strips (virtual ground of the APV), leading to a stronger field on the p-implant.

The measurements showed that the huge increase of the leakage current due to mechanical stress, seen on some sensors, could not be reproduced on the modules. But all strips showing an increased noise are affected by mechanical and thermal stress, which may be critical for the operation of the tracker. No additional noisy strips were created during these measurements. Furthermore, the measurements showed for the used type of problematic sensors, that it is not always possible to transfer the sensor qualification results directly to module strip faults. This is particularly true for leaky strips which may appear or dissappear on the module.

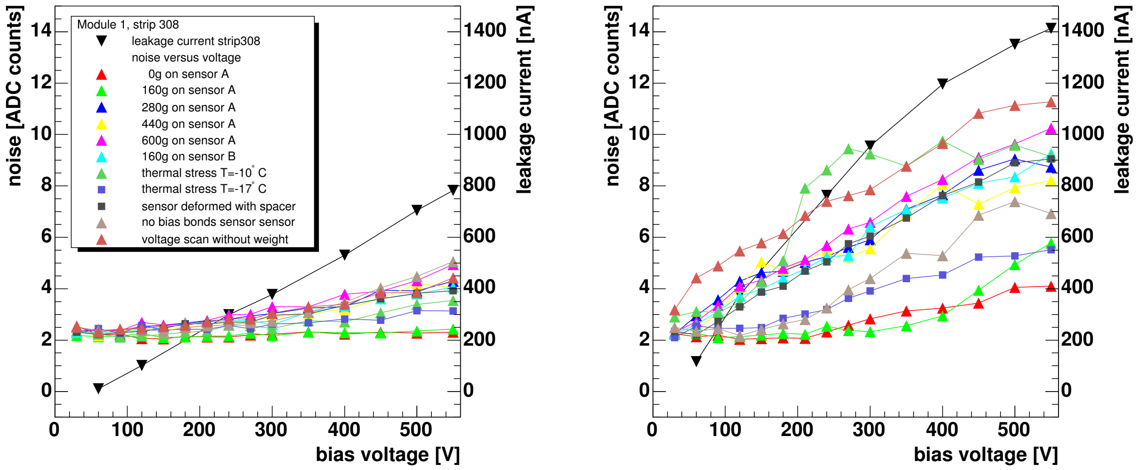

(a) (b)

Figure 8.12: *Noisy strips measured on module 1. Here the noise for different mechanical deformations, thermal stresses and the leakage current for the unstressed case as function of the bias voltage are plotted for strip 308 (a) and strip 341 (b). Both strips show a dependence on mechanical and thermal stress. The legend in plot (a) applies for both figures*

Module 1		leakage current [nA]			noise	figure
strip #	sensor	QTC (pre)	Module	QTC (post)	[ADC counts]	
12	B	1080.00	642.30	–	4.77	F.1
98	B	232.00	182.89	–	2.07	F.1
106	A	183.00	173.76	205.13	2.16	F.2
115	A	358.00	326.10	394.77	2.10	F.2
180	A	208.00	205.00	239.70	2.15	F.2
265	A	5230.00	1.76	2.46	2.11	
266	A	5210.00	1.54	1.19	2.09	
308	A	1.30	530.00	242.40	2.24	8.12
312	B	218.00	185.95	–	2.03	F.3
341	A	3.90	1195.50	1375.73	3.25	8.12
352	A	11.50	59.18	173.33	2.11	F.3
429	A	108.00	93.82	122.66	2.04	F.3

Table 8.1: *Comparison of strip measurements on sensors and module. The values of the leakage current and noise correspond to a bias voltage of* 400 *V. The noise contribution is shown with no mechanical stress applied. For higher bias voltages the noise of strip* 12 *and* 341 *increases to* 7.05 *and* 4.09 *ADC counts. The post qualification of the sensor was only done on sensor A*

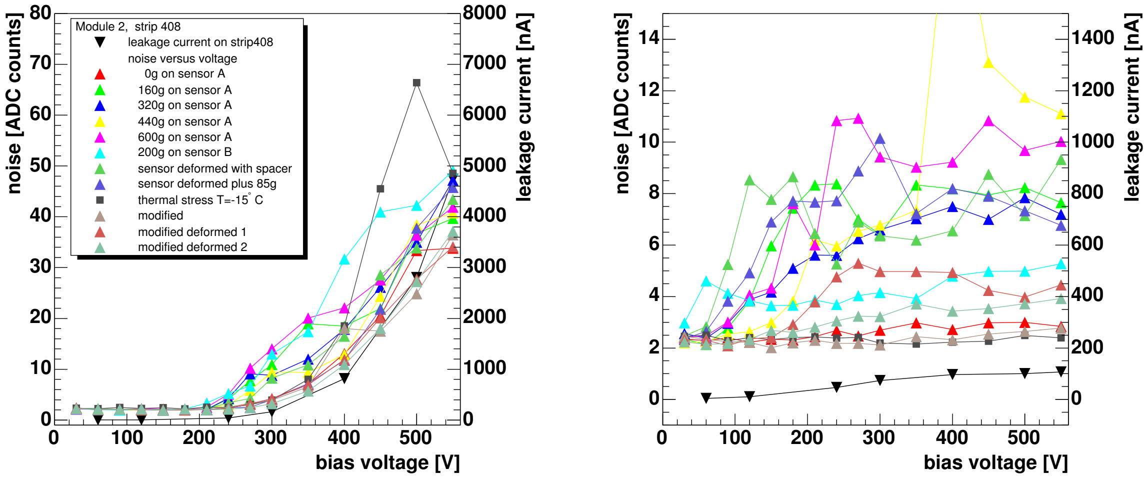

(a) (b)

Figure 8.13: *Noisy strips on module 2, here the noise for different mechanical deformation, thermal stress and the strip leakage current for the unstressed case as function of the bias voltage is plotted for strip 408 (a) and strip 399 (b). The leakage current for strip* 408 *was measured on the sensor next to the hybrid. At least strip* 399 *shows a dependence on the applied stress, for strip* 408 *it has to be taken into account that the leaky strip is on the sensor next to front-end hybrid and therefore the unaffected by most measurements. The legend in plot (a) applies for both figures*

Module 2		leakage current [nA]			noise	figure
strip #	sensor	QTC (pre)	Module	QTC (post)	[ADC counts]	
93	A	1300.00	1.23	0.67	2.11	
94	A	2790.00	0.48	0.65	2.09	
117	A	379.00	282.90	393.63	2.19	F.4
158	B	182.00	193.20	–	2.18	F.4
181	A	318.00	279.70	338.83	2.10	F.4
229	A	6.38	7.03	6.95	4.72	F.4
235	A	282.00	202.80	289.15	2.08	F.5
382	A	6.83	12.97	6.33	2.36	F.5
399	A	2570.00	96.41	74.41	2.72	8.13
408	B	2160.00	817.20	–	13.10	8.13

Table 8.2: *Comparison of strip measurements on sensors and module. The values of the leakage current and noise correspond to a bias voltage of* 400 *V. The noise contribution is shown with no mechanical stress applied. For higher bias voltages the noise of strip* 408 *increases to* 33.81 *ADC counts, strip* 229 *is a pinhole. The post qualification of the sensor was only done on sensor A*

8.3 Irradiation Induced Strip Faults

Section 7.5 showed that modules behave perfectly in terms of depletion voltage, leakage current and signal to noise ratio (SNR) even after being irradiated to the expected fluence of ten years of LHC. Another important factor for the operation of modules in experiment is the number of strips lost due to radiation induced defects in the sensor or the electronics. Therefore the three modules, used for the irradiation studies in section 7.5, have been investigated for additional strip faults after irradiation. These modules were built of sensors from ST Microelectronics (STM). Two of the modules were irradiated with protons and one with neutrons, see section 7.5 for details.

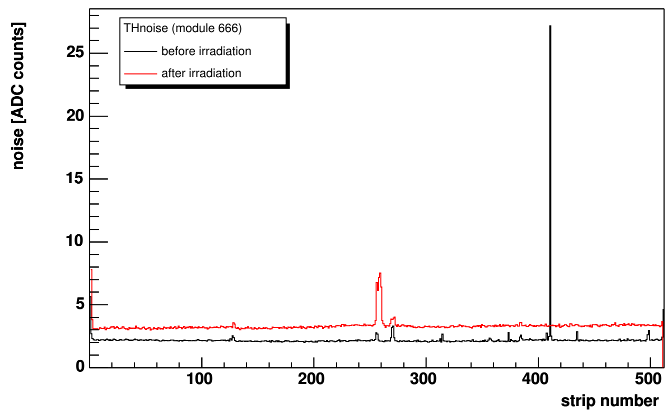

Figure 8.14: *Comparison of module noise before and after irradiation (with neutrons),* $V_{bias} = 500$ *V and* 80 *minutes annealing at* $60°C$*. After irradiation the region between strip* 256 *and strip* 260 *shows an increased noise distribution. Strip* 411 *with a very high noise before irradiation completely disappeared in the noise*

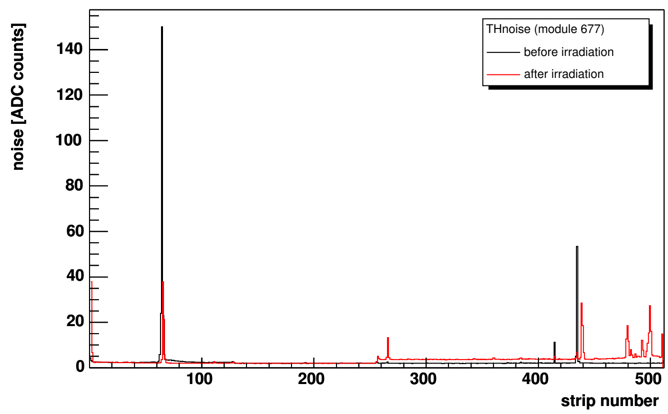

Figure 8.15: *Comparison of the noise distribution before and after irradiation (with protons) of module 677, at* $V_{bias} = 500$ *V and after* 80 *minutes annealing at* $60°C$*. This module shows several noisy strips after irradiation, e.g. strip* 266*, strip* 65 *to* 66*, strip* 439 *to* 441 *and strip* 479 *to* 501

Figure 8.14 to 8.16 show the noise behavior before and after irradiation (80 minutes annealed at 60°C,) at a bias voltage of 500 V. For all three modules regions with increased noise are observed. The two proton irradiated modules are affected mainly in the region around strip 480 to 500. The neutron irradiated module shows a region of increased noise after irradiation between strip 256 and 260. It is worth to mention, that one strip seen in the noise before irradiation completely disappeared. The latter can be explained by the increased depletion voltage ($\approx$ 480 V) and type inversion. Especially the type inversion, where the space charge region starts to grow from the backside of the detector, reduces the electric field on the strip side significantly. This delays a local breakthrough of a strip to higher voltages.

To be sure the strips shown up in the noise are related to sensor faults and not to failures in APV channels the calibration signal was used to check the amplifiers response. Figure 8.17 shows the calibration signal for module 671 after 80 minutes annealing at 60°C. The module was biased at 400 V the region around strip 480 responses correctly to calibration signal, excluding an APV failure.

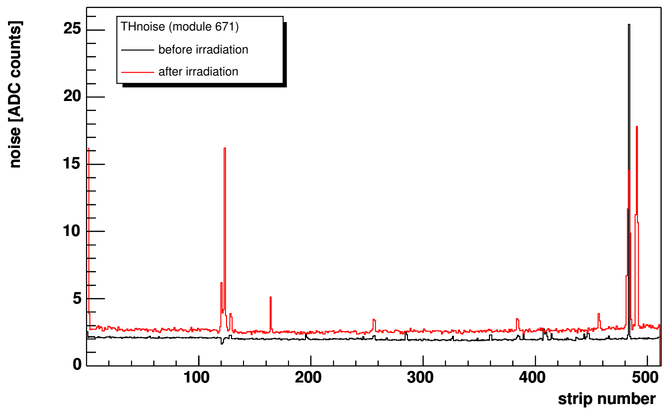

Figure 8.16: *Comparison of noise before and after irradiation (with protons) for module 671,* $V_{bias} = 500$ *V and* 80 *minutes annealing at* $60°C$. *On this module several strips occurred to be noisy after irradiation, strip* 121 *to* 123*, strip* 164*, strip* 481 *to* 485 *and strip* 489 *to* 492

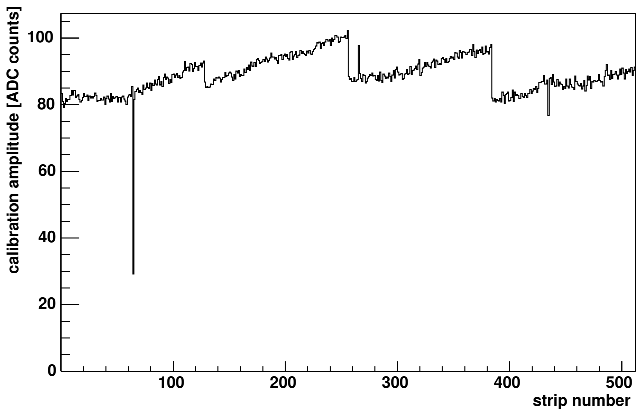

Figure 8.17: *Calibration amplitude for module 671 at* $V_{bias} = 400$ *V and* 80 *minutes annealing at* $60°C$. *The three channels with conspicuous calibration signals are caused by defective strips and not by defective channels in the front-end electronics*

8.4 Conclusion

Several problems in the silicon sensors reported by the QTC were investigated on module basis to see the impact on the performance and also the expected failure rate in the experiment.

The region with inter-strip resistance problem is well correlated to the region with increased noise, but as the inter-strip resistance reaches its nominal value around the depletion voltage and should therefore not affect the noise of an over-depleted module. This fact and the noise behavior after removing the passivation layer points to problems in the oxide layers.

Problems seen in the dependence of the leakage current on the applied mechanical stress on sensors seem to be less intense on modules. However, in case of the noise behavior a small dependence on the mechanical stress is seen. It is worth to mention that this effect is only seen on sensors from one manufacturer (ST Microelectronics) all sensors delivered by Hamamatsu never showed such a behavior.

After irradiation some strips showed up in noise on each of the three modules. This can be attributed to sensor problems since the APV chips react correctly to the calibration signal. In total 43 strips on the three modules increased in noise after irradiation this are $\approx 3\%$ of all strips. More concerning than the occurrence of 3% noisy strips is the fact that some of these strips are clustered, which hints to local inhomogeneities in the oxide layers or the p^+-implants.

Chapter 9

Summary

The CMS silicon strip tracker has to be operated in the harsh radiation environment of the LHC for ten years. Therefore it has to be ensured before the installation at the experiment that all components will withstand these conditions and can be fully operated during this time, since the accesses to the sub-detectors is limited.

The main part of this work was involved in the development of test-stations for the qualification of detector modules and the adoption of test procedures for the pre- and post-qualification of detector modules and front-end readout hybrids for irradiation studies as well as the investigation of problems seen on the sensors by the quality control center (QTC) on module basis.

During the study of the radiation hardness, one front-end readout hybrid and three silicon strip detector modules of tracker outer barrel (TOB) geometry were irradiated. The front-end was irradiated with protons to the highest fluence expected for the inner tracker part including a safety factor of ≈ 1.5, resulting in an equivalent fluence of 2.5×10^{14} n_{1MeV} cm^{-2}. Two modules were irradiated with protons to a fluence of 0.7×10^{14} n_{1MeV} cm^{-2} and one with neutrons to fluence of 1.21×10^{14} n_{1MeV} cm^{-2}. The most important parameters for the operation of a module are the depletion voltage, the leakage current and the signal to noise ratio (SNR). These parameters have been extensively studied on the three irradiated modules and for different annealing times to see their influence on the operation of the module. It has been shown that the depletion voltage is in good agreement with the "Hamburg model" and the current related damage rate calculated from the leakage current delivered comparable results with measurements done on sensor basis. The proton irradiated modules reached a SNR of ≈ 20 (15) in peak (deconvolution) mode, while for the neutron irradiated module a SNR of ≈ 17 (13) in peak (deconvolution) mode was reached. Considering that the neutron irradiated module was exposed to a much higher fluence than expected for outer barrel modules, these results show that the detector modules still have some safety margin in the operation voltage and SNR.

The ongoing quality control of the QTC on CMS silicon strip sensors discovered several problems, like regions of strips with low inter-strip resistances or strip leakage currents ranging from some 10 nA up to the order of μA partly reacting on mechanical stress. Out of these sensors modules were built to study the influence of these problems on the module performance. The module built of sensors with the inter-strip resistance problem showed an increased noise in the region where the saturation of inter-strips starts around the depletion voltage. The increased noise can not be caused by the inter-strip resistance since above 300 V all measured inter-strip resistances reached the value of the unaffected strips. The observed noise after removal of the passivation layer hints to problems of negative charges in the passivation layer or the underlying oxide layers.

The leakage current and the noise behavior of a detector module showed a dependence on mechanical and for the noise additionally on thermal stress. This is something to worry about since a certain and unavoidable mechanical stress is expected when the modules are mounted on rods or petals and cooled to the operating temperature. These results show that there are problems in the process of the sensor production, especially in the processing of the oxide layers and the passivation layer in case of ST Microelectronics. For Hamamatsu the other manufacturer for CMS silicon strip sensors such problems have never been observed.

Appendix A

Symbols and Constants

A.1 Physical Constants

Symbol	Description	Unit
c	speed of light	$299792458\ \mathrm{ms}^{-1}$
h	Planck constant	6.626098×10^{-34} Js
$\hbar = \frac{h}{2\pi}$	Planck constant, reduced	1.054571×10^{-34} Js
e	electron charge	$1.602176 \times 10^{-19}\ C$
ϵ_0	permittivity of free space	$8.854187 \times 10^{-12}\ \mathrm{Fm}^{-1}$
μ_0	permeability of free space	$4\pi \times 10^{-7}\ \mathrm{NA}^{-2} = 12.566270 \times 10^{-7}\ \mathrm{NA}^{-2}$
m_e	electron mass	$0.510998\ \mathrm{MeV/c}^2$
m_p	proton mass	$938.271998\ \mathrm{MeV/c}^2$
N_A	Avogadro's number	$6.022144 \cdot 10^{23}\ \mathrm{mol}^-1$
r_e	classical electron radius	$2.817940 \cdot 10^{-13}$ cm

Table A.1: *Physical constants* [hag02]

A.2 Properties of Silicon

Symbol	Description	Unit
$\epsilon_{silicon}$	relative permittivity of silicon	11.9
ϵ_{oxide}	relative permittivity of silicon oxide	3.9
ρ	density of silicon	$2.329\ \mathrm{g/cm}^3$
μ_n	mobility of electrons	$1500\ \mathrm{cm}^2/\mathrm{Vs}$
μ_p	mobility of holes	$450\ \mathrm{cm}^2/\mathrm{Vs}$
$E_{g_{silicon}}$	band gap in silicon (indirect semiconductor)	1.12 eV
$E_{g_{oxide}}$	band gap in silicon oxide	8.8 eV
λ	radiation length (Si / SiO_2)	9.36 cm / 10.2 cm
V_{break}	breakdown field	$\approx 3 \times 10^5$ V/cm

Table A.2: *Properties of Silicon*

A.3 Frequently Used Symbols

Symbol	Description	Unit
α	current related damage rate	A/cm
β	ratio of velocity v and velocity of light c	
γ_e	Euler's constant	0.577215665
A	atomic weight	
C_c	coupling capacitance	F
C_{int}	inter-strip capacitance	F
$D_{n,p}$	diffusion coefficient of electrons and holes	cm^2/s
E_c	lower edge of conduction band	eV
E_f	Fermi level	eV
E_g	band gap	eV
E_i	intrinsic energy level	eV
E_v	upper edge of valence band	eV
$m^*_{n,p}$	effective electron/hole mass	kg
n	free electron concentration	cm^{-3}
n_i	intrinsic carrier concentration	cm^{-3}
$n_{n,p}$	electron concentration in n- and p-regions	cm^{-3}
N_a	acceptor concentration	cm^{-3}
$N_{c,v}$	density of states in conduction/valence band	cm^{-3}
N_d	donor concentration	cm^{-3}
N_{eff}	effective doping concentration	cm^{-3}
p	free hole concentration	cm^{-3}
$p_{n,p}$	hole concentration in n- and p-regions	cm^{-3}
T	temperature	
Z	atomic number	

Table A.3: *Symbols frequently used throughout the text*

Appendix B

Acronyms and Abbreviations

Acronym	Description
AC	alternating current
ADC	analog to digital converter
APD	avalanche photodiode
APV	analog pipeline voltage chip
APSP	analog pulse shape processor
ASIC	application specific integrated circuit
CCU	communication control unit
CERN	European laboratory for particle physics
CMOS	complementary MOS
CMS	compact muon solenoid
APSP	analog pulse shape processor
CPLD	complex programmable logic device
DAC	digital to analog converter
DC	direct current
DCU	detector control unit
DPM	dual port memory
ENC	equivalent noise charge
FED	front end driver
FET	field effect transistor
FIFO	first in first out
FPGA	field programmable gate array
GUI	graphical user interface
HIP	highly ionizing particle
I^2C	I^2C bus protocol
IQC	irradiation qualification center
LED	light emitting diode
LEP	large electron positron collider

continued on next page

continued from previous page

Acronym	Description
LHC	large hadron collider
LSB	least significant bit
LVDS	low voltage differential signal
MIP	minimum ionizing particle
MIS	metal insulator semiconductor
MOS	metal oxide semiconductor
MSB	most significant bit
MSSM	minimal supersymmetric standard model
NIEL	non ionizing energy loss
PCB	printed circuit board
PCI	peripheral component interconnect
PLL	phase lock loop
PKA	primary knock-on atom
PMC	PCI Mezzanine card
QTC	quality control center
RMS	root mean square
SM	standard model
SNR	signal to noise ratio
SST	silicon strip tracker
TEC	tracker end-cap
TIB	tracker inner barrel
TID	tracker inner disk
TOB	tracker outer barrel
TTL	transistor-transistor logic
VPT	vacuum photo-triode

Table B.1: *Acronyms and Abbreviations*

Appendix C

Sensor Types and Modules

sensor type	width [mm]	length [mm]	thickness [mm]	pitch [μm]	number of strips	number of sensors
IB1	63.3	119.0	320	80	768	1536
IB2	63.3	119.0	320	120	512	1188
OB1	96.4	94.4	500	122	768	3360
OB2	96.4	94.4	500	183	512	7056
W1 (TEC)	64.6 - 87.9	87.2	320	81 - 112	768	288
W1 (TID)	63.6 - 93.8	112.9	320	80.5 - 119	768	288
W2	112.2 - 112.2	90.2	320	113 - 143	768	576
W3	64.9 - 83.0	112.7	320	123 - 158	512	640
W4	59.7 - 73.2	117.2	320	113 - 139	512	1008
W5a	98.9 - 112.3	84.0	500	126 - 142	768	1440
W5b	112.5 - 122.8	66.0	500	143 - 156	768	1440
W6a	86.1 - 97.4	99.0	500	163 - 185	512	1008
W6b	97.5 - 107.5	87.8	500	185 - 205	512	1008
W7a	74.0 - 82.9	109.8	500	140 - 156	512	1440
W7b	82.9 - 90.8	90.8	500	156 - 172	512	1440

Table C.1: *Sensor types, dimensions and multiplicity used for the silicon strip tracker. The IB and OB types are for the inner and outer barrel respectively, the W-sensor are the wedge shaped for the TEC and TID rings,* [dir03]

module type	range in radius [mm]	number of strips	number of sensors	number of modules
IB1	239.0 - 355.0	768	1	768
IB2	402.5 - 514.0	512	1	1188
OB1	610.0 - 868.0	768	2	1680
OB2	965.0 - 1080.0	512	2	3528

Table C.2: *Modules size, number of readout channels ,the number of sensor daisy-chained and their location inside the tracker for TIB and TOB,* [bre03]

module type	range in radius [mm]	number of strips	number of sensors	number of modules
Ring1	233.0 - 320.0	768	1	144
Ring2	323.0 - 411.1	768	1	288
Ring3	393.1 - 502.7	512	1	640
Ring4	504.1 - 619.2	512	1	1008
Ring5	603.2 - 750.4	768	2	720
Ring6	727.0 - 910.9	512	2	1008
Ring7	888.4 - 1094.1	512	2	1440

Table C.3: *Modules size, number of readout channels, the number of sensor daisy-chained and their location inside the tracker for TEC and TID,* [dir03]

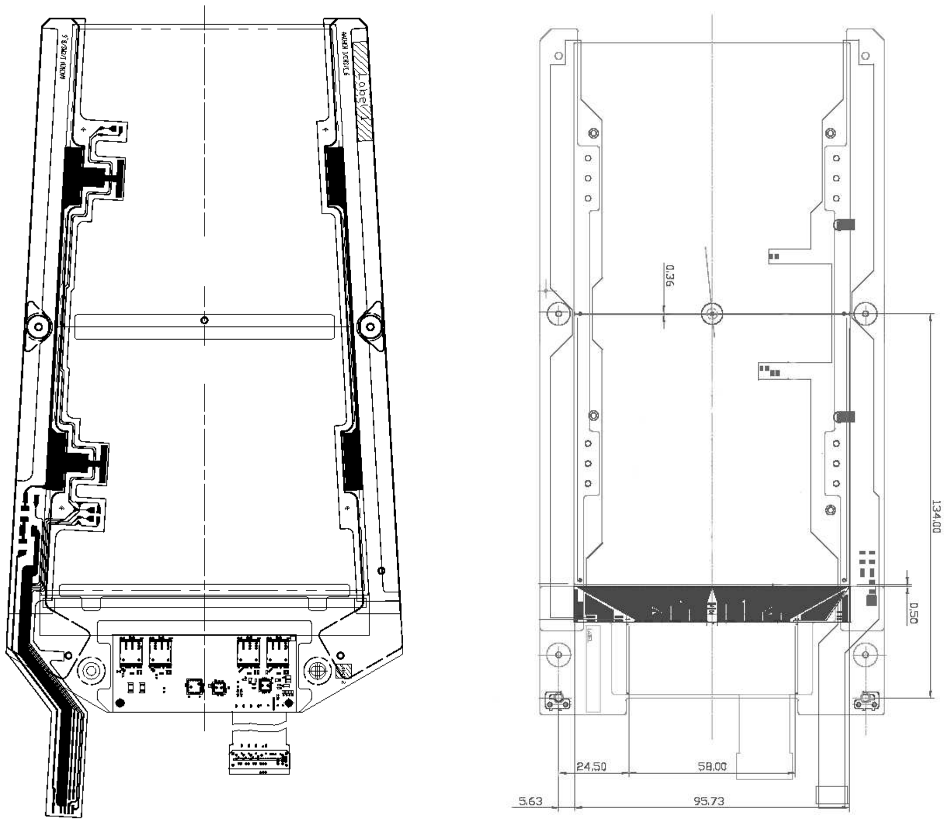

(a) (b)

Figure C.1: *Schematic drawing of ring 6 module (a) and OB2 (b)*

Appendix D

Calculation of LED to Fit Data Ratio

The LED system is a handy tool for failure tagging on modules. On the following pages the processing of LED data is shown. During a LED run the LED system is operated in pulse mode. This means that each LED is fired separately. The digitized data is filled into a histogram. On each LED cone a polynomial fit of order 8 is fitted. Figure D.1 shows the LED raw signal envelope histogram, which is filled with the maximum LED signal for each strip. This figure also shows that there is enough overlap between the LED cones to access every strip. Figure D.2 shows the LED fit envelope histogram, only the maximum value of the fit for each strip is stored. And finally in figure D.3 shows the LED ratio fit histogram. This is the ratio between the two histograms mentioned above. This data is taken to tag on missing signals. If a channel reacts correctly to the LED signal the ratio should be near one [fah04].

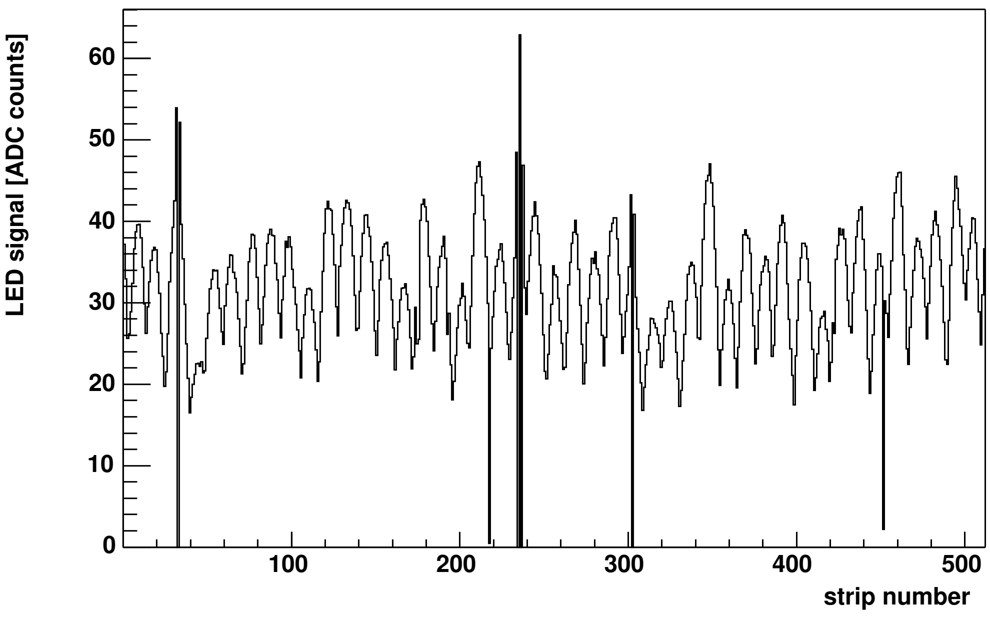

Figure D.1: *This graph shows the LED raw signal envelope. In here the maximum LED signal for each strip is plotted versus strip number*

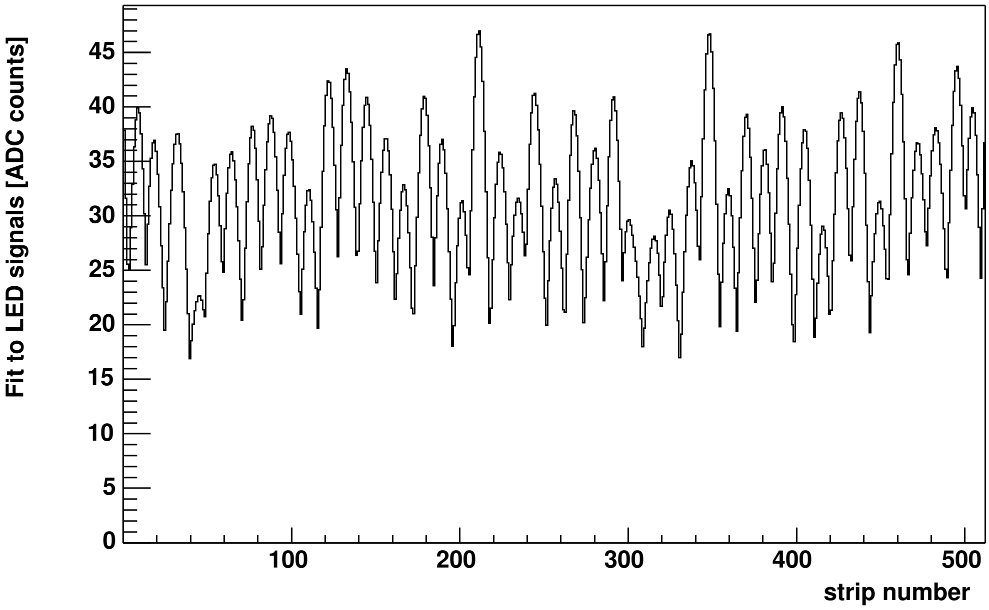

Figure D.2: *The LED fit envelope histogram shows a polynomial fit of order 8, done for each LED cone. The maximum value for those fits is plotted versus channel*

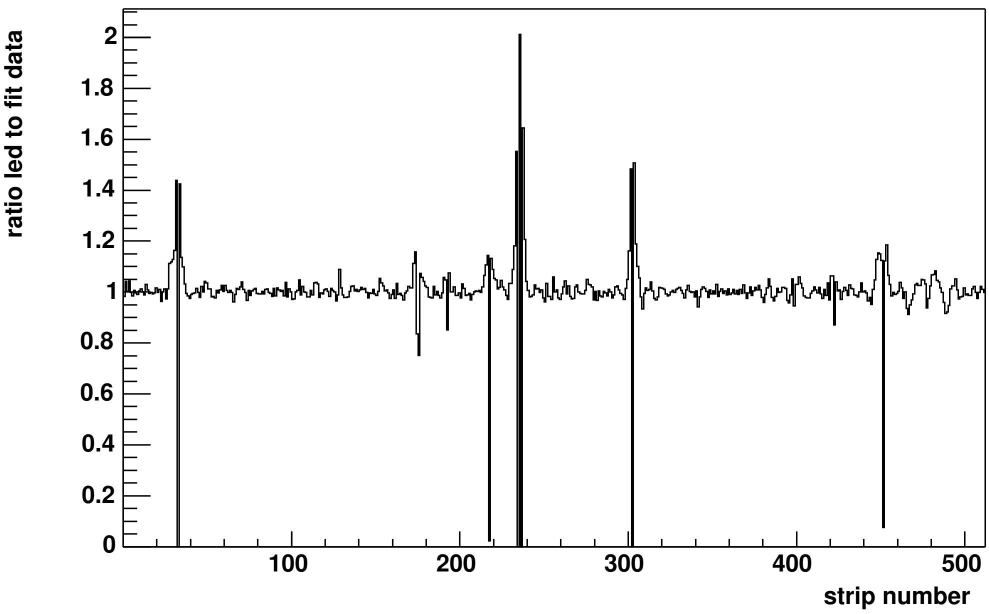

Figure D.3: *This graph shows the ratio between the LED raw signal envelope (figure D.1) and the LED fit envelope (figure D.2). If a strip reacts correctly to the LED signal the ratio should be around one*

Appendix E

Signal to Noise Calculation

In the following section the definition and equations used to calculate the SNR distribution (this is implemented in the readout software) and the corresponding most probable value is summarized.

E.1 Clustering and Signal to Noise Algorithm

First all data received during the particle run is pedestal and common mode corrected. The obtained data is scanned for clusters. The channels considered to belong to a particle hit must have a signal of at least three times the noise and the highest strip in the cluster a signal of at least five times the noise.

The cluster noise $N_{cluster}$ is the square root of the averaged squared noise of the strip contributing to the cluster

$$N_{cluster} = \sqrt{\frac{1}{n}\sum_{i}^{n} N_i^2} \tag{E.1}$$

The cluster signal $S_{cluster}$ is the sum of all signals from strips contributing to the cluster

$$S_{cluster} = \sum_{i}^{n} S_i \tag{E.2}$$

and finally the SNR is the cluster signal divided by the cluster noise

$$S_{SNR} = \frac{S_{cluster}}{N_{cluster}} \tag{E.3}$$

This value is filled into a histogram and stored in the local database for further processing [fah04].

E.2 Signal to Noise Fit

In the ideal case the energy loss in thin absorber is described by a Landau distribution (see section 4.1.5.3). Since the measurement is affected by noise and resolution effects, a Landau distribution convoluted by a Gaussian distribution is used to fit the data. The Gaussian distribution considers electronic noise and and detector fluctuations [dir03]. Figure E.1 and

E.1 show the fitted SNR distribution for peak and deconvolution mode respectively. The maximum value of the histogram was used as initial value for most probable.

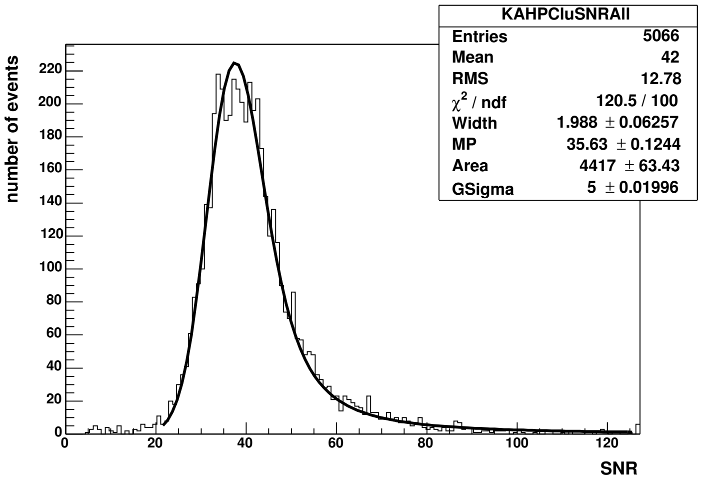

Figure E.1: *SNR in peak mode for module 671 at a bias voltage of* 350 *V, fitted by Landau distribution convoluted by Gaussian distribution*

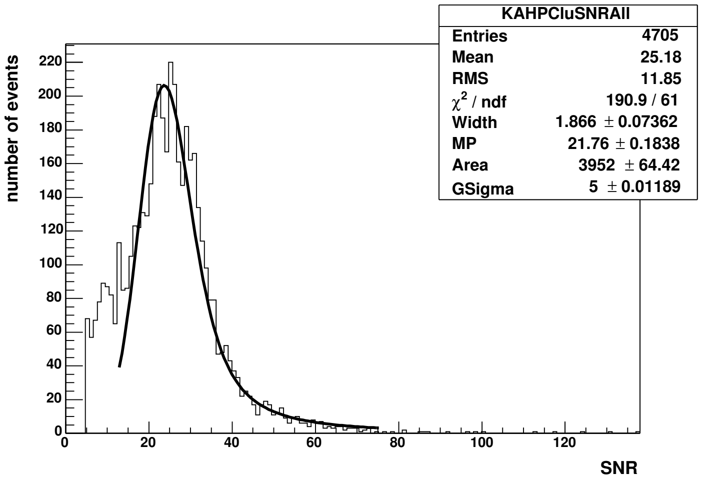

Figure E.2: *SNR in deconvolution mode for module 671 at bias voltage of* 350 *V, fitted by Landau distribution convoluted by Gaussian distribution*

Appendix F

Leaky strip Modules

The following sections presents the data of all measured strips during the mechanical stress test and the behavior of the global leakage current.

F.1 Module 1

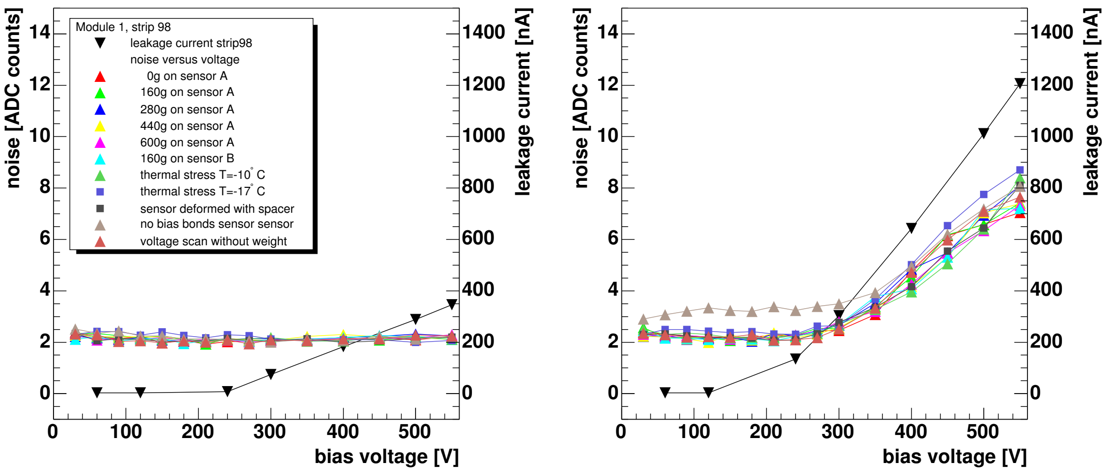

(a) strip 98 on sensor B

(b) strip 12 on sensor B

Figure F.1: *Strip noise for different mechanical and thermal stress versus voltage and corresponding strip leakage current for unstressed case on (a) strip* 98 *and (b) strip* 12*. The strip leakage current was measured for both strips on senor B*

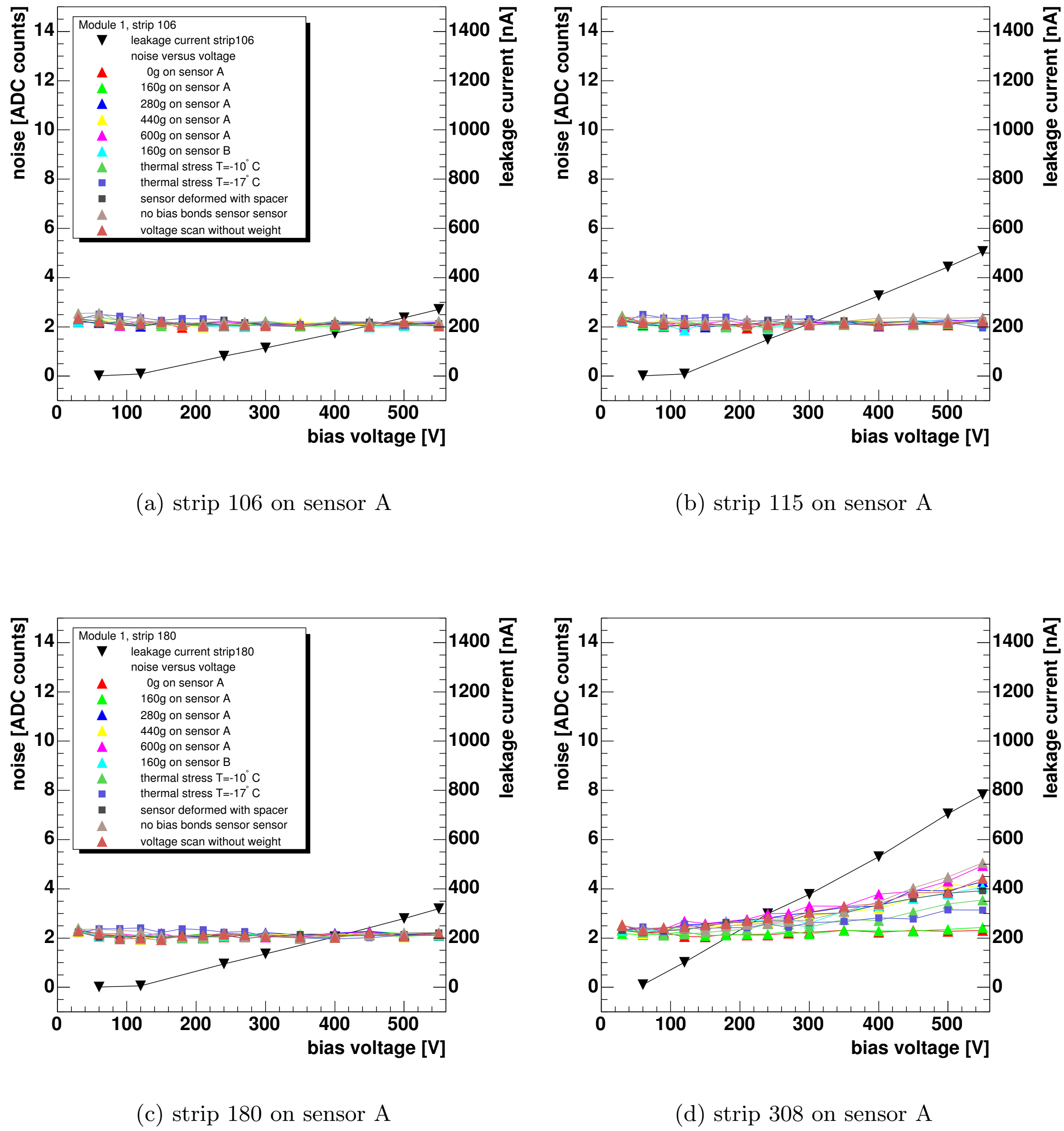

(a) strip 106 on sensor A

(b) strip 115 on sensor A

(c) strip 180 on sensor A

(d) strip 308 on sensor A

Figure F.2: *Strip noise for different mechanical and thermal stress versus voltage and corresponding strip leakage current for unstressed case, on (a) strip* 106*, (b) strip* 115*, (c) strip* 180 *and (d) strip* 308

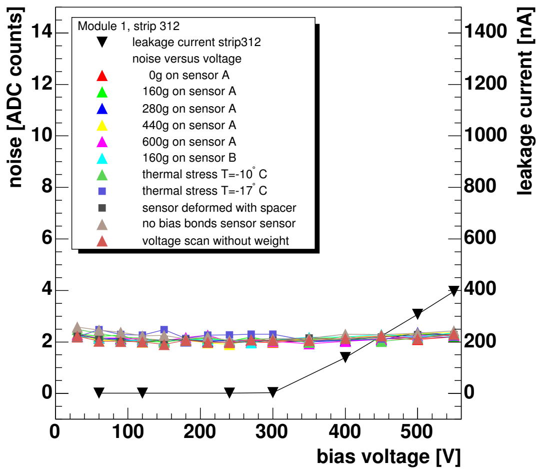

(a) strip 312 on sensor B

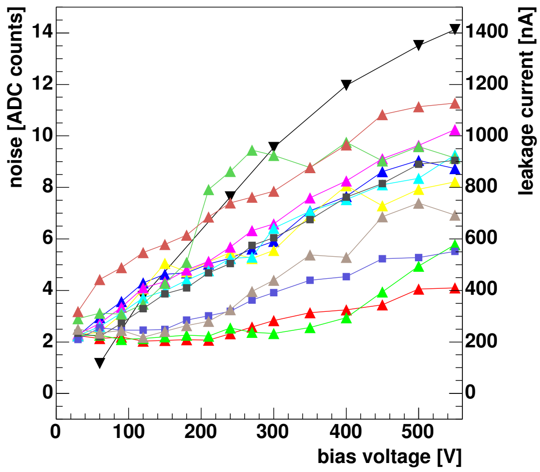

(b) strip 341 on sensor A

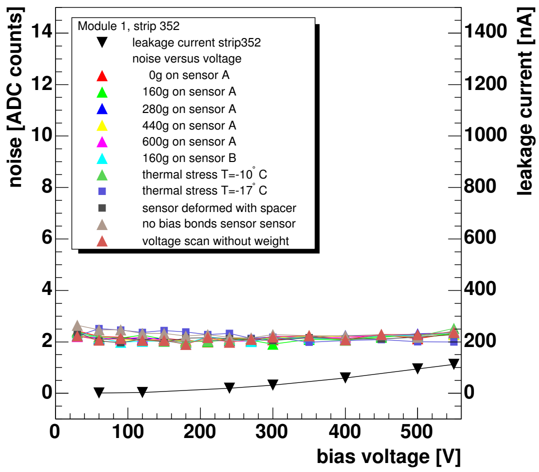

(c) strip 352 on sensor A

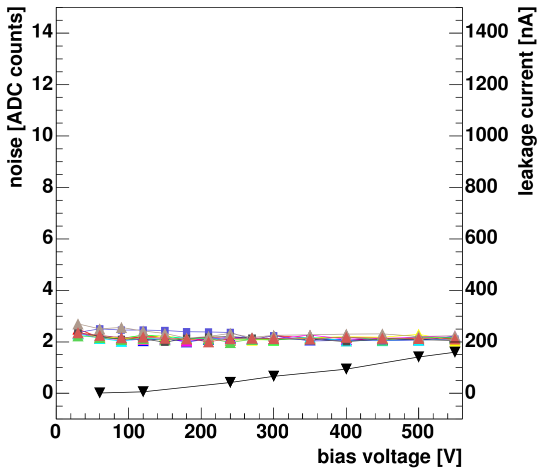

(d) strip 429 on sensor A

Figure F.3: *Strip noise for different mechanical and thermal stress versus voltage and corresponding strip leakage current for unstressed case, on (a) strip* 312*, (b) strip* 341*, (c) strip* 352 *and (d) strip* 429

F.2 Module 2

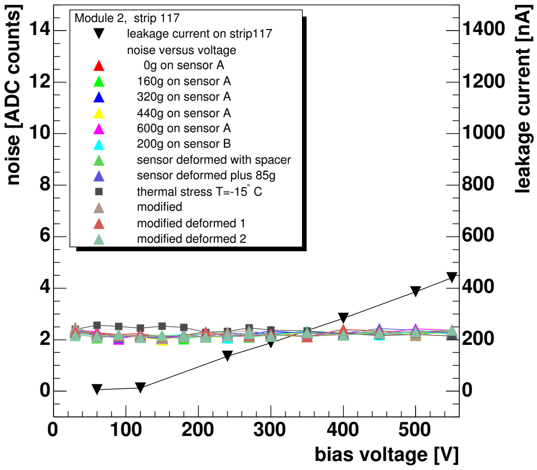

(a) strip 117 on sensor A

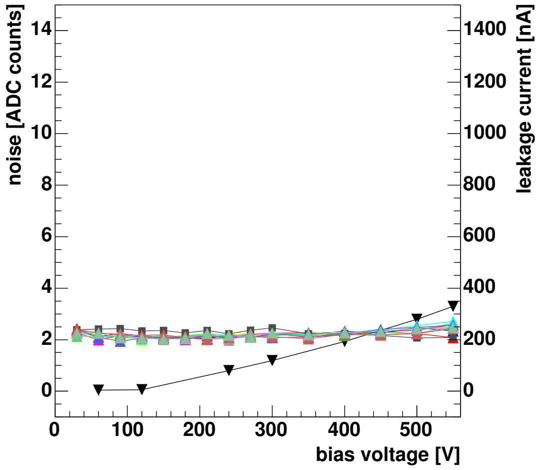

(b) strip 158 on sensor B

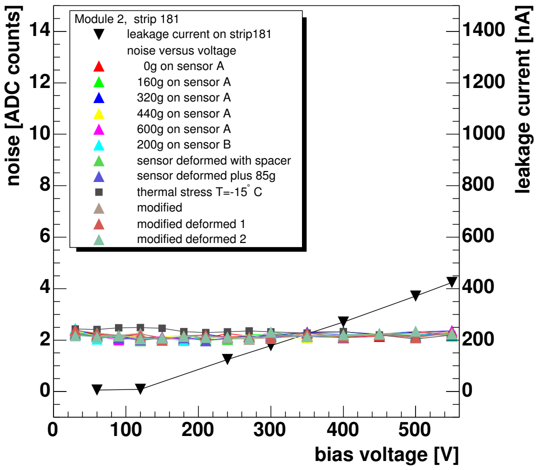

(c) strip 181 on sensor A

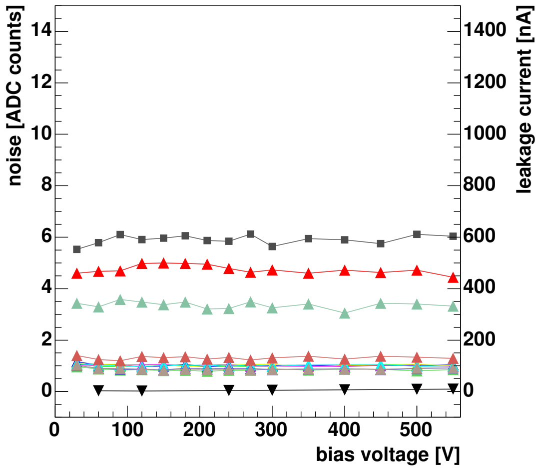

(d) strip 229 on sensor A

Figure F.4: *Strip noise for different mechanical and thermal stress versus voltage and corresponding strip leakage current for unstressed case, on (a) strip* 117*, (b) strip* 158*, (c) strip* 181 *and (d) strip* 229

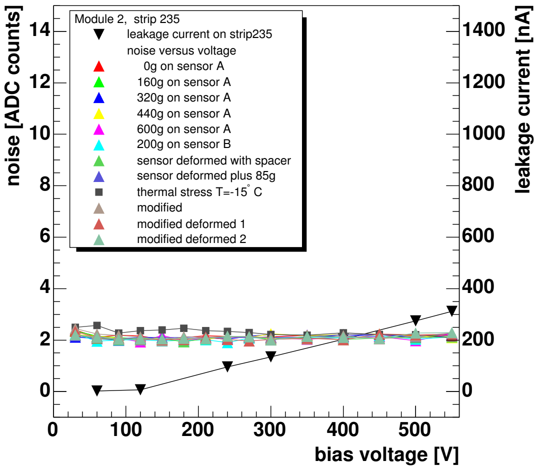

(a) strip 235 on sensor A

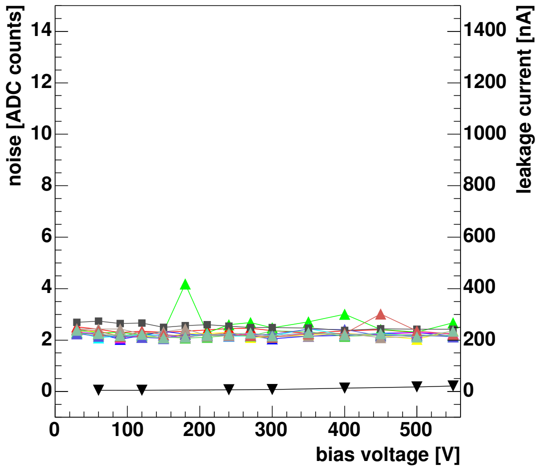

(b) strip 382 on sensor A

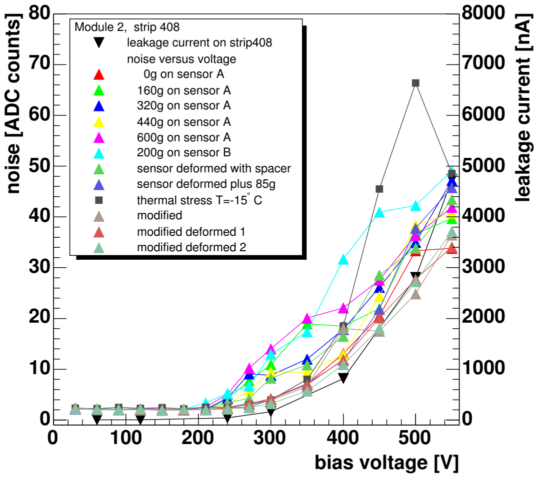

(c) strip 408 on sensor B

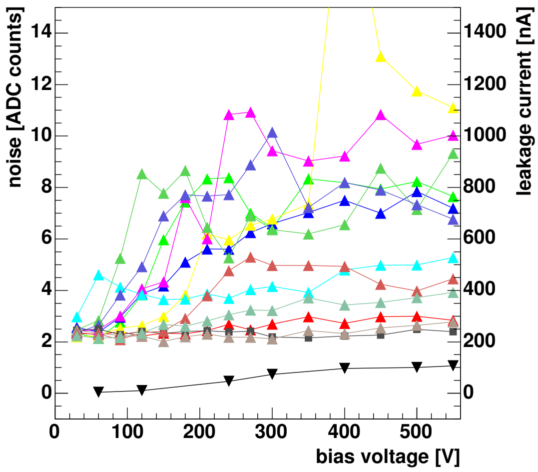

(d) strip 399 on sensor A

Figure F.5: *Strip noise for different mechanical and thermal stress versus voltage and corresponding strip leakage current for unstressed case, on (a) strip* 235*, (b) strip* 382*, (c) strip* 408 *and (d) strip* 399

F.3 Global Leakage current module 1 and module 2

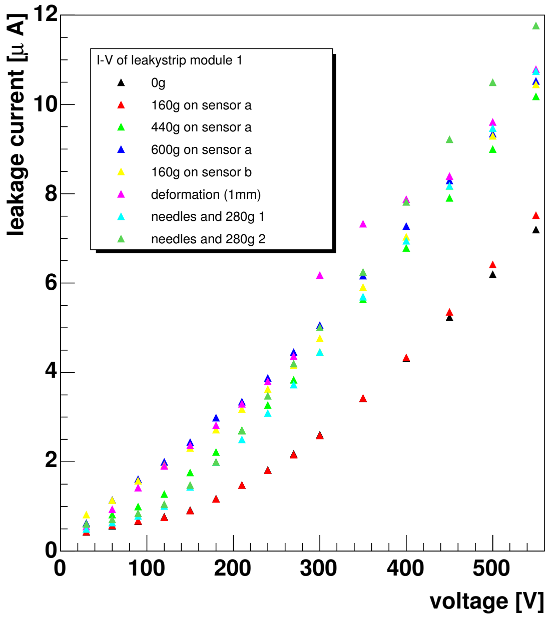

Figure F.6: *Global leakage current for module 1*

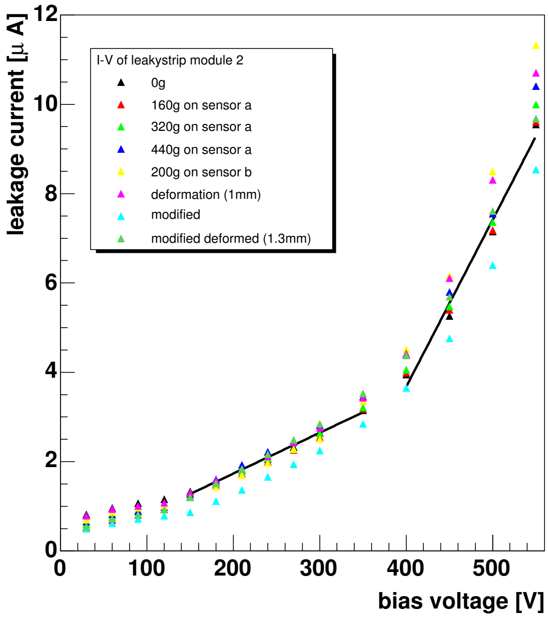

Figure F.7: *Global leakage current for module 2*

List of Figures

List of Tables

Index

Bibliography

[agr03] J.-L. Agram et al., The silicon sensor for the Compact Muon Solenoid Tracker - Design and qualification procedure, CMS Note 2003/15, 2003.

[alt03] Altera MAX 7000 programmable logic device family, data sheet, version 6.6, 2003.

[as+03] S. Assouak, et al., Irradiations of CMS silicon sensors with fast neutrons, Nucl. Instrum. Meth., A 514, 156-162, 2003.

[axe01] M. Axer et al., A test setup for quality assurance of front end hybrids, CMS Note 2001/046, 2001.

[bai99] S. A. Baird, et al., A PMC based ADC card for CMS Tracker readout, IEEE Real-Time Conference, Santa Fe, USA, 1999.

[bat02] M. Battaglia, et al., The CKM matrix and the unitarity triangle, workshop on the CKM unitarity triangle, CERN, hep-ph/0304132, 2002.

[ber01] K. Bernier, An intense fast neutron beam in Louvain-la-Neuve, http://www.fynu.ucl.ac.be/themes/he/cms/neutron_beam/neutrons-beam.html, 2001.

[bei01] F. Beißel, ARC_FE, III. Physikalisches Institut, RWTH Aachen, 2001.

[ber92] L. Bergmann, Lehrbuch der Experimentalphysik, Band 6, Festkörper, Walter de Gruyter, 1992.

[bin93] N. Bingefors, et al., A novel technique for fast pulse shaping using a slow amplifier at LHC, Nucl. Instrum. Meth., A 377, 290-297, 1996.

[boc98] R. K. Bock and A. Vasilescu, The particle detector briefbook, Springer 1998.

[bor03] L. Borello, Sensor design for the CMS silicon tracker, CMS Note 2003/20, 2003.

[bre03] H. Breuker, CMS tracker parameter booklet, 2003.

[che76] J. R. Chelikowski and M. L. Cohen, Nonlocal pseudopotential calculation for the electronic structure of eleven diamond and zinc-blende semiconductors, Phys. Rev. B14, 556, 1976.

[cla02] C. Claeys and E. Simoen, Radiation Effects in advanced semiconductor materials and devices, Springer 2002.

[CMS94] The CMS Collaboration, The compact muon Solenoid, Technical Proposal, CERN-LHCC-94-38, 1994.

[CMS97a] The CMS Collaboration, The electromagnetic calorimeter project, Technical design report, CERN-LHCC-97-33, 1997.

[CMS97b] The CMS Collaboration, The hadronic calorimeter project, Technical design report, CERN-LHCC-97-31, 1997.

[CMS97c] The CMS Collaboration, The magnet project, Technical design report, CERN-LHCC-97-10, 1997.

[CMS97d] The CMS Collaboration, The muon project, Technical design report, CERN-LHCC-97-32, 1997.

[CMS98] The CMS Collaboration, The tracker project, Technical design report, CERN-LHCC-98-6, 1998.

[CMS00] The CMS Collaboration, Addendum to the tracker TDR, CERN-LHCC-2000-016, 2000.

[CMSWEB] CMS, plots and drawings, http://cmsinfo.cern.ch/Welcome.html/CMSdocuments/CMSdocuments.html .

[das55] W.C. Dash and R. Newman, Phys. Rev. 99 (1955) 1154, 1955.

[die03a] A. Dierlamm, Studies on the radiation hardness of silicon sensors, PhD thesis, Universität Karlsruhe (TH), IEKP-KA/2003-23, 2003.

[die03b] A. Dierlamm, Irradiation qualification of CMS silicon tracker components with protons, Nucl. Instrum. Meth., A 514, 162-172, 2003.

[dir02] G. Dirkes, F. Hartman, L. DeMaria and M. Meschini, Procedures for module testing, CERN, 2002.

[dir03] G. Dirkes, Development and implementation of quality control strategies for CMS silicon strip tracker modules, PhD thesis, Universität Karlsruhe (TH), IEKP-KA/2003-23, 2003.

[djo97] A. Djouadi, J. Kalinowski and M. Spira, HDECAY: a program for Higgs boson decays in the standard model and its supersymmetric extension, hep-ph/9704448, 1997.

[dro01] V. Drollinger, Reconstruction and analysis methods for searches of Higgs bosons in the decay mode $H^0 \rightarrow b\bar{b}$ at hadron colliders, PhD thesis, Universität Karlsruhe (TH), IEKP-KA/2001-26, 2001.

[kap97] Du Pont, Kapton general information, data sheet, Du Pont, 1997.

[ege03] U. Egede, CKM reach at hadron colliders, workshop on the CKM unitary triangle, IPPP Durham, conference proceedings, 2003.

[fah04] M. Fahrer, Karlsruhe readout for CMS tracker modules, user's manual, version 1.0, Institut für Experimentelle Kernphysik, Universität Karlsruhe (TH), 2004.

[fel01] L. Feld, Halbleiter-Spurdetektoren für den LHC, Physikalisches Kolloquium, Universität Freiburg, http://sct.physik.uni-freiburg.de/atlas/sct/talks/habil_final.ppt, 2002.

[fre01] M. J. French, et al., Design and results from APV25, a deep sub-micron CMOS front-end chip for the CMS tracker, Nucl. Instrum. Meth., A 466, 359-365, 2001.

[fri01] M. Friedl, The CMS silicon strip tracker and its electronic readout, PhD thesis, Vienna University of Technology, 2001.

[fur02] A. Furgeri, Studien zu Strahlenschäden an Siliziumstreifensensoren für CMS, Diplomarbeit, Universität Karlsruhe (TH), IEKP-KA/2002-14 ,2002.

[fur04] A. Furgeri, Radiation damage effects on CMS sensors quality assurance and irradiation tests, IEEE Nuclear Science Symposium and Medical Imaging Conference, Portland, USA, 2003.

[gad92] S. Gadomski, et al., The deconvolution method of fast pulse shaping at hadron colliders, Nucl. Instrum. Meth., A 320, 217-227, 1992.

[gia02] P. Giacomelli, The CMS muon detector, Nucl. Instrum. Meth., A 478, 147-152, 2002.

[hag02] K. Hagiwara et al., Physical Review D66, 010001-1, 2002.

[hei01] S. Heier, Entwicklung einer Teststation für CMS-Mikrostreifendetektoren, Diplomarbeit, Universität Karlsruhe (TH), IEKP-KA/2001-18, 2001.

[her01] A. Herve, et al., Status of the CMS magnet, DAPNIA-STCM-01-10, 2001.

[hor89] P. Horowitz and W. Hill, The art of electronics, Cambridge University Press, 1989.

[hov04] Pierre van Hove, private communication, 2004.

[ise02] Iseg, High voltage module (BPz 10 305 12), iseg, http://www.iseg-hv.de, 2002.

[jon99] L. L. Jones, et al., The APV25 deep submicron readout chip for CMS detectors, prepared for 5th workshop on electronics for LHC experiments, Snowmass, Colorado, 1999.

[jon01] L. L. Jones, APV25-S1 user's guide version 2.2, Rutherford Appleton Laboratory, 2001.

[kno99] G. F. Knoll, Radiation detection and measurement, John Wiley & Sons 1999.

[kot01] D. Kotlinski, The CMS pixel detector, Nucl. Instrum. Meth., A 465, 46-50, 2001.

[kra03] N. V. Krasnikov and V. A. Matveev, Search for new physics at LHC, hep-ph/0309200, 2003.

[len01] M. Lenzi, Performance of the all-silicon CMS tracker, Nucl. Instrum. Meth.,A 473, 31-38, 2001.

[leo87] W. R. Leo, Techniques for nuclear and particle physics experiments, Springer 1987.

[lut99] G. Lutz, Semiconductor radiation device physics, Springer 1999.

[ma 89] T. P. Ma and P. V. Dressendorfer, Ionizing radiation effects in mos devices and circuits, John Wiley & Sons 1989.

[mag01] M. Magazzu, et al., DCU2 user's guide, version 2.16, CERN - EP/MIC, 2001.

[mer98] J. P. Merlo, CMS hadronic forward calorimeter, Nuclear Physics B (Proc. Suppl), B 61, 41-46, 1998.

[mig02] E. Migliore, Measurements on pitch adapter in Torino, CMS tracker electronics meeting, http://cmsdoc.cern.ch/~ghall/TKEL_0102/Migliore_0102.pdf, January 2002.

[mol99] M. Moll, Radiation damage in silicon particle sensors: microscopic defects and macroscopic properties, PhD thesis, Desy, DESY-THESIS-1999-040, 1999.

[mol02] M. Moll, et al., Relation between microscopic defects and macroscopic changes in silicon detector properties after hadron irradiation, Nucl. Instrum. Meth., B 186, 100-110, 2002.

[mur00] P. Murray, APVMUX user's guide, version 1.0, CERN, 2000.

[nev99] A. Neviani, APV25S0 Calibration circuit Version 1.1, 1999.

[ni 02] National Instruments, DAQ NI 6034E/6035E/6036E user's manual, National Instruments, 2002.

[phi00] Philips Semiconductors, The I^2C-bus specification, version 2.1, 2000.

[pla00] P. Placidi, et al., CMS tracker PLL reference manual, version 2.0, CERN - EP/MIC, 2000.

[ray00] M. Raymond, et al., The CMS Tracker APV25 0.25 μm CMOS readout chip, prepared for 6th workshop on electronics for LHC experiments, Krakow, Poland, 2000.

[ray01] M. Raymond, Results from lab tests of module, CMS tracker electronics meeting, http://cmsdoc.cern.ch//~ghall/TKEL/TKEL_1001/Raymond_1001.pdf, October 2001.

[roy03] D. P. Roy, Higgs and SUSY searches at the LHC: An overview, hep-ph/0303106, 2003.

[sch02] W. Schwerdtfeger, Entwicklung von Systemkomponenten zur Qualitätssicherung von CMS-Silizium-Streifen-Detektoren, Diplomarbeit, Universität Karlsruhe (TH), IEKP-KA/2002-09, 2002.

[sgu04] G. Sguazzoni, The CMS Si-strip tracker, Proceedings of the 7th International Conference on ICATPP-7, to be published on World Scientific, 2004.

[spi00] H. Spiesberger, M. Spira and P. M. Zerwas, The standard model Higgs: Physical basics and scattering experiments, hep-ph/0011255, 2000.

[sze81] S. M. Sze, Physics of semiconductor devices, John Willey & Sons, 1981.

[wal02] M. Waldschmitt, Fertigstellung einer Teststation zur Qualifikation CMS Siliziumstreifendetektormodulen, Diplomarbeit, Universität Karlsruhe (TH), IEKP-KA/2003-02, 2003.

[wei02] Th. Weiler, LED array , version 1.2, data sheet, Institut für Experimentelle Kernphysik, Universität Karlsruhe (TH), 2002.

[wei03] Th. Weiler, et al., Infrared LED array for silicon strip sensor qualification, CMS Note 2003/023, 2003.

[wro02] G. Wrochna, Heavy ion physics with the CMS detector, Eur. Phys. J. direct C, 4(S1), 23, 2002.

[wun96] R.Wunstorf et al., Damage-induced surface effects in silicon detectors, Nucl. Instrum. Meth., A 377, 290-297, 1996.

Acknowledgements

Here I want to thank the people from the Institut für Experimentelle Kernphysik and the CMS collaboration contributing to the realization of this work.

First of all I want to thank Prof. Dr. Thomas Müller giving me the possibility and freedom to perform this work. Prof. Dr. Wim de Boer I want to thank for being my co-reference.

A special thank to Dr. Siegfried Weseler ($2001^\dagger$) who inspired most of the electronical part of this work. I learned a lot from him about electronics and layout design and profited from his tremendous knowledge about on physics.

Dr. Peter Blüm our group leader for the coordination of our activities and his fruitful discussion concerning this work. Further I have to thank him for reading and commenting this manuscript.

I have to thank Dr. Hans-Jürgen Simonis for the help on technical aspects, for solving computer and network problems.

Dr. Frank Hartmann for his contribution to this work by organizing work and finding interesting topics to investigate on silicon strip detectors. For his hints and discussion concerning silicon sensors.

Without the help from the people at Karlsruhe readout group this work would not be possible. Hence a lot thanks for the good collaboration and collegial atmosphere to Dr. Guido Dirkes, Manuel Fahrer, Dr. Javier Fernandez, Stefan Heier, Tino Ortega-Gomez, Wolfgang Schwerdtfeger and Markus Waldschmitt.

Dr. Alexander Dierlamm and Alexander Furgeri for organizing the irradiations and the fruitful discussion about silicon sensors and their behavior after irradiation.

Our technicians Pia Steck and Tobias Barvich for the help on the various problems which came up during this work. Especially for design of crates for the electronics of the test-stations, the construction and bonding of modules.

Samia Assouak and Eric Forton for the irradiation of a detector module with neutrons at the cyclotron at Louvain-la-neuve.

Edeltraut Haas and Diana Fellner-Thedens for helping through administrative and bureaucratic problems.

Last but not least I want to thank my parents for their support.